UNIVERSITY OF OKLAHOMA

GRADUATE COLLEGE

3D QUANTITATIVE SEISMIC STRATIGRAPHY OF JURASSIC CARBONATE STRATA ON THE ARABIAN PLATFORM

A THESIS

SUBMITTED TO THE GRADUATE FACULTY

in partial fulfillment of the requirements for the

Degree of

MASTER OF SCIENCE

By

ALI ALSHAFEI
Norman, Oklahoma
2018

3D QUANTITATIVE SEISMIC STRATIGRAPHY OF JURASSIC CARBONATE STRATA ON THE ARABIAN PLATFORM

A THESIS APPROVED FOR THE
CONOCOPHILLIPS SCHOOL OF GEOLOGY AND GEOPHYSICS

BY

Dr. John D. Pigott, Chair

Dr. Kurt J. Marfurt

Dr. Gerilyn S. Soreghan

Acknowledgements

I would like to express my gratitude to my advisor, Dr. John D. Pigott for his guidance, support, and good nature throughout my master's study. I would also like to thank Drs. Kurt J. Marfut and Gerilyn S. Soreghan for their discussions, valuable suggestions, comments, and professional inputs on my thesis.

I would like to thank Saudi Aramco for providing me data and supporting me financially to pursue my master's degree.

Further, I would like to thank the contributors of the Attribute-Assisted Seismic Processing and Interpretation (AASPI) Consortium (AASPI software), Schlumberger (Petrel and Techlog) and CGG (Geoview), for providing licenses for the software that were used in this work.

Many thanks go to my family especially my grandparents, parents, brothers and sisters for their continues support. Most importantly, special thanks to my wife Fatimah for her encouragements and patience throughout my life. Without her support, it is impossible to finish my graduate education. I wish to thank my two wonderful children, Ameer and Hadi, who provide unending inspiration.

Table of Contents

List of Figures

Abstract

Quantitative seismic stratigraphy of a 3D seismic volume of the Arabian platform provides critical information on the heterogeneity of reservoir quality of a productive Jurassic carbonate grainstone. The Vail method of sequence stratigraphy allowed the delineation of thirteen sequence boundaries from the Permian to the Cenozoic. Integrating the Galloway petrophysical methods of sequence stratigraphy from well constraints, four third-order cycles of HST, RST, TST, and LST parasequence sets are identified. As these are regionally correlated on the seismic they appear to be allocyclically controlled. The 3D porosity prediction via neural network application successfully predicted the continuity of HST high porosities, suggesting the porosities were caused by fresh-water vadose/phreatic diagenesis of these Hothouse mineralogies during sea level falls of the ensuing RST's. Unfortunately, while discernible in the wells, these parasequence sets are below seismic resolution for interpretation. The LST's have good mudstone deposition with accompanying enriched organic matter content for potential self-sourcing of the overlying HST's. The TST's which followed, much like the RST's, are below seismic resolution for mapping. Combined with post-depositional structural, this parasequence porosity centralization in these stacked cycles of carbonates provides an ideal assemblage of reservoir criticals for hydrocarbon accumulation and suggests quantitative seismic stratigraphy is a powerful tool for Arabian platform Jurassic carbonate exploration and exploitation.

Chapter 1 Introduction

1.1 Problem Definition:

Porosity distribution within carbonate reservoirs is often problematic, a complex interplay between the initial energy of the depositional facies, the diagenetic susceptibility of allochems, and cement mineralogy and of changes in water chemistry through time.

This investigation employs quantitative seismic stratigraphy in order to gain insight into the carbonate depositional facies, their relation in both time and space, and their reservoir properties within a Jurassic-aged interval from a study area within the boundaries of the Kingdom of Saudi Arabia (Figure 1). A three-dimensional (3D) seismic dataset will be analyzed, constrained with borehole data, and interpreted within a high resolution sequence stratigraphic framework in order to examine the possible association with changes in relative sea level.

Figure 1: Location of the Arabian Plate, highlighted in the red box.

1.2 Study Location:

As this study will utilize proprietary data, the precise location and formation names are confidential. However, the study area is on the Arabian Platform within the Kingdom of Saudi Arabia (Figure 2). The formations of interest for this study date to the Jurassic, and remain of especial exploration interest to the petroleum industry as the Kingdom of Saudi Arabia has historically enjoyed prolific production from similar-aged formations.

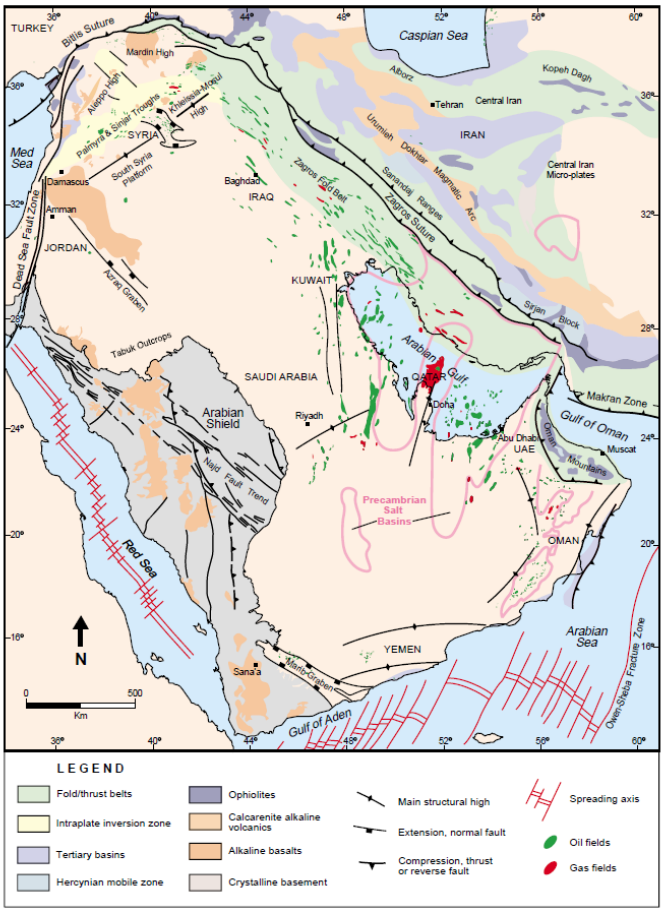

Figure 2: Major tectonic elements of the Arabian Plate. The pink boundaries show the Precambrian salt basins. From Konert et al. (2001).

Indeed, Dammam Well No. 7 targeted Jurassic formations, and the world's largest oil field, "Ghawar," has an ultimate recovery equivalent (oil and gas) of 97,099 Million Barrels of Oil Equivalent (MMBOE), produces primarily from Jurassic intervals (Mann et al., 2000).

1.3 Data Available:

This study is based on the following data, as shown in Figure 3:

1. A post-stack time-migrated 3D seismic volume spanning approximately 4,500 km^2, comprising 2,800 inline and 2,300 crossline seismic, with a sampling interval of 4 milliseconds (ms).
2. Five wells located within the 3D seismic survey boundaries. The well data include caliper, gamma ray (GR), neutron density (ND), density (ρ) and sonic logs. Though included, and with excellent coverage of the Jurassic intervals of interest, lithology cuttings logs were not utilized in this study as they are based upon interpretations made at the time of drilling. In combination with the tendency of cuttings to mix, and the inconsistency of cutting classifications, there is little confidence in their validity.
3. Approximately 520 feet (ft) (≈158 meters) of core data, which include core description, photos, digital thin sections, and partial (discrete) core measurement data (porosity and permeability).

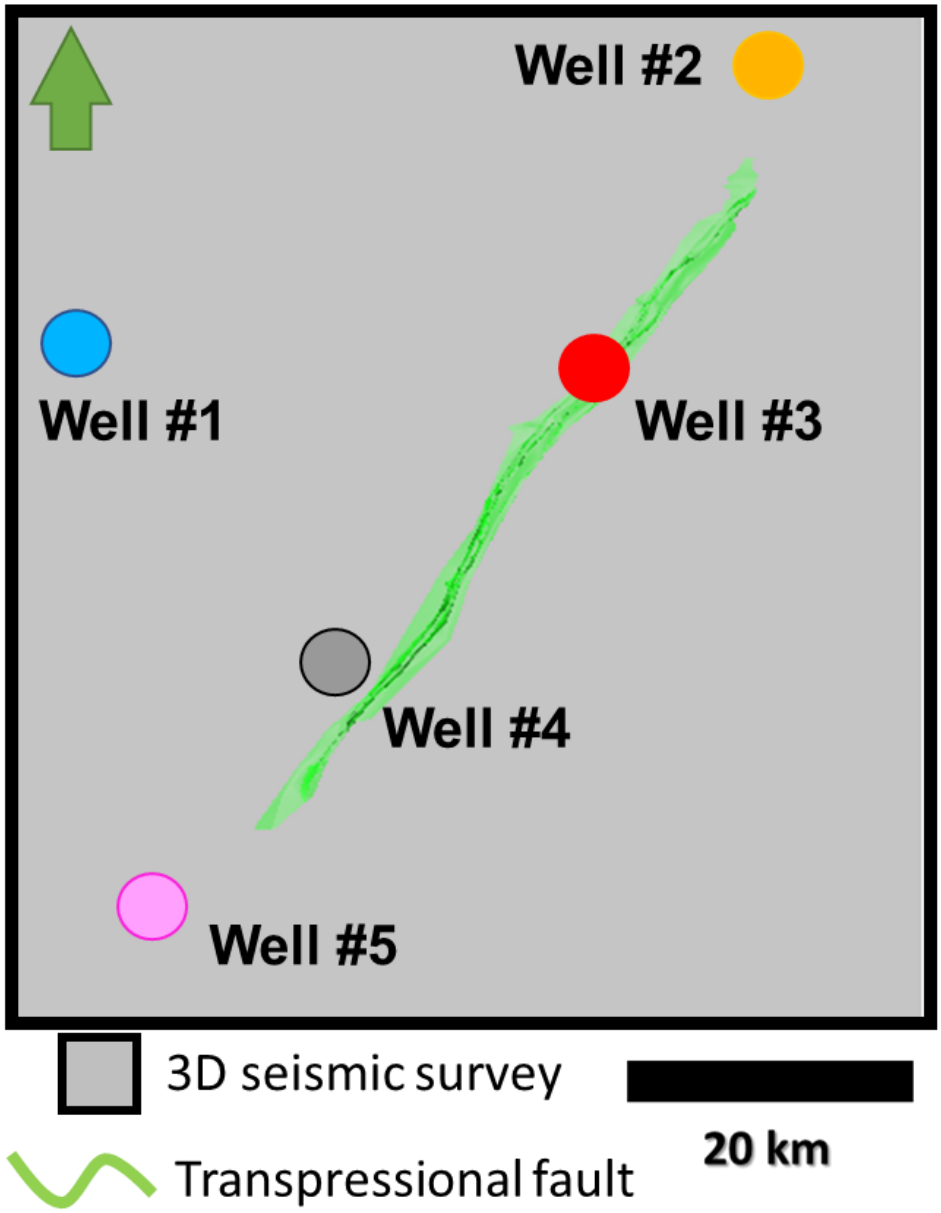

Figure 3: Data used during the study. The gray area represents the extent of the 3D seismic survey. The colored circles represent the well locations. The green line represents the transpressional fault.

1.4 Data Condition:

1.4.1 Seismic Data:

One of the first tasks when dealing with seismic data is to examine the volume for artifacts that may mislead or obstruct future attempts at interpretation. The acquisition footprint and near surface are several examples of artifacts common to seismic data (Chopra and Marfurt, 2007). Figure 4 shows a shallow time slice @ -32 ms through the seismic volume with prominent acquisition footprint artifacts demonstrating North-South and East-West trends. Backscattered noise and non-uniform bin size owing to variation in fold, offset, and azimuth are all known contributors to acquisition footprint (Chopra and Marfurt, 2007). Near-surface terrain artifacts, on the other hand, affect the resolution of the shallow time in the seismic section up to 500 ms, as shown in Figure 5. Fortunately, neither horizontal trace normalization or vertical trace balancing were performed as is the common case for purely structural balancing interpretations of seismic. Overall the seismic data quality with respect to acquisition and processing is viewed as favorable for this quantitative seismic stratigraphic approach.

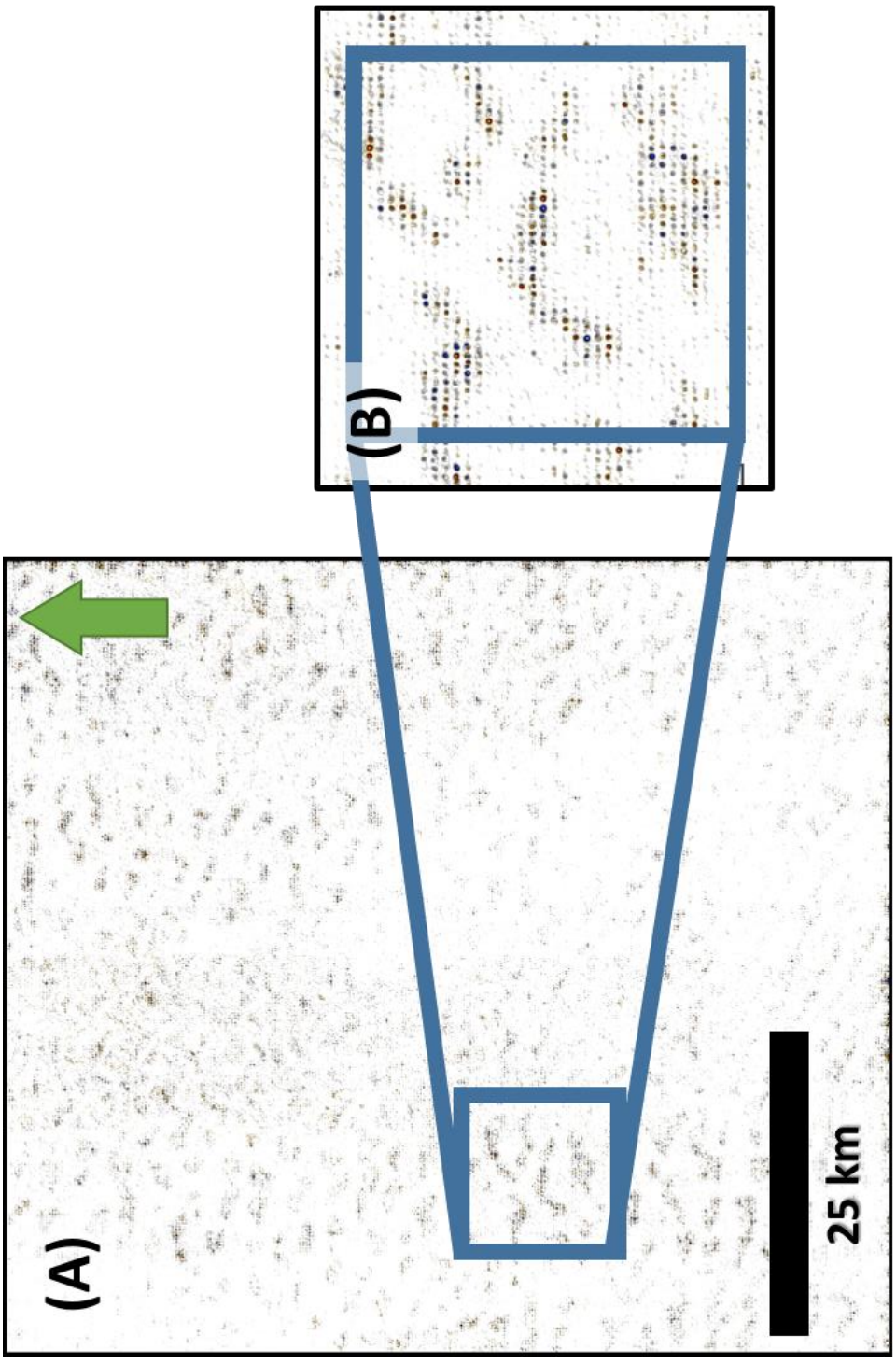

Figure 4: (A) Shallow time slice @ 32 ms through a seismic amplitude volume extracted from the 3D seismic survey @ -32ms. **(B)** A zoomed in section from the time slice to show North-South and East-West acquisition footprint trends.

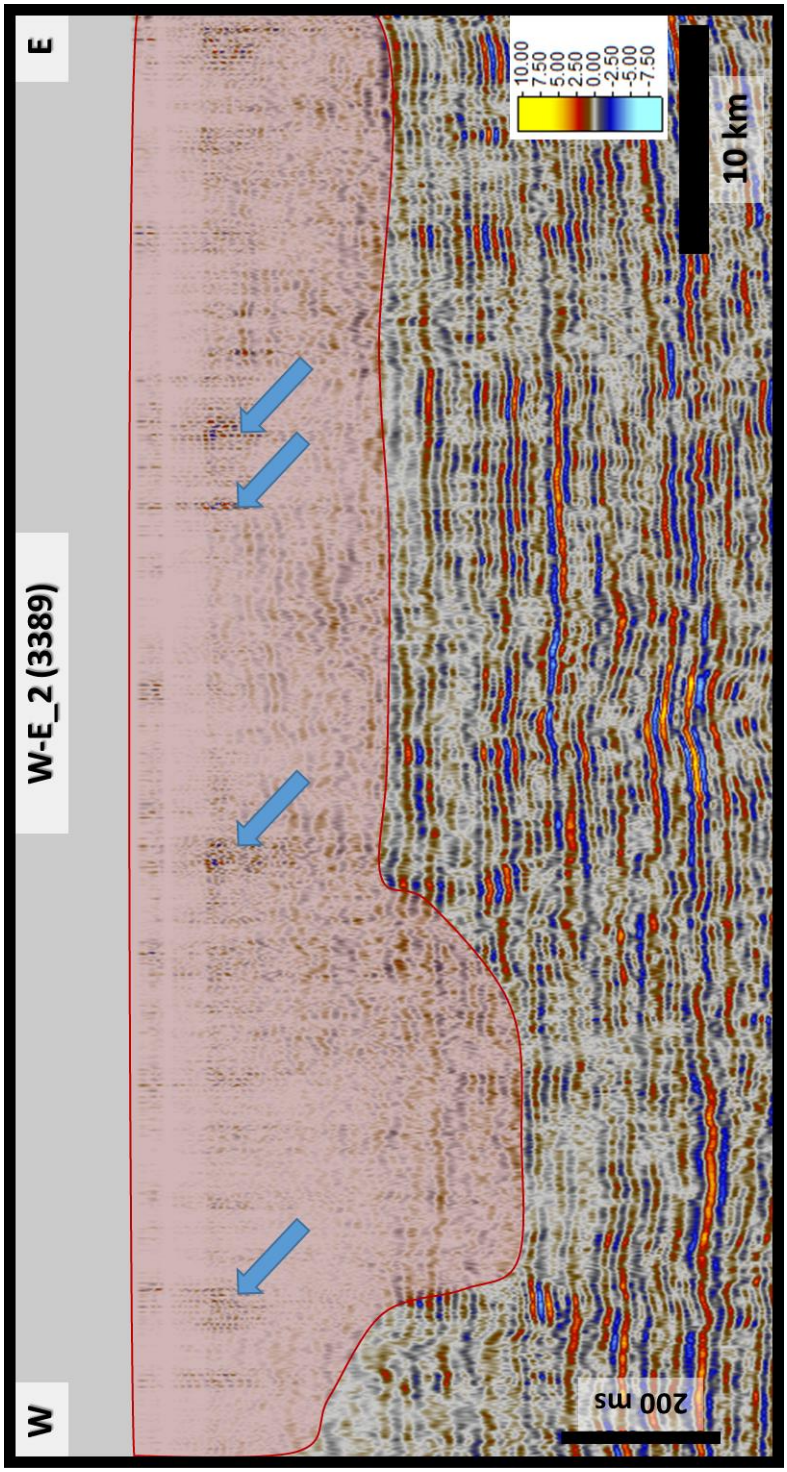

Figure 5: E-W seismic section reveling the effects of the near-surface topography on the shallow section (highlighted by the red polygon). Blue arrows indicate acquisition footprints.

1.4.2 Well log coverage:

Within our dataset, while the GR logs extend all the way from surface to the Jurassic, sonic and density logs begin in the Middle Cretaceous.

Since no resistivity data were provided, a robust fluid analysis cannot be conducted. Nevertheless, compressional and shear slowness can be combined together to detect some fluid effects.

1.4.3 Core data:

Table 1 below shows the available distal core data from each well. See text for description of intra well zone labeling.

	Well #1	Well #2	Well #3	Well #4	Well #5
No. of cores	4	1	1	2	2
Length	167 ft	90 ft	60 ft	120 ft	120 ft
Zones	TST-2, HST-2 & RST-2	HST-4	HST-4	RST-1	RST-1 & HST-4
Description	Yes	Yes	Yes	Yes	Yes
Porosity data	N/A	Yes	Yes	Yes	Yes

Overall core pictures	N/A	Yes	Yes	Yes	Partial (only core #1)
Thin section	14 slides	N/A	N/A	10 slides	N/A
Other		Core plugs report			

1.5 Method:

Figures 6 illustrate the summary workflow behind the application of an integrated Vail (depositional) and Galloway (genetic) sequence stratigraphic methodologies (Pigott and Bradley, 2014). The detailed flow chart Figure 7 illustrates the procedure followed during this study. The two principal information inputs were post-stack 3D seismic and borehole data (well logs). A "Vail" approach (detailed in Chapter 3) applied to the seismic data was the initial procedure followed by a Galloway approach (also described in Chapter 3). The results are Post-Stack Acoustic Impedance Inversion (PSAII), 3D porosity volume and quantitative interpretation. Quantitative interpretation and consequent conclusions are predicated upon the PSAII-derived 3D porosity volume as well as the interpreted motifs (Galloway and Vail) within the well logs.

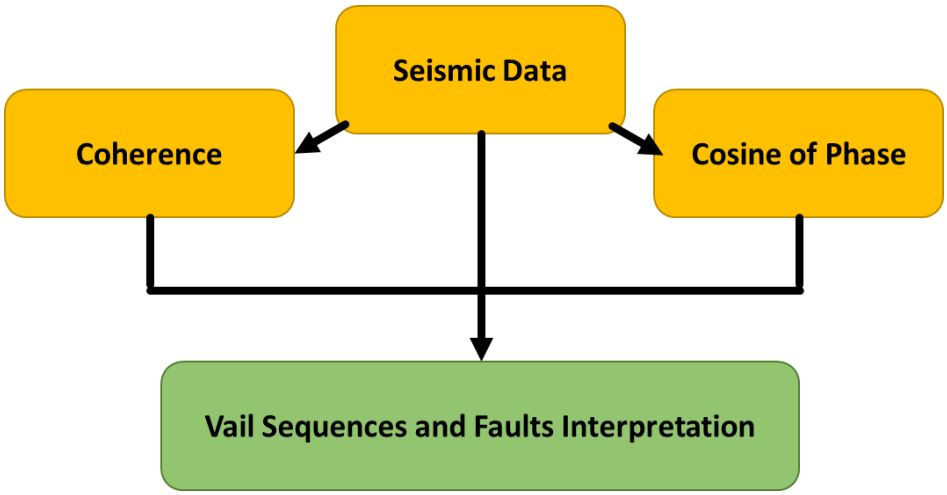

Figure 6: Main input used to conduct Vail Sequence and fault surfaces.

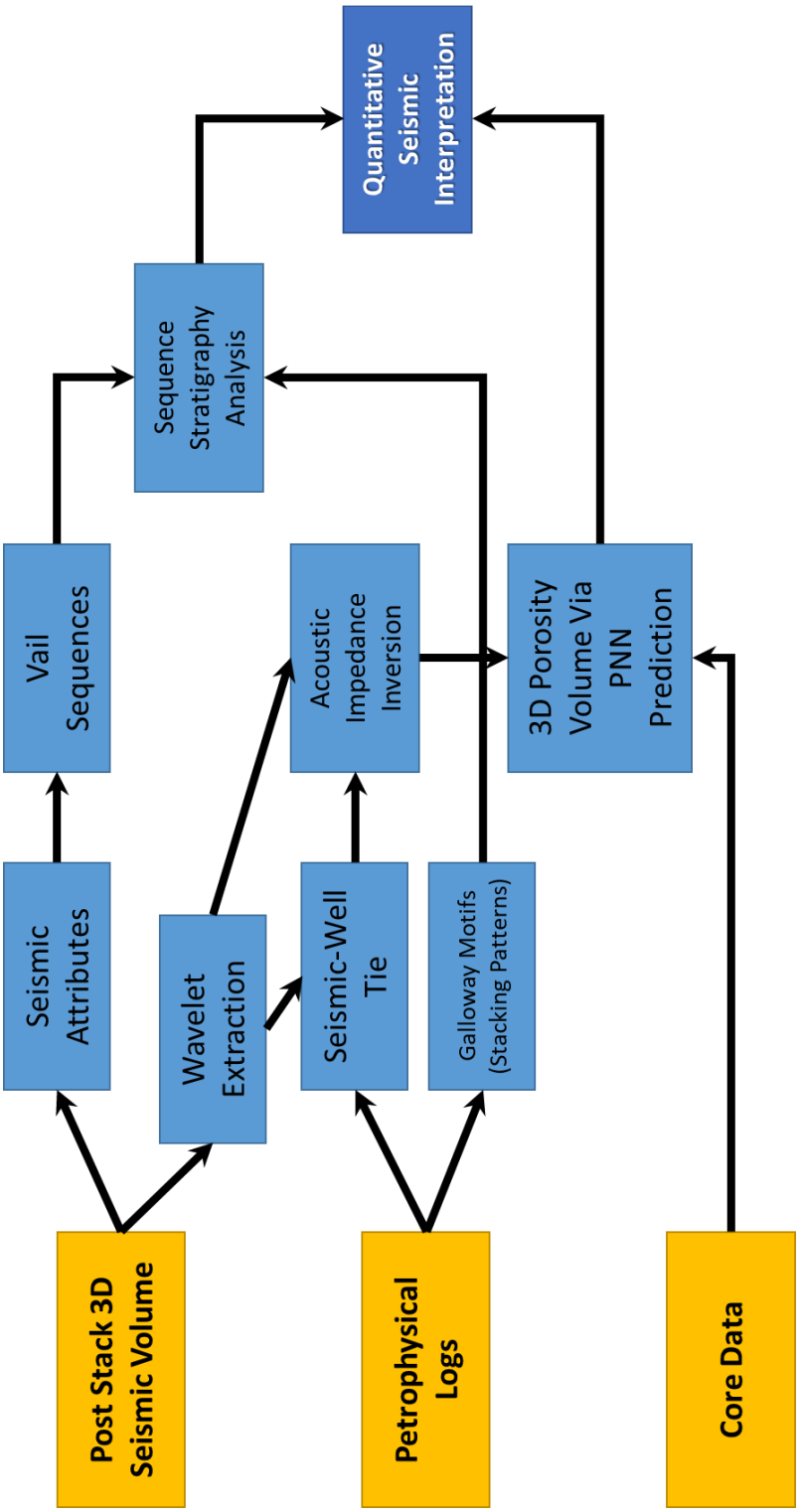

Figure 7: Detailed workflow followed to construct post-stack acoustic impedance and 3D porosity volume. These steps also aid in making the final interpretations.

Chapter 2 Geological Setting

2.1 Formation of the Arabian Plate

The Arabian Plate consists of the Arabian Shield and the Arabian Platform (Figure 2). According to Stewart (2016), the Arabian Shield is composed of Neoproterozoic oceanic island arcs and pre-Neoproterozoic continental crustal slivers. This amalgamation of terranes is dominated by a northwest-southeast fault system identified as "Najd Fault System," which has had little impact on the overlying strata (Steward, 2016). Although the Arabian Shield is dominated by the amalgamation of continental and oceanic crustal rocks with associated volcanism, the geology of the Arabian Platform is dominated by a fairly complete section of Phanerozoic sedimentary clastics and carbonate strata overlying Precambrian basins and basement as shown in Figure 2 (Konert et al., 2001).

As the study area is located solely on the Arabian Platform, the following detailed geological history will be focusing on the Platform, disregarding those other sections of the Arabian Plate.

The Arabian Plate formed in the Late Precambrian with the collision of several terranes and volcanic materials (Haq and Al-Qahtani, 2005). According to Stern and Johnson (2010), the different parts of the Arabian Plate did not stabilize at a consistent time. It is estimated that the eastern part of the Arabian Plate, identified as the Platform, stabilized around ≈ 725 Ma while the western part of the Arabian Plate, identified as the

Arabian Shield, stabilized around ≈ 570 Ma. Since then (725 Ma), the Platform had almost continuous sedimentation into the Phanerozoic with steady subsidence.

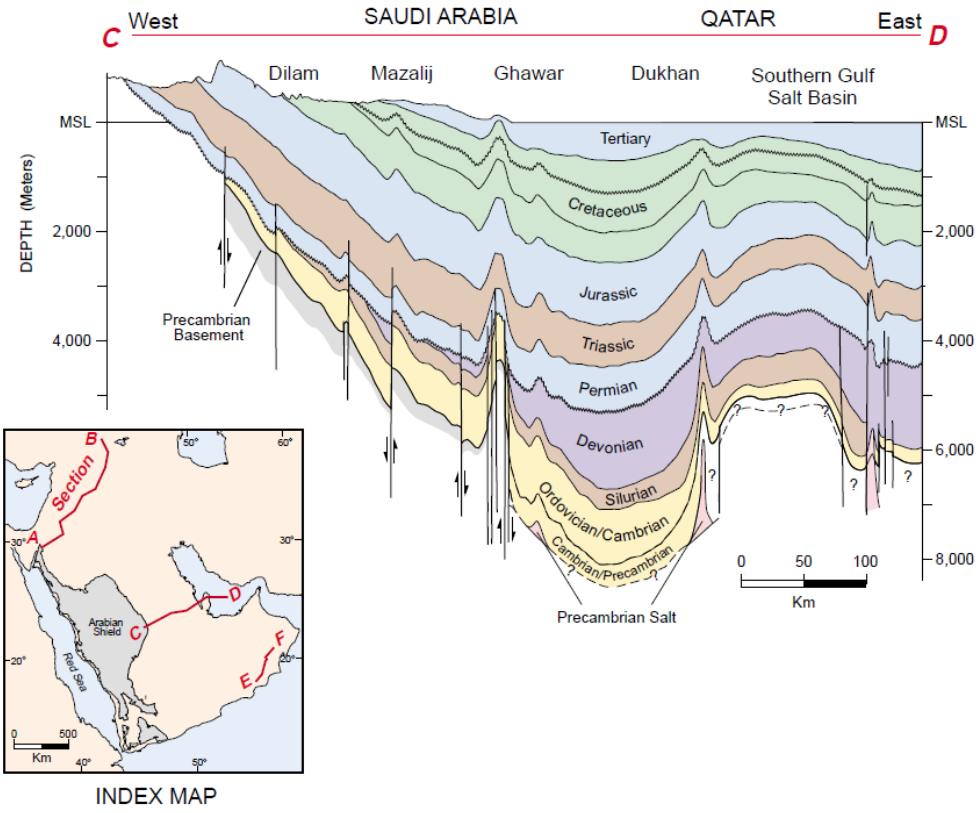

Figure 8: E-W cross section through the Arabian Plate targeting the Arabian Platform. The traverse shows preservation of the sedimentary succession in the Arabian Plate from as early as Precambrian to the Tertiary. The index map on the left shows the path of the traverse. From Konert et al. (2001).

This led to sediment accumulation on the Platform ranging from 5 to 14 km in thickness. In stark contrast, the Shield preserved its elevation resulting in little to no Phanerozoic sediment accumulation. Consequently, the crust thicknesses increase from west (35-40 km) to east (40-45 km).

During the Infra and Lower Precambrian, syn-rift basins were developed in the Platform, which resulted in the deposition of the salt (evaporites), creating the salt basins (Konert et al., 2001; Haq and Al-Qahtani, 2005; Stewart, 2016) which are shown in Figure 2. In some areas, evaporitic deposition occurred in thicknesses exceeding 1,000m. The salt deposits are believed to be the core for many of the hydrocarbon structures that originated in the Infra Cambrian era (Husseini and Husseini, 1990).

2.2 Structural Evolution and Tectonic Framework:

With the formation of the Arabian Plate and since the stabilization of the Arabian Platform, tectonic activity has been responsible for the creation and destruction of accommodation and erosional processes. Below is the summary of the events based on (Konert et al., 2001; Ziegler, 2001; Haq and Al-Qahtani, 2005; Stewart, 2016).

1. Late Precambrian: Development of rift salt basins.
2. Cambrian to Ordovician: two phases of subsidence occurred during this period that were indicated from the stratigraphic column. First, the Plate experienced gentle subsidence from the Late Cambrian to Early Ordovician. Then, during the mid-Ordovician, the subsidence rate increased leading to transgressional environments.
3. Late Devonian to Late Carboniferous: This event is called the "Hercynian Orogeny" wherein the Plate was subjected to compressional stresses, uplifting central Arabia and rotating the Plate clockwise and

tilting the Plate to the northeast. Consequently, widespread erosion occurred within the Devonian sediments, resulting in the removal of several kilometers of sediment.

4. Early Permian: Subsidence rates increased according to extension-driven crustal thinning and sediment loading processes.
5. Late Permian: The Neotethys initiates rifting and the development of a passive margin and the reactivation of arch and structures along the Plate.
6. Jurassic: the passive margin continued to develop with ongoing subsidence, furthered by the separation of the Indian Plate from Gondwanaland.
7. Cretaceous: The Indian Plate completed its separation from the Arabian Plate, causing uplift in the western part of the Platform. Furthermore, the tilt direction changed from the Northeast to East. Some of the uplifted structures underwent erosion. Overall, folds grew in the North-South direction in the west of the Platform, while the eastern part of the Platform has a Northeast-Southwest directed fold trend. Evidence suggests the folding was controlled by the Precambrian lineaments and faults.
8. Late Oligocene: The Neotethys completed its closure causing a reverse in the tilt direction and a return to the northeast. Also, the Red Sea

started to open during this period. However, it had no impacts on the structural evolution of the Arabian Platform.

Figure 9 shows the paleolatitude position of the Arabian Plate through time, beginning in the Late Pre-Cambrian and continuing up through the Jurassic. Moreover, Figure 9 illustrates the rotation of the plate through that period.

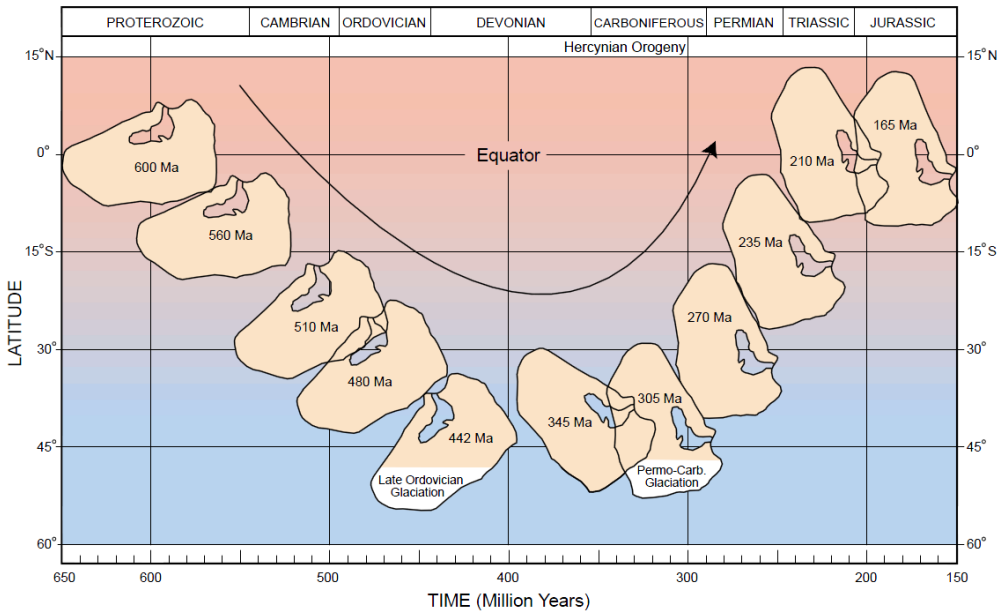

Figure 9: The Arabian Plate paleolatitude location during the Paleozoic. From Ordovician to Carboniferous, the Plate rotated nearly 90º clockwise. Since the Permian, the Plate has remained within the optimum carbonate zone (between ±30º latitude). From Konert et al. (2001).

According to Stewart (2016), the north-south basement faults in the Arabian Platform have a spacing of approximately 100 km. This conclusion is based on the reflection seismic, gravity, and magnetic data used to study the structural evolution

from the Late Precambrian to Neogene specifically in the Rub' Al-Khali area within Saudi Arabia. Also, the study asserted that the structures are transpressional folds based on the available regional seismic data.

The distribution of Infra-Cambrian salt basins in the Arabian Platform is controlled by the Dibba Fault, Oman Salt basins and the Wadi al Batin lineament. These three-faults trends form the base for the later deformation by being reactivated (Ziegler, 2001). Figure 10 shows the principal horizontal stress direction for each period (Marzouk and Sattar, 1993).

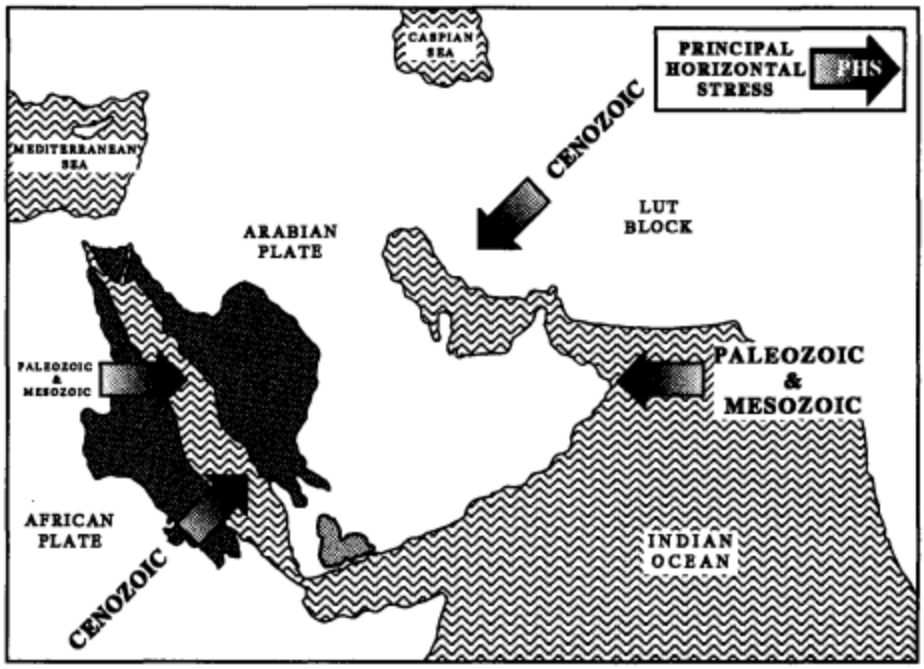

Figure 10: Principal horizontal stresses for the Arabian Plate during Cenozoic, Paleozoic and Mesozoic. Taken From (Marzouk and Sattar, 1993).

2.3 Accommodation Development and Eustasy Effects:

For the eastern portion of the Arabian Plate, the main control governing the creation of accommodation is subsidence (Stewart, 2016)**.** Overall, changes in sea level, also have controlling effects up on the accommodation space either positively by subsidence or negatively by depositional hiatuses or erosional unconformities (Pigott and Bradley, 2014). Furthermore, as the relative sea level curve cycle chart can provides important information about diagenesis and reservoir quality through exposure duration, Haq and Al-Qahtani (2005) studied the regional cycles of the relative sea-level changes in detail and below is a summary of their findings:

- The duration of major hiatuses in sedimentation on the Arabian Platform based on the cycle chart are:

    1. Carboniferous (25 My duration) due to the Hercynian Orogeny.
    2. Late Triassic through the Early Jurassic (20 My duration) because of the breakup of Gondwana, and
    3. Oligocene (10 My duration) owing to the closure of the Neotethys Ocean and the collision of the Arabian Plate with Eurasia.

Some minor hiatuses owing to changes in relative sea level such as in the Late Eocene because of ice cap buildups in Antarctica.

- Many of the Arabian Platform sequences may represent third-order or even higher-order cycles.
- Throughout the geological column, the cycle chart was matching the globe in some periods and discriminated in other periods. For example, the glaciation in the Late Ordovician caused global sea level to fall. However, constructing the cycle chart for the Late Carboniferous is challenging owing to the long hiatus attributed to the Hercynian Orogeny. However, the overall Arabian Plate cycle chart is very similar to the globe cycle chart.
- Relative sea level is the main contributor to the sedimentary patterns.

Al-Husseini (2011) posited the existence of another major hiatus in sedimentation occurring at the base of the Cambrian, which was later confirmed by Stewart's (2016) seismic investigations. Both Al-Husseini and Stewart considered this break to be one of the most significant in the stratigraphy of the Arabian Platform. Still, there remains little evidence for determining the exact age, though research in the Arabian Shield suggests the timing of the event occurred in the Late Ediacaran. The main cause of this hiatus is currently associated with the assembly of Gondwana.

The giant oil fields in the Arabian region have been classified into two main categories based up on the tectonic events that led to the evolution of the structural component in the fields. The two classifications are: 1) rift-controlled, located in the

eastern side of the Plate, and 2) passive margin controlled, located in the western side of the Plate and in the Arabian Gulf (Mann et al., 2000).

Chapter 3 Sequence Interpretation

3.1 Basic Concepts

The history of the development of sequence stratigraphy, especially as pertains to its practical application, has been summarized by Pigott and Bradley (2014). A stratigraphic sequence involves genetically related strata bounded by unconformities or correlative conformities from the upper and lower boundaries (Vail and Mitchum, 1977). Mitchum et al. (1977) defined unconformity, conformity and hiatus as the following:

> "An unconformity is a surface of erosion or nondeposition that separates younger strata from older rocks and represents a significant hiatus. A conformity is a surface that separates younger strata from older rocks, but along which there is no physical evidence of erosion or nondeposition, and no significant hiatus is indicated. A hiatus is the total interval of geologic time that is not represented by strata at a specific position along a stratigraphic surface."

From an approach that emphasizes deposition rather than erosion, stratigraphic units are generated from repetitive episodes of progradation, transgression and flooding events. As a consequences maximum flooding surfaces or hiatal surfaces represent the boundaries for the units that also form the starting point of each Galloway cycle (Galloway, 1989). He identified three factors that affect the stratigraphic architecture as 1) sedimentation rate, 2) subsidence rate, and 3) eustatic sea level change. However, Galloway recognized that "stratigraphic architecture is very similar regardless of the dominant control." Eustatic sea level change also controls the distribution and facies of the sequences as its fluctuates both globally (regionally) and locally (Mitchum et al.,

1977). Given the cyclicity observed in stratigraphiy from the repetitive nature of events, sequences can be predicted to a considerable degree. Thus, the goal of sequence analysis is to differentiate between the sequences, determine where individual sequences lie, and for applied purposes of hydrocarbon exploration predict important reservoir properties such as porosity and organic content.

Both the Vail and Galloway methods are linked through seismic well tie so as to complement each other, such that the Vail approach is applied on seismic data while the Galloway approach is applied to the borehole data. Borehole data provide a high resolution of variations vertically within the borehole path. In contrast, seismic data provides excellent lateral resolution of the variations for regional correlation where borehole data prove too localized. Refer to Pigott and Radivojevic (2010) for more examples using this method. In comparison to petrophysical logs, Vail sequences are more easily detected by seismic as they are based on unconformities, constituted by abrupt changes in lithology that manifest as sharp contrasts within acoustic impedance data. By comparison, Galloway sequences are more easily detected on borehole data (especially Gamma Ray logs) as the cycles start by flooding surfaces which are associated with organic-rich deposits.

3.2 Seismic Stratigraphy

Before applying the Vail approach to the seismic reflection data, it is important to understand the constraints of the data. “Primary seismic reflections are generated by

physical surfaces in the rocks, consisting mainly of stratal (bedding) surfaces and unconformities with velocity-density contrasts" (Vail and Mitchum, 1977). Vail et al. (1977) recognized that physical surfaces follow time-stratigraphic correlation rather than lithostratigraphic correlation. Furthermore, lithology cannot be determined directly from the seismic reflection data. Vail et al. (1977) listed eight interpretations based directly on the reflection data: "(1) Post depositional structural deformation and thickness changes, (2) Geologic time correlations, (3) Definition of genetic depositional units, (4) Depositional topography, (5) Paleo-bathymetry, (6) Burial history, (7) Relief and topography on unconformities, and (8) Paleo-geography and geologic history." For many years, seismic data have been used strictly for structural evaluation. However, since the development of seismic stratigraphic methodologies, more specifically the "geologic approach to the stratigraphic interpretation of seismic data" as defined by Vail and Mitchum (1977), more complex usage for the data had occurred. Seismic stratigraphy may be applied to predict depositional environments and investigate the presence of stratigraphic traps, especially where borehole data are limited. However, a holistic understanding of depositional environments is necessary to maximize the efficacy of the analysis (Brown and Fisher, 1977). The seismic sequences are based on the identified stages per Mitchum and Vail (1977). Ten seismic lines were selected for the initial application of detailed seismic stratigraphy analysis (Figure 11).

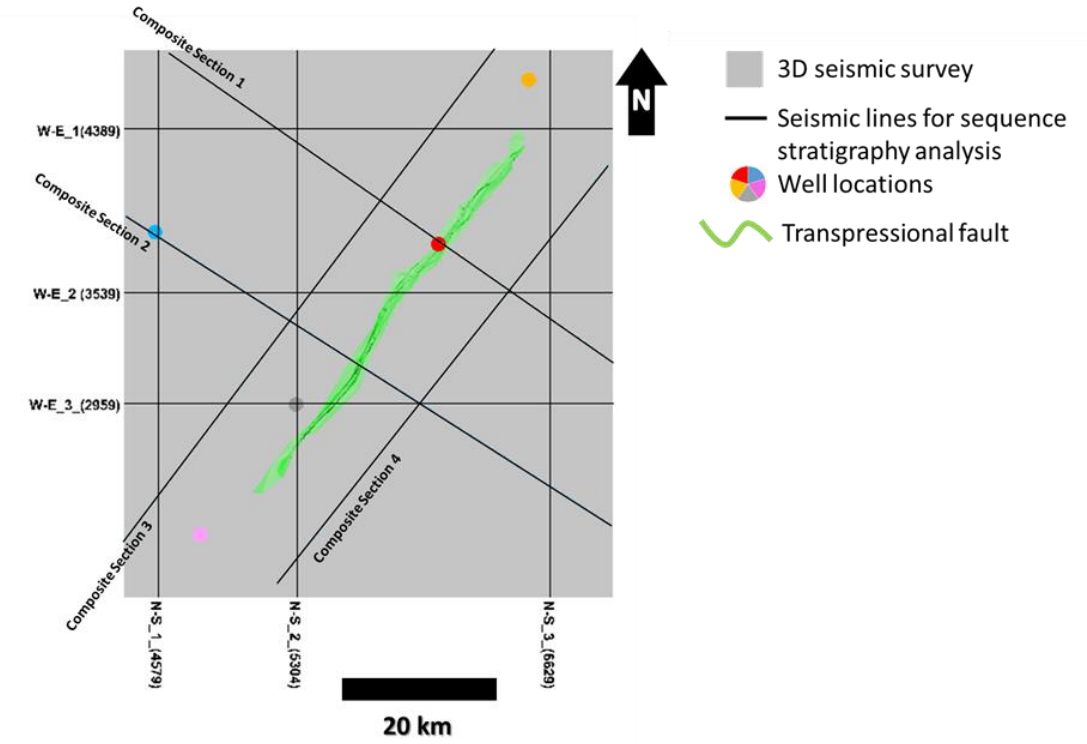

Figure 11: 3D seismic survey limits are shown by the gray area along with the well location. Black lines represent the chosen seismic lines and composites to apply detailed seismic stratigraphy analysis.

The ten lines consist of three Inlines (E-W orientation), three Xlines (N-S orientation), and four arbitrary composite section lines (2 NE-SW and 2 NW-SE orientations). The workflow for seismic sequence analysis is broken down into five steps across three stages: recognition, correlation, and age determination:

1. Faults are interpreted across the seismic section.

2. Terminations (onlap, downlap, toplap and truncations) are marked.

3. Operational sequence boundaries (parasequence sets via the method of Pigott and Radivojevic (2010)) are interpreted based on the terminations.

4. Operational sequence boundaries interpretation are extended over the seismic volume.

5. Operational sequence boundaries are correlated to the pre-interpreted wells based on Galloway sequences to predict the age of the sequence boundaries.

By implementing the above steps, thirteen seismic operational sequence boundaries based on the marked terminations were distinguished. The thirteen interpreted operational sequences consist of one sequence in the Cenozoic, three Cretaceous, six Jurassic, two Triassic, and one Permian operational sequences.

Future work could be done on the terminations to distinguish between the sequences boundaries to determine whether they are a non-depositional hiatus or an erosional hiatus. Non-depositional hiatuses are indicated by onlaps, downlaps, and toplaps, while erosional hiatuses are indicated by truncations (Mitchum et al., 1977). Thinning of a unit can create a false termination due to the tuning effect, a limitation of seismic reflection data pertaining to wavelength behavior and resolution. Thus, to mark any sequence boundary, at least two terminations shall be marked before an operational sequence boundary is set. Likewise, if an interpreted operational sequence boundary is interpreted on a seismic section, then that sequence boundary may be extended onto the intersected seismic section, regardless of a lack of mapped terminations.

The zone of interest is confined between J2 and J6. During this stage of analysis, borehole data input is constrained to define the zone of interest. Thus, the operational sequences at this stage are interpreted without assistance or guidance from the well tops or sequences.

The interpreted faults are classified and color-coded into five groups based on their ages (youngest age on top after the methods of (Pigott and Abouelresh, 2016)). Table 2 illustrate the ages and the color for the interpreted faults.

Fault's color	Age of the fault
Black	Permian or older
Dark brown	Triassic
Brown	Jurassic
Orange	Cretaceous
Light Yellow	Cenozoic

Table 2 shows the classifications categorize for the interpreted faults.

Certain patterns can be observed from the fault interpretation: 1) there are no interpreted faults between Early Jurassic and Late Triassic, 2) faults within the zone of interest are confined to the zone. In addition, a major NE-SW transpressional fault, extending for nearly 60 km, cross-cuts the entire Jurassic period (interpreted with light green) creating four-way-closure in that interval. Borehole data are clustered in the western flank of the faults. Given the lack of borehole data in the area, difficulties in

interpreting the east side of the fault occur. Note that the ages below the Middle Jurassic are predicted based on the regional geologic understanding and not borehole data owing to the lack of available borehole penetration.

Upper boundary terminations (truncations and toplaps) are in yellow, while lower boundary terminations (onlaps and downlaps) are in red. 3D seismic attributes aided in identifying, recognizing and interpreting faults and terminations. The attributes includ coherence, cosine of phase and curvature. The seismic attributes were generated using PETREL and AASPI. PETREL's ant track model was used as a secondary method to quality control the manual fault interpretations. These attributes were selected based on several studies (Pigott et al., 2013; Abidan, 2015) that highlight their efficacy in detecting and aiding in the interpretation of targeted structural features. In addition, the seismic volume was preconditioned using an amplitude spectral balancing program in AASPI. Spectral balancing broadens the seismic data making it easier to detect faults (Chopra and Marfurt, 2016; Milad et al., 2018). Figure 12 shows the amplitude spectrum before and after spectral balancing. In our dataset, this procedure posted the amplitude of the frequencies that are higher than 40 Hz, allowing for increased accuracy in the mapping of terminations. Also, the spectrally balanced data yielded higher resolution post-acoustic inversion, which will be discussed in the next chapter. Interpreted faults, terminations, and sequence boundaries are shown in Figures 13 to 18.

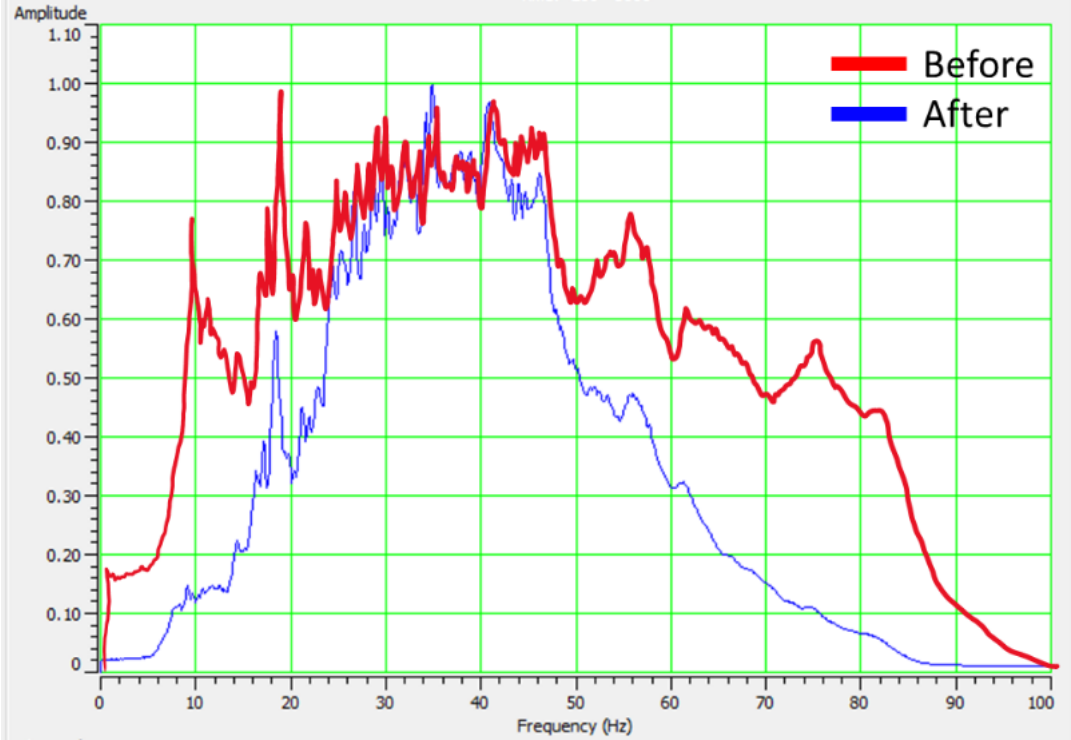

Figure 12: Seismic amplitude spectrum before (blue) and after (red) applying spectral balancing. Overall, the frequency content is broadened after applying spectral balancing.

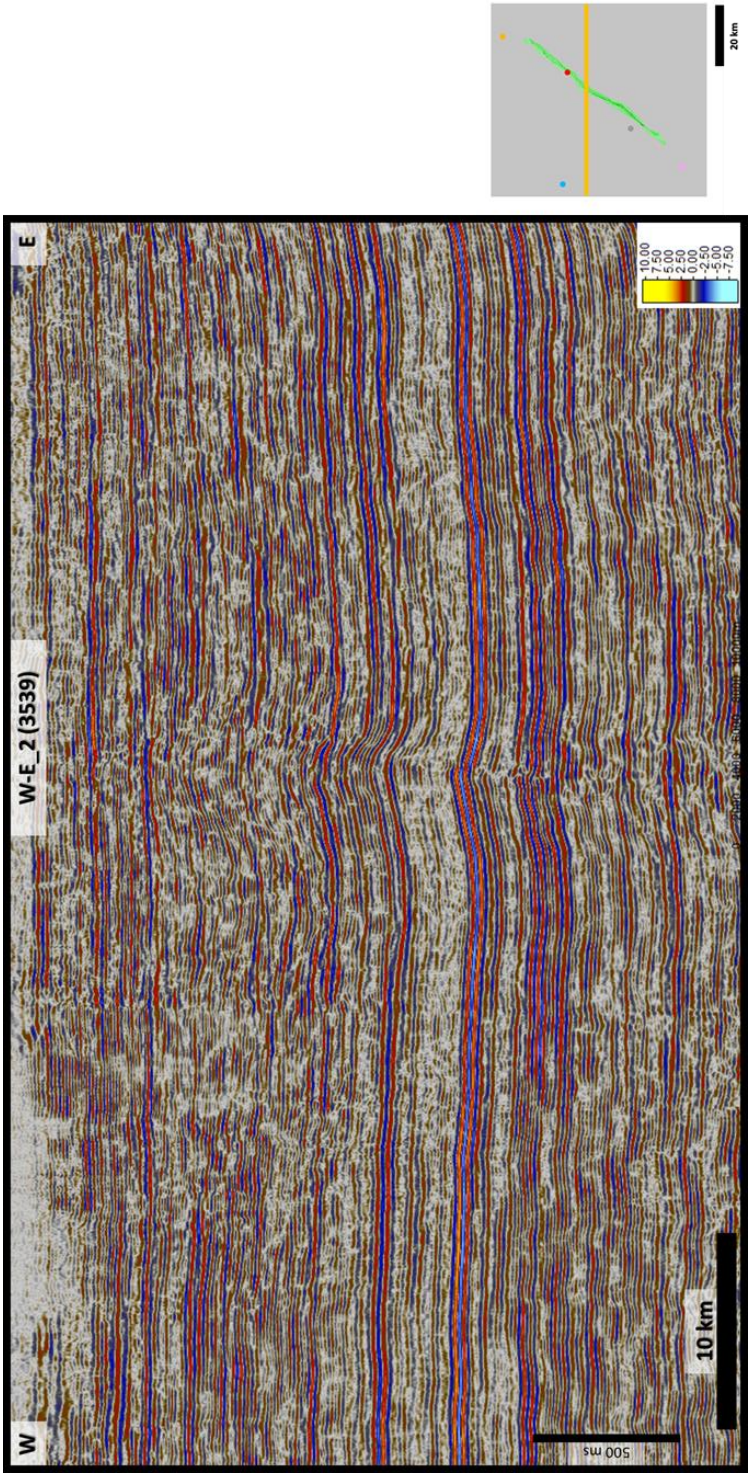

Figure 13: Uninterpreted E-W inline # 3539 seismic section as shown in the index map on the bottom right corner.

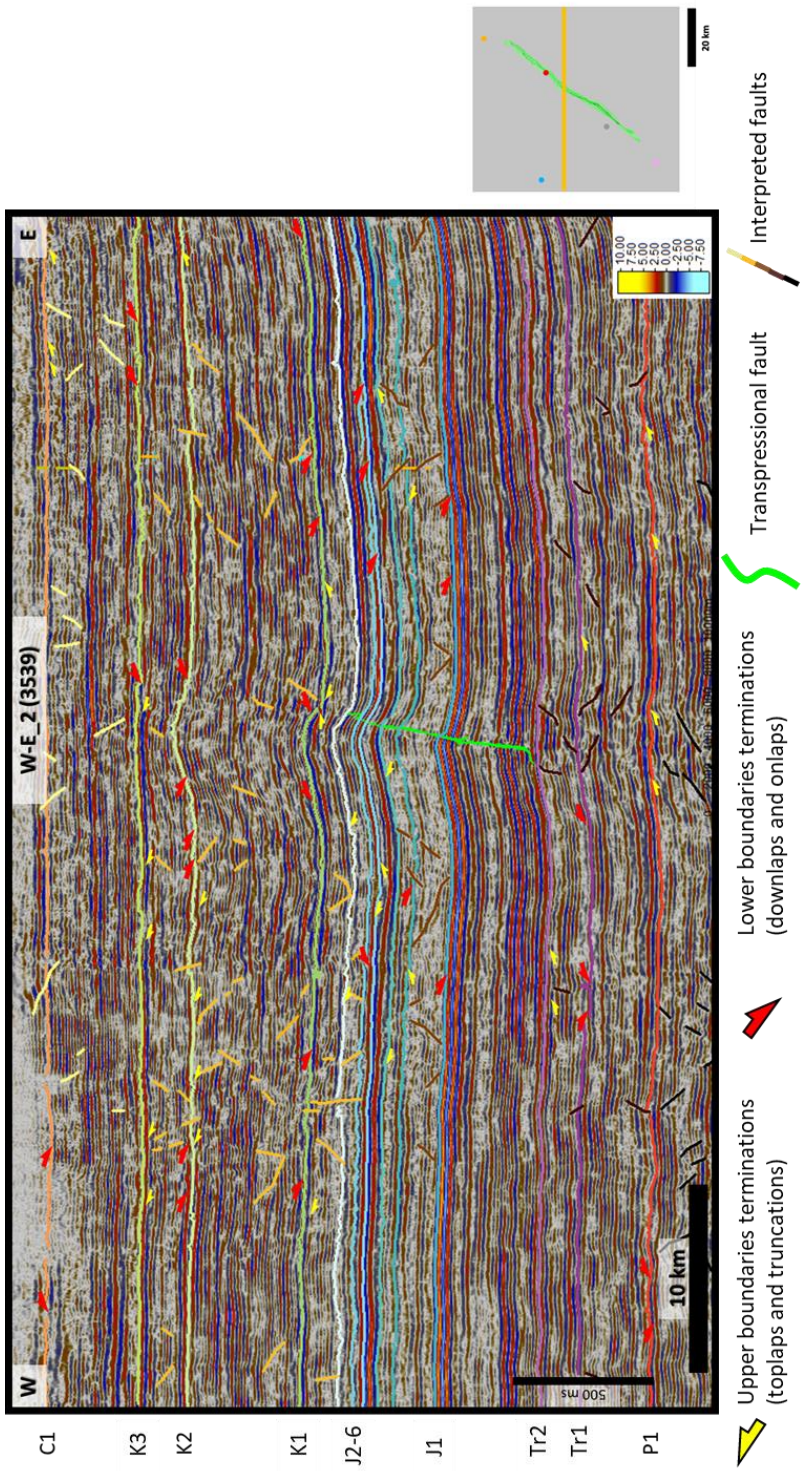

Figure 14: Interpreted E-W inline # 3539 seismic section as shown in the index map on the bottom right corner. Thirteen interpreted sequence boundaries are shown along with the upper and lower terminations. The five sets of the faults are also shown.

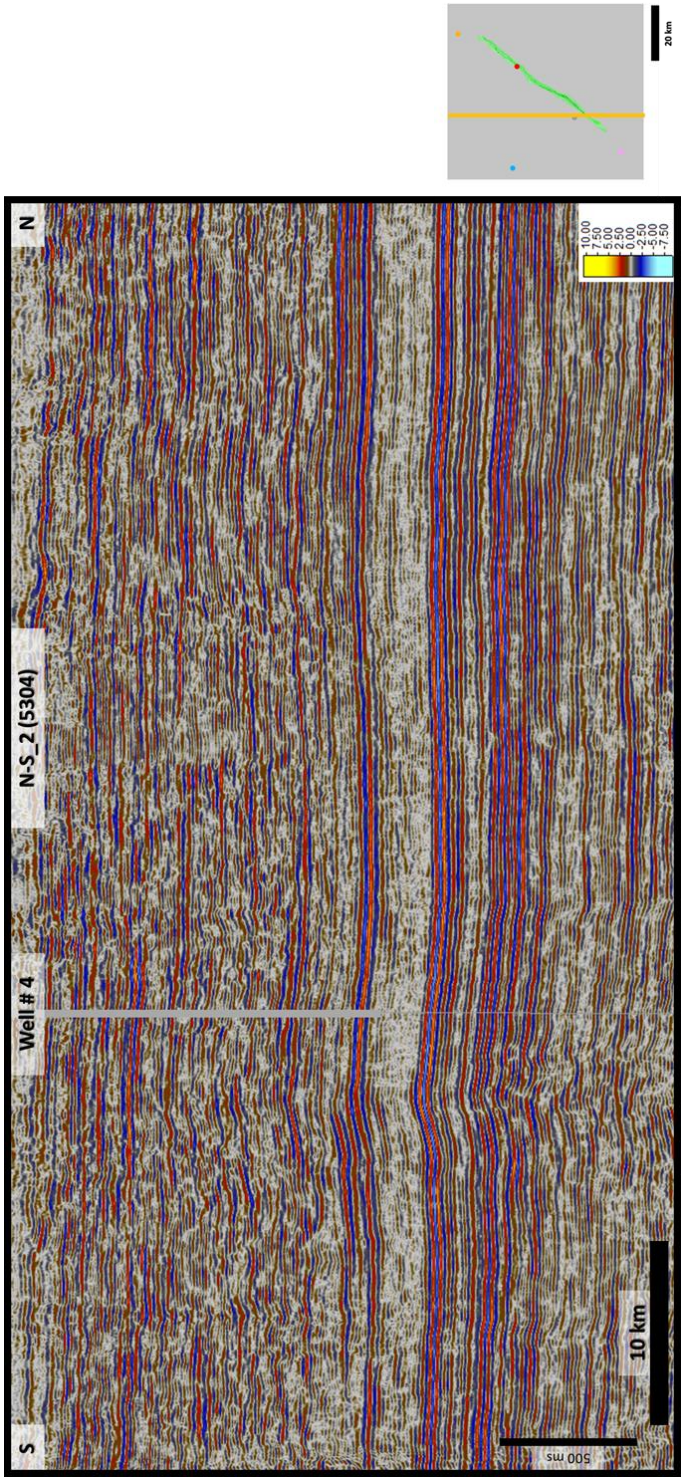

Figure 15: Uninterpreted N-S xline # 5304 seismic section as shown in the index map on the bottom right corner.

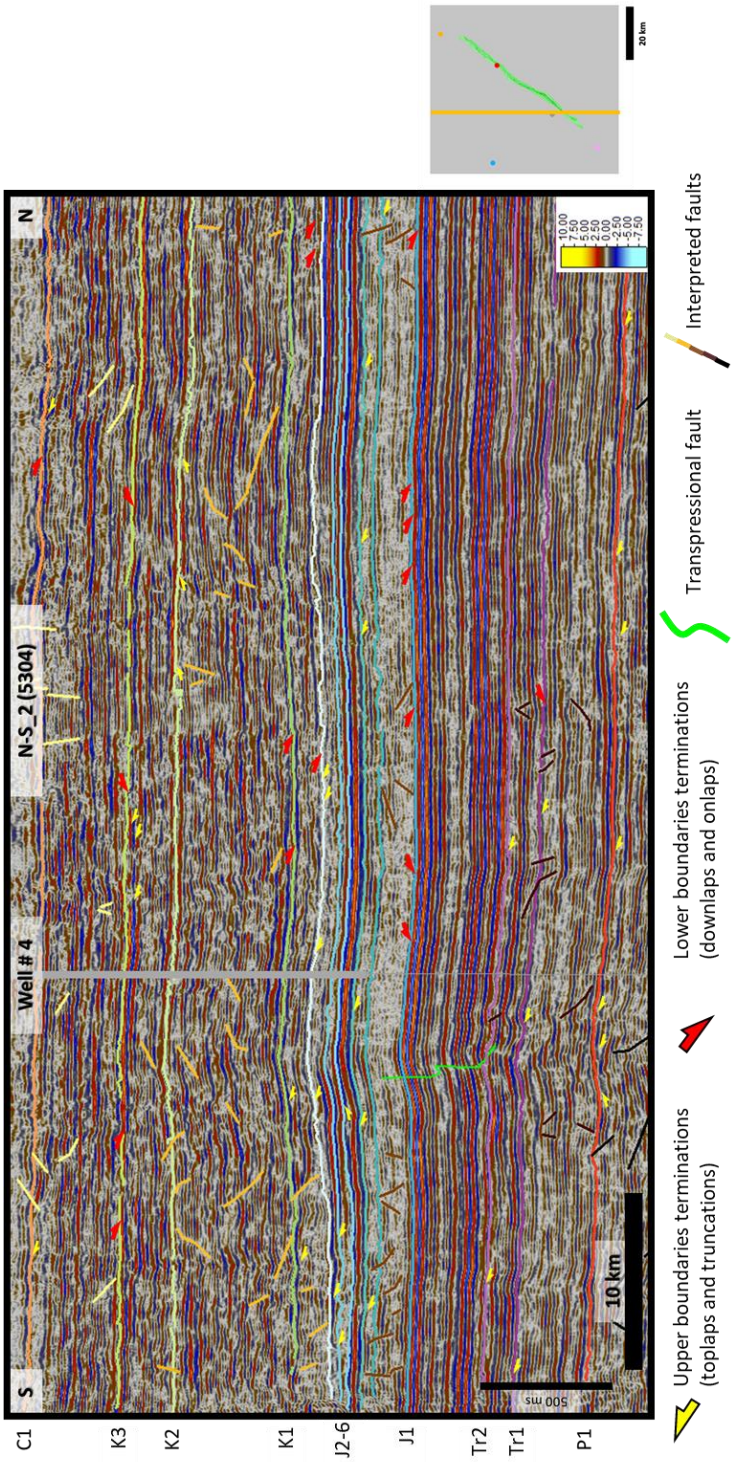

Figure 16: Interpreted N-S xline # 5304 seismic section as shown in the index map on the bottom right corner. Thirteen interpreted sequence boundaries are shown along with the upper and lower terminations. The five sets of the faults are also shown.

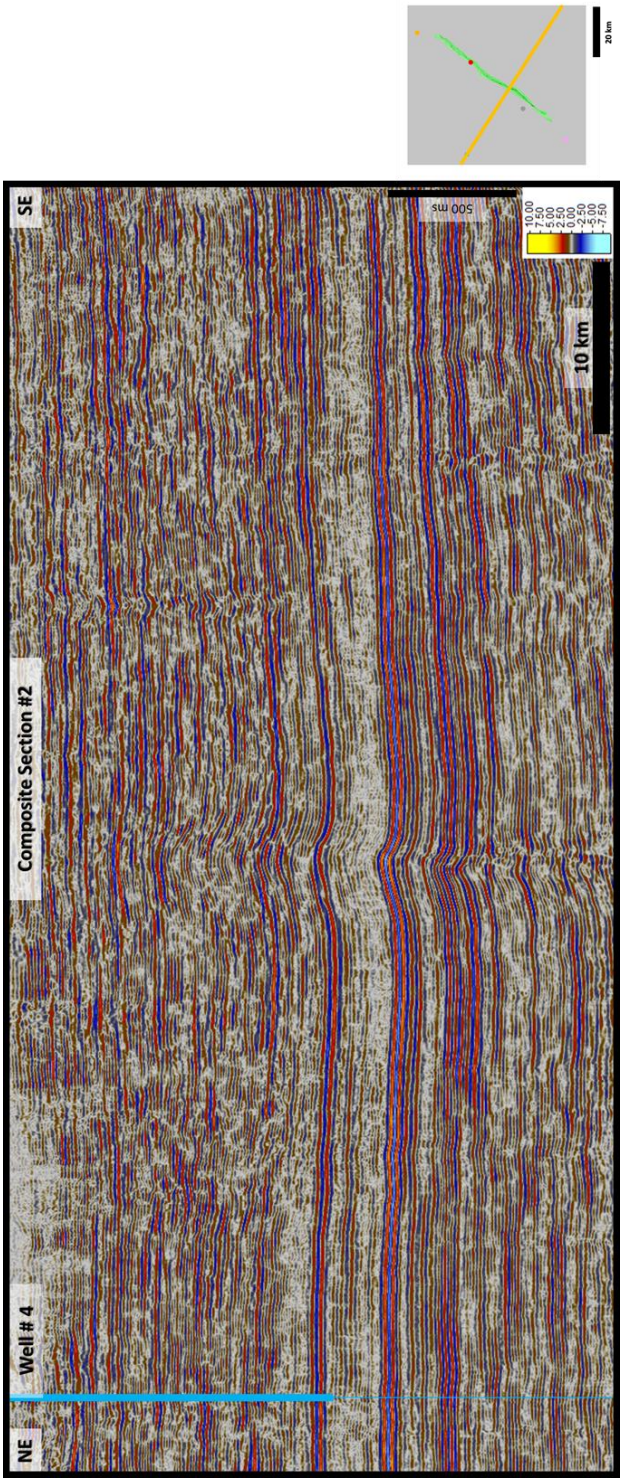

Figure 17: Uninterpreted NW-SE composite seismic section #2 as shown in the index map on the bottom right corner.

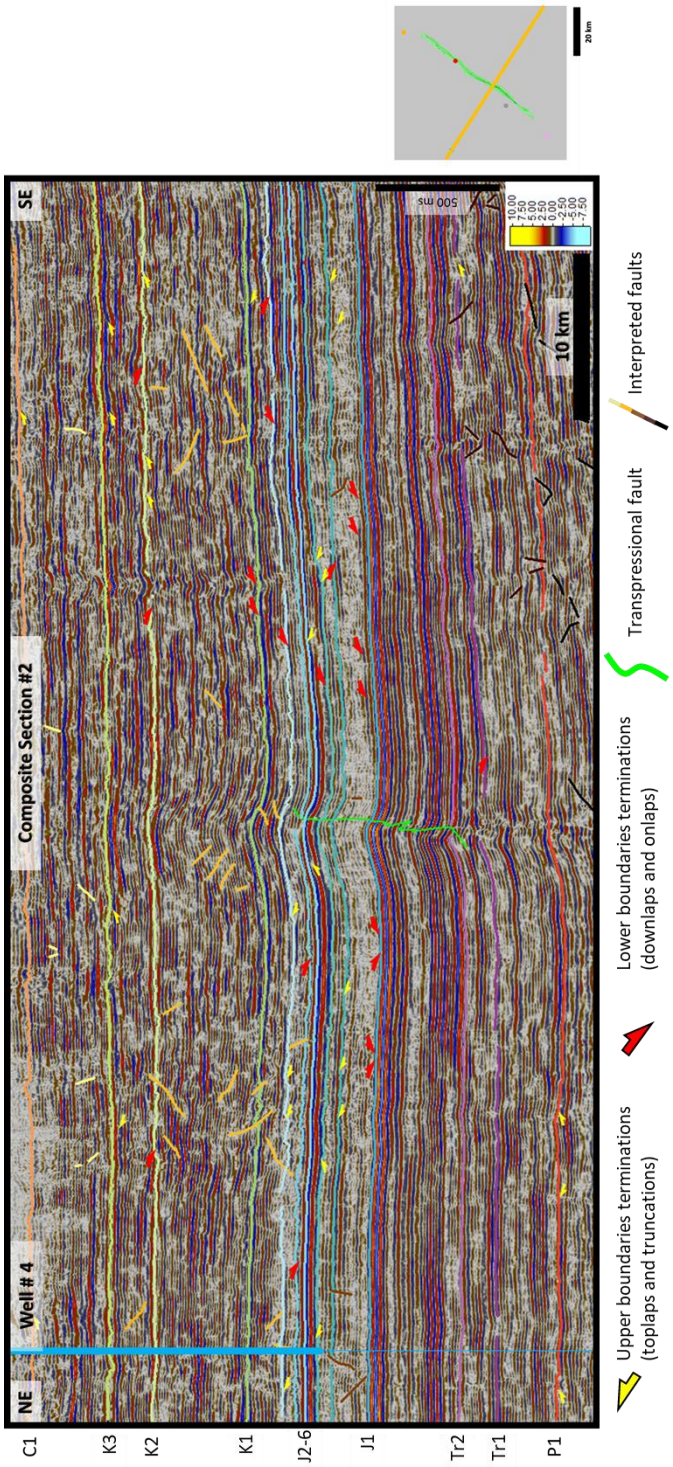

Figure 18: Interpreted NW-SE composite seismic #2 as shown in the index map on the bottom right corner. Thirteen interpreted sequence boundaries are shown along with the upper and lower terminations. The five sets of the faults are also shown.

Seismic facies analysis is performed based on the seismic attributes, however the lateral variations in the depositional environments appear to be minimal. The observed clinoforms are wide, 30 - 40 km, and have a very gentle dipping angle.

3.3 Well Stratigraphy

Galloway (1989) worked on clastic depositional environments and constructed his method based on the basic concepts of Frazier (1974). His techniques is modified for application to carbonates. For example, his flooding surface, mostly shale indicative of low depositional environment, is considered as a flooding surface approaching a Highstand Systems Tracts (HST) component, while for carbonate HST deposits are expected to include grainstone because of the enhanced process-energy (Pigott, unpublished sequence stratigraphy class notes). For Galloway, a sequence boundary is a regionally extensive mudstone or shale that represents sediment starvation, hence the usually appropriated name: condensed section. Mudstone, a low-energy deposit equivalent to shale in clastic systems, is deposited during Lowstand Systems Tracts (LST). While Galloway placed little importance on eustatic sea level change, this study, conducted on a restricted carbonate system, directly accounts for the role of relative sea level on evolving carbonate depositional systems. Figure 19 shows the relationship between the eustatic sea level change with the depositional system tracts (Pigott and Bradley, 2014). Note that the regressive Systems Tract “RST” was incorporated into this study based on Pigott et al. (2012) which is a cyclical opposite of the Transgressive Systems Tracts (TST).

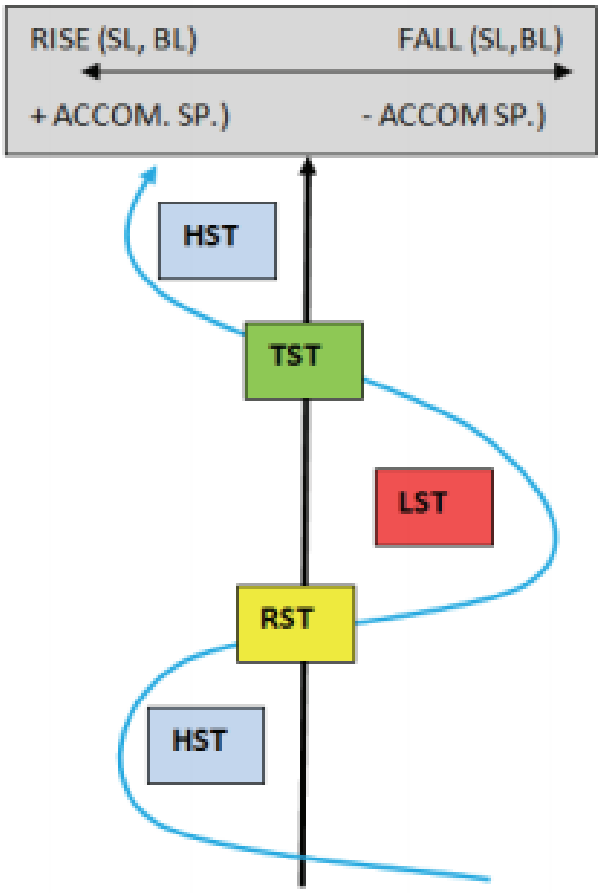

Figure 19: Effects of eustasy on the deposited system tracts. From Pigott et al. (2012).

One may identify and classify the parasequence sets (HST, RST, LST and TST) through an investigation of Gamma Rays (GR) logs from the borehole data as illustrated in the model in Figure (20) if these Jurassic carbonates are responding in similar fashion to those of reciprocal sedimentation of the Permian of West Texas (Crosby, 2015). Figure (21) shows the interpreted cycles based upon the approach provided by Pigott (2018 unpublished Sequence Stratigraphy class notes) in the five wells. The area of interest is Middle to Late Jurassic ≈ 15 ma. Four cycles are interpreted, all of which

may be understood as third order. However, the well number 2 has an interpreted lower order cycle within the older cycle. The boundary between HST and RST represents a definitive boundary while the rest are subjective as it is an unconformity. Therefore, this boundary would match Vail sequences as it is easily detected by seismic data due to the acoustic impedance contrast. In addition, it is expected to interpret upper boundary beneath it (truncations). Furthermore, the boundary between RST and LST is the most challenging and difficult boundary to pick. In the next chapter, cross plots that support the classification scheme for the system tracts are shown. The first interpreted unit is a TST (mainly because of the data coverage). Therefore, the cycle numbers begin with the TST as the base and end with a LST as the top. As the top picked anhydrite may represent both RST and LST, it may be considered as a continuation of the cycle #4.

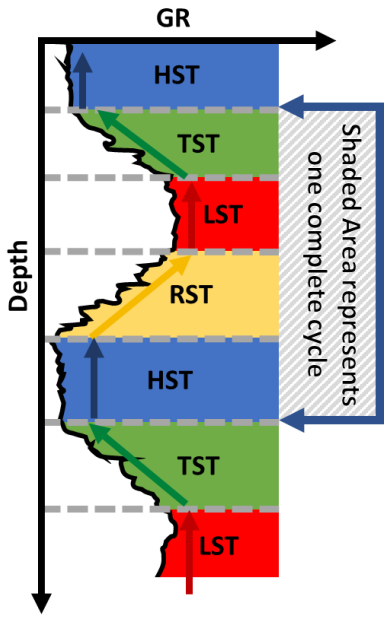

Figure 20: illustration showing the procedure to pick up the system tracts based on the GR log. A complete cycle has TST, HST, RST and LST. After Pigott (2018)

(unpublished Sequence Stratigraphy class notes with respect to the Permian of West Texas)

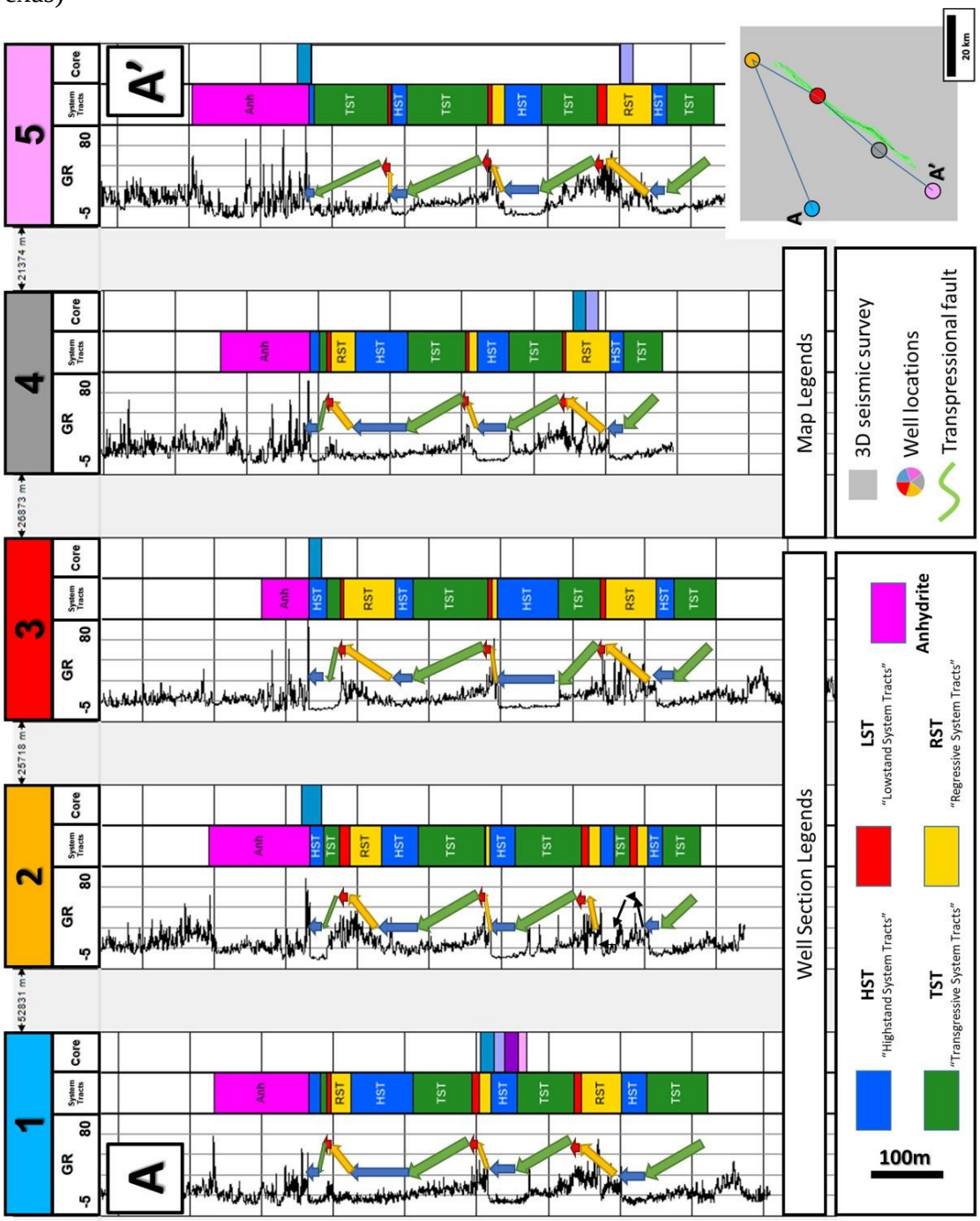

Figure 21: Well log cross section as shown in the index map on the bottom right corner. The tracks represent GR logs, interpreted system tracts and core location.

3.4 Seismic-Well Tie

In order to link interpretations using both Vail and Galloway (seismic and well) sequences, the borehole data are tied to the seismic data. This essentially allows for the incorporation of well data into seismic data. For example, biostratigraphic data may be incorporated to assign ages to the interpreted horizons. Moreover, sonic and density logs may be used to generate impedance logs and the resulting impedance logs are utilized in seismic inversion to link the seismic data to geology.

The five wells were tied to the seismic using sonic and density logs. A statistical wavelet is generated as shown in Figure (22). Table (3) shows the correlation coefficient and analysis window of tied wells. I have not edited or conditioned any logs through the process. Nevertheless, some of the logs were edited/conditioned before accessed to the dataset.

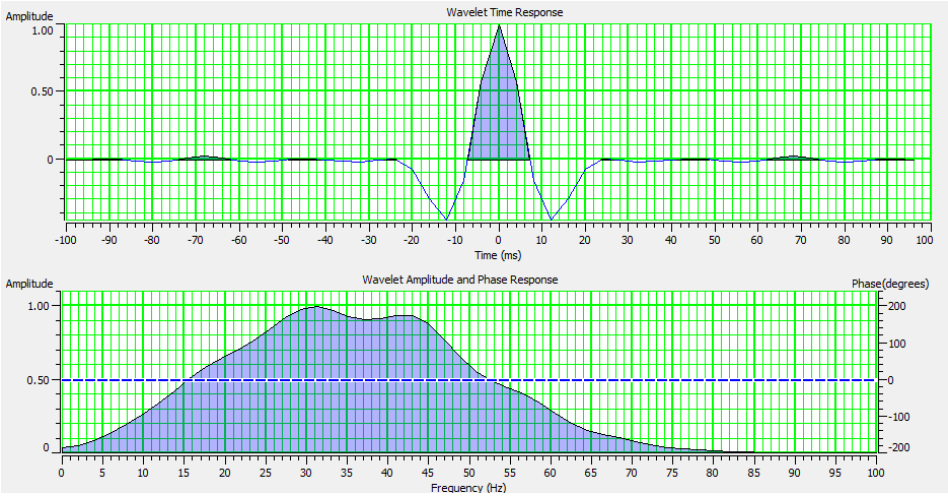

Figure 22: Statistical wavelet generated from the well logs between 700 to 1700 ms with 200 ms window length.

Well Number	Correlation Coefficient	Analysis Window
1	77%	600 ms
2	61.9%	550 ms
3	72.4%	450 ms
4	75.7%	400 ms
5	57.1%	350 ms

The zone of interest from the well section is shown in seismic section Inline #2274 through Well #5 Figure (23). Furthermore, Figure (23) shows the correlation of the interpreted seismic sequences (J1, J2, J3, & J4) with their correspondent system tracts cycle from the wells. J1 is interpreted on a peak while the other operational sequence boundaries are interpreted on zero crossings. This explains why the seismic operational sequence boundaries are slightly above the well's parasequence sets. Zero crossing are chosen as they provide more precise mapping when compared to either the peaks or troughs. However, to extract any seismic properties, time shifting the horizon facilitated accuracy.

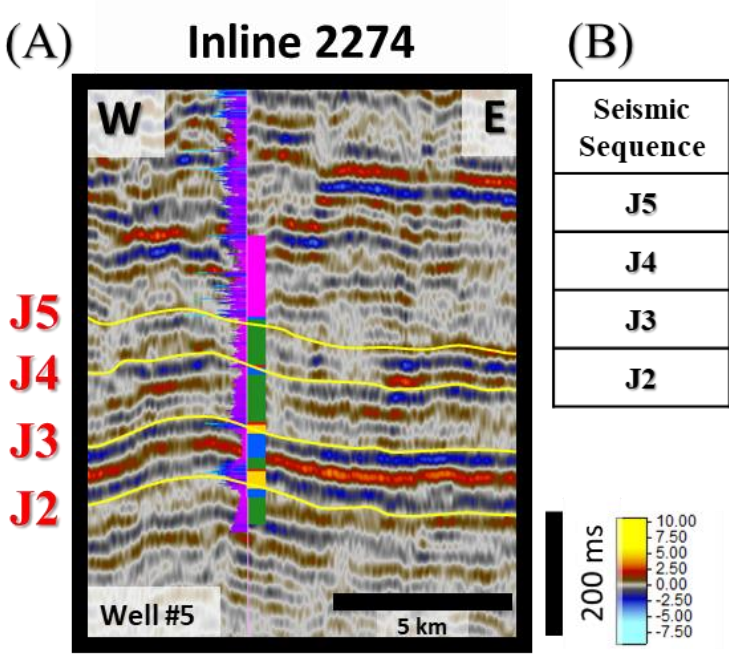

(B)

Seismic Sequence	System tract
J5	HST-4
J4	HST-3
J3	HST-2
J2	HST-1

Figure 23: (A) Inline #2274 through Well #5 with the interpreted operational sequence boundaries targeting the zone of interest. **(B)** Correlation of the operational sequence boundaries to the interpreted parasequence sets colors correspond to legend shown in figure 21.

Noting the well location, and thus proximity to the transpressional fault, remain of vital importance to interpretation. Interpreted sequences and any further analysis e.g. porosity predictions have higher confidence on the western side of the seismic volume in comparison to the eastern side.

Chapter 4 Quantitative Interpretation

4.1 The Procedure

Following the theory and methods of Caf and Pigott (2016), quantitative seismic stratigraphic interpretations for both the borehole data and seismic data were applied. Petrophysics and rock physics link the seismic data and borehole data together so as to predict the formation properties through seismic-well tie. The logic behind the procedure was perhaps best espoused by Avseth et al. (2005) who said "The seismic reflections are physically explained by contrasts in elastic properties, and rock physics models allow us to link seismic properties to geologic properties". Consequently, petrophysics is used to predict 1D total porosity using the core data and well logs, and provide insight to lithology, such as differentiating between limestones and dolomites. Furthermore, the core data has been applied to the quality control of the interpreted system tracts. Therefore, an investigation upon potentials determines the effects of diagenesis on primary and secondary porosity is made, based upon petrophysics and utilizing neural network training.

4.2 Petrophysical Quantitative Interpretation

4.2.1 1-D porosity prediction

Since access to porosity data is limited to the core section where it was measured from the core plugs, porosity logs may be predicted using different methods.

Four different methods have been tested to calculate the porosity. The resultant porosity logs are plotted against the core porosity to determine the best approximation for later use in porosity prediction via probabilistic neural networks across the entire seismic volume.

The porosity can be predicted using 1) sonic (compressional slowness) log only, 2) bulk density log only, 3) sonic (compressional slowness) and neutron density logs, 4) bulk density and neutron density logs, and 5) sonic (shear slowness) log. The first 4 methods were used while the last one sonic (shear slowness) is eliminated from the testing as its results proved unrealistic (it calculated porosity up to 100%). Below are the equations used to calculate the different porosity curves, for more details please refer to Techlog manual (Schlumberger, 2017):

1- Sonic Log Porosity:

$$\Phi = \frac{\Delta_t - \Delta_{t_{ma}}}{\Delta_{t_f} - \Delta_{t_{ma}}}$$

2- Bulk Density Log (RHOB) Porosity:

$$\Phi = \frac{\rho_{ma} - \rho_B}{\rho_{ma} - \rho_f}$$

3- Sonic and Neutron Density Logs Porosity:

$$\Phi = \frac{\Phi_{Sa} * \Phi_N - \Phi_S * \Phi_{Na}}{\Phi_{Sa} - \Phi_{Na}}$$

Where $\Phi_S = \frac{\Delta_t - 47.7}{\Delta_{t_f} - 47.6}$, $\Phi_N = \text{Neutron Density log}$

If $\Phi_N < \Phi_S$ Then: $\Phi_{Sa} = 0.5$, $\Phi_{Na} = -(0.62 * \Phi_N + 0.36) + 10^X$ and

$X = -(1\Phi_N + 0.92)$

If $\Phi_N \geq \Phi_S$ Then: $\Phi_{Sa} = -0.146$, $\Phi_{Na} = 0.5 - 10^X$ and

$X = -(5 * \Phi_N + 0.3)$

4- Bulk Density and Neutron Density Logs Porosity:

Porosity is determined from the Neutron-Density crossplot.

Establishing core porosity versus calculated porosity is difficult as the two datasets have different sampling rates. Furthermore, the core-sampling rate is inconsistent as core plugs are handpicked from the core. In addition, no porosity measurements are available from the Well #1. Figure (24 A & B) shows the calculated porosity using the four methods plotted against core porosity data for wells #2-5. For core position, please refer to Figure (21). Appendix B shows the digitized core description. Overall, core porosity data have higher values compared to calculated porosity. Well #2 has significant higher porosity compared to those calculated. However, core report indicates that the core measurements are unreliable owing to the core plug sizes, more specifically where the diameter of the plugs are greater than the length of the plugs. Since porosity generated from Neutron-Density logs shows the best

fit to core data, the Neutron-Density is used to generate porosity for the complete well interval for all the wells.

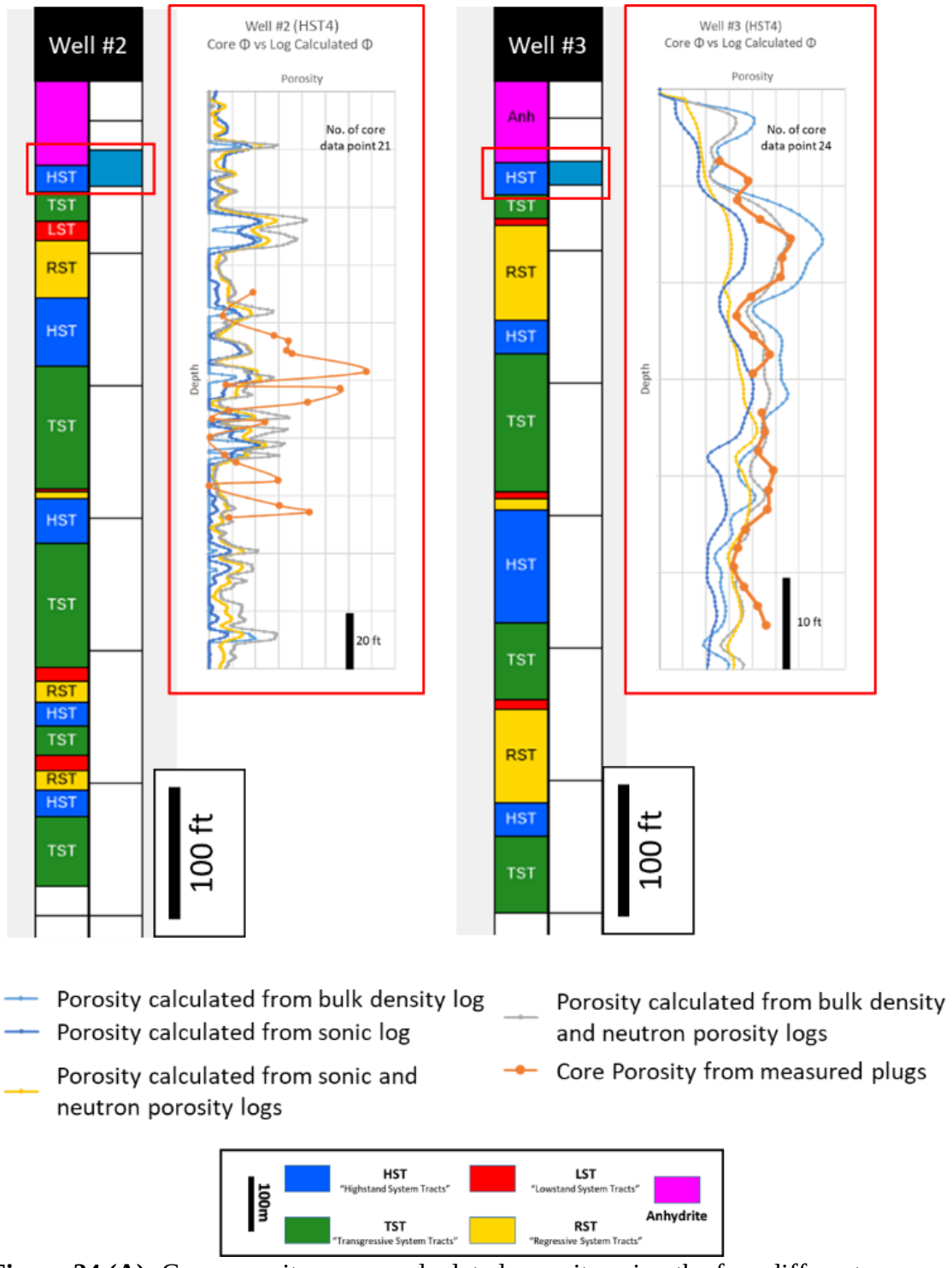

Figure 24 (A): Core porosity versus calculated porosity using the four different methods for Wells #2 & #3. Red box represents the location of the core within the well.

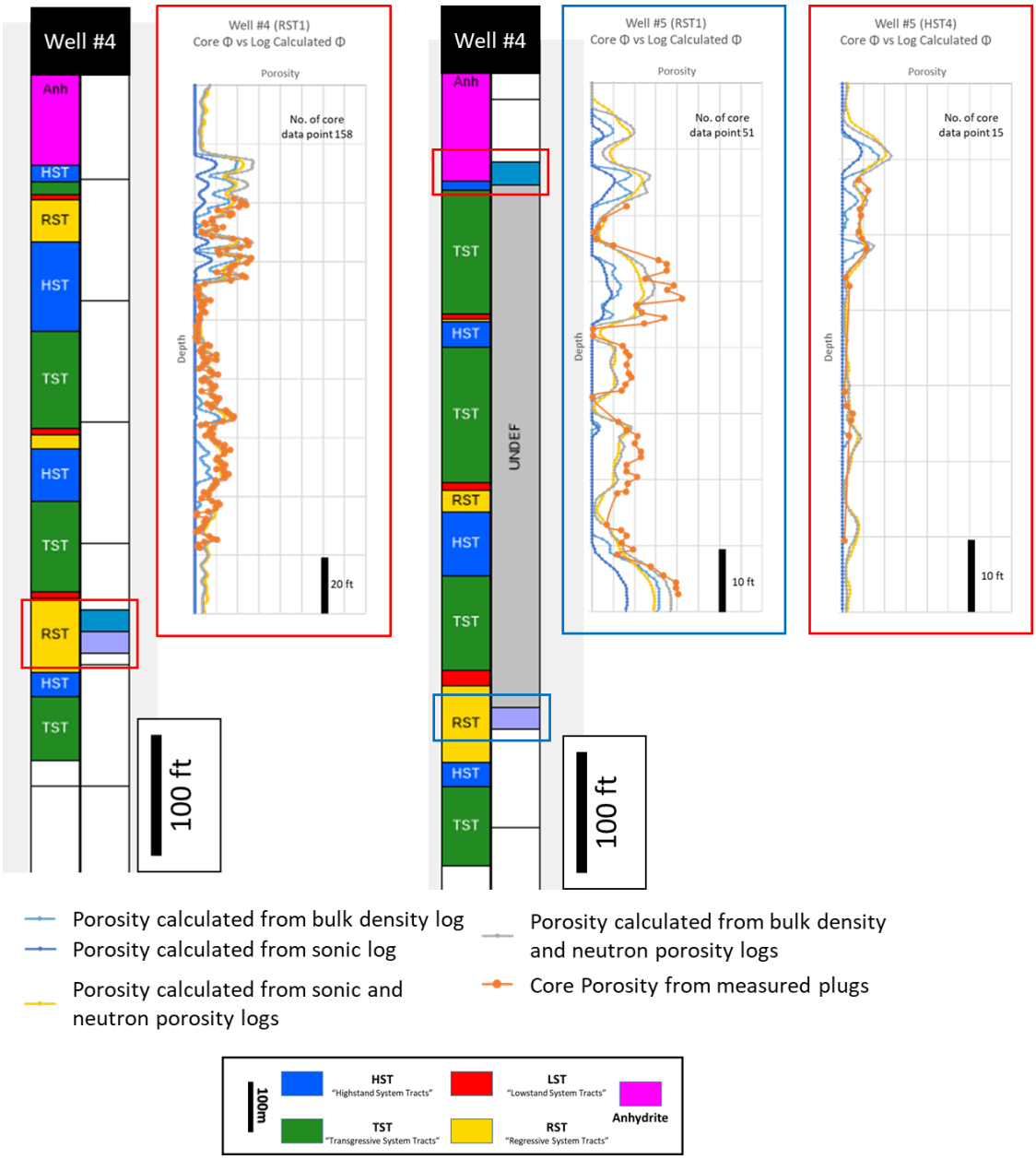

Figure 25 (B): Core porosity versus calculated porosity using the four different methods for Wells #4 & #5. Red and blue boxes represent the location of the cores within the well.

4.2.2 Lithology differentiation

Regional geology indicates that the local depositional environment within the zone and area of interest is restricted to carbonate deposition. Thus, there is no need to perform any analysis to separate between clastics and carbonate. The Neutron-Density crossplot is the main classification tool used to differentiate between lithology, as it has the ability to classify between limestone, dolomite and anhydrite. The importance of differentiation is to predict any diagenesis within the system. Figure (25) shows the crossplot of Neutron-Density for the zone of interest for all of the wells, and highlights the predominance of pure limestone, with some limestone and dolomite mix, but no pure dolomite. Also, there is a lack of thick anhydrite layers within the zone of interest except in Well #5. Figure (26) shows the well #5 logs (GR, Caliber, Density, Neutron, and Sonic) for the anhydrite zone. The density log shows reading up to 2.95-2.98 g/cm^3, indicative of anhydrite. Figure (27) shows the Well #3 logs for the outliers zone.

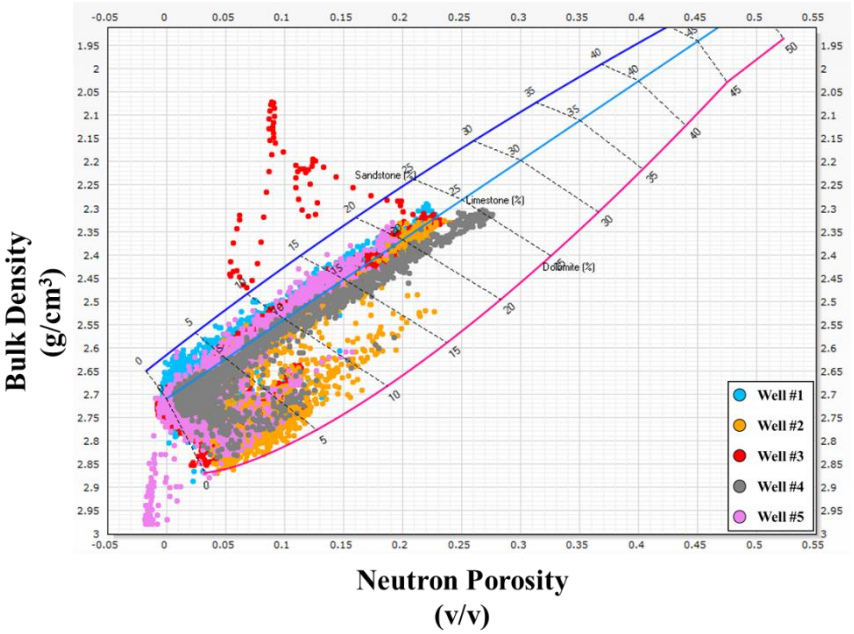

Figure 26: Bulk density versus neutron density cross plot for the zone of interest (cycles #1, #2, #3 and #4) for the five wells. Figures 27 and 28 elaborate more on the outliers.

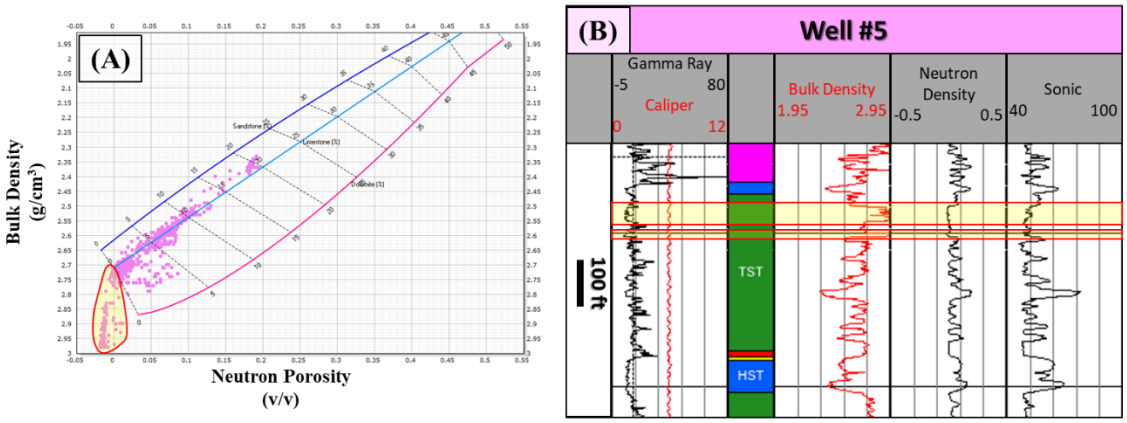

Figure 27: (A) Bulk density versus neutron density cross plot for TST-4 for Well #5. **(B)** Well logs for the same zone to highlight the presence of anhydrite which is causing the outliers in **(A)**. Well logs are GR, caliber, bulk density, neutron density and sonic.

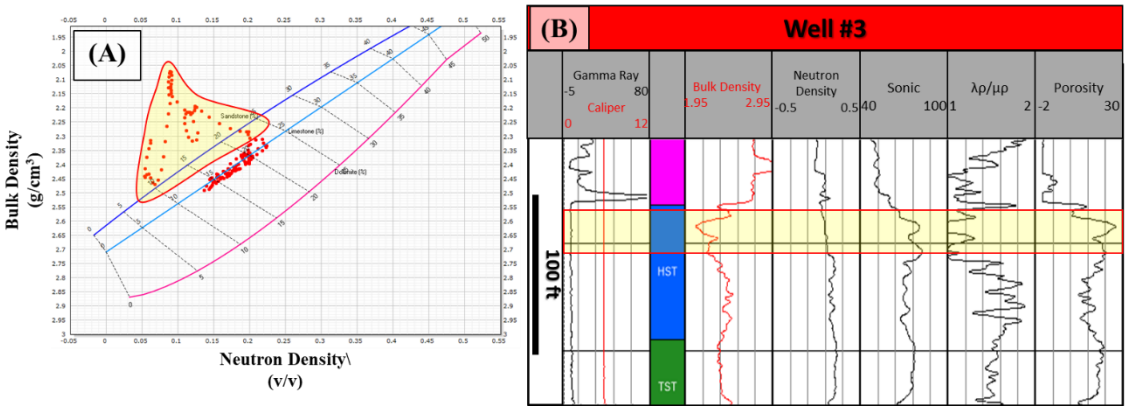

Figure 28: (A) Bulk density versus neutron density cross plot for HST-4 for Well #3. **(B)** Well logs for the same zone to highlight the low density zone which is probably caused by fluid content as shown in the well logs **(A)**. The well logs are GR, caliber, bulk density, neutron density, sonic, λρ/μρ and porosity.

4.2.3 System tracts analysis

Different plots are examined to validate the system tracts that have been interpreted on the well logs via the Galloway approach. Figures (28 -30) show the crossplots for the 2nd cycle (Figure 31) for four wells (#1, #3, #4, and #5) as a quality

control. The crossplots are GR versus acoustic impedance, bulk density versus neutron porosity and acoustic impedance versus porosity. The 2nd cycle is chosen as it proved the most well-defined cycle across the five wells. The crossplots show consistent interpreted systems tracts for the four wells. In addition, a clear discrimination for HST from the other systems tracts is clearly evidenced.

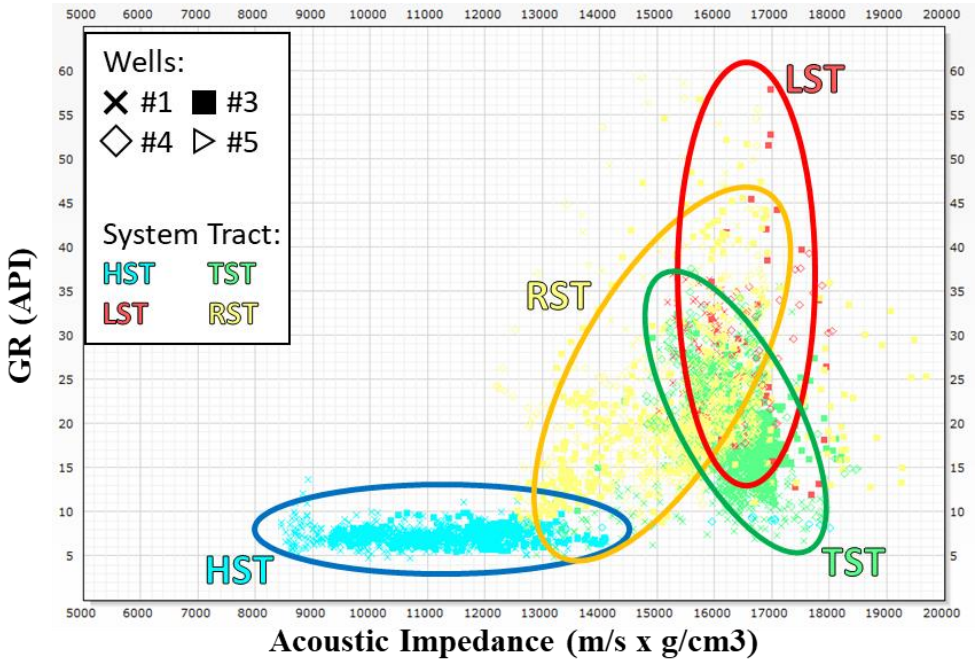

Figure 29: GR versus acoustic impedance cross plot for cycle #2 for the four wells (#1, #3, #4 & #5). HST zone has a very distinctive zonation compared to the other zones. It is difficult to distinguish among LST, RST and TST. However, they have different trends.

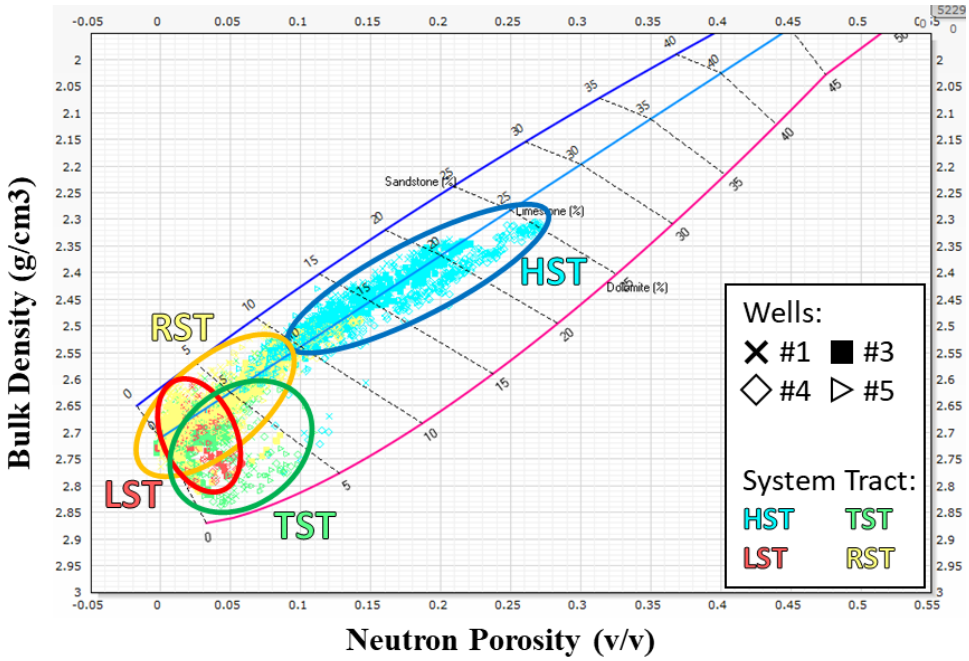

Figure 30: Bulk density versus neutron density cross plot for cycle #2 for the four wells (#1, #3, #4 & #5). HST zone has a very distinctive zonation compared to the other zones due to its high porosity. It is difficult to distinguish among LST, RST and TST. TST has more dolomite percentage compare to RST.

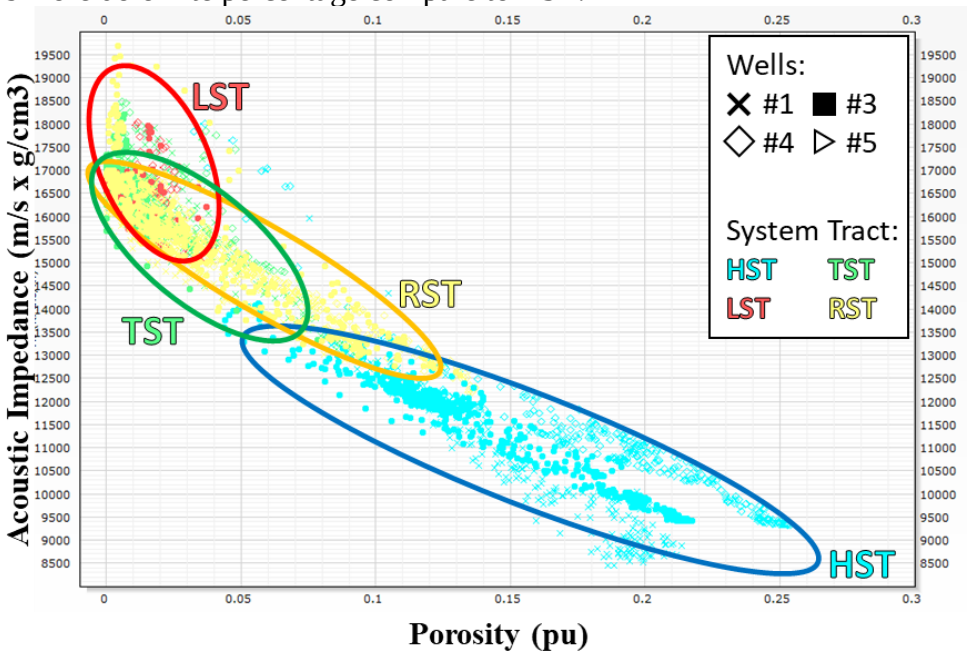

Figure 31: Acoustic impedance versus porosity cross plot for cycle #2 for the four wells (#1, #3, #4 & #5). HST zone has a very distinctive zonation compared to the other

zones due to its high porosity. RST has higher porosity compared to the TST. LST has the lowest porosity.

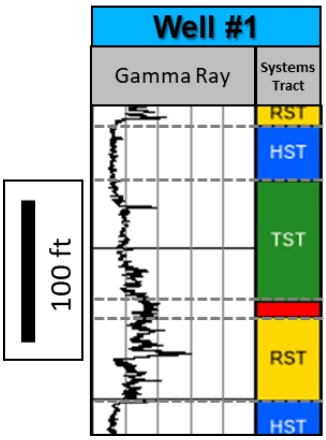

Figure 32: GR log and the interpreted system tracts for cycle #2 from Well #1.

Figures (32-35) show bulk density versus neutron density for each system tracts (HSTs, TSTs, RSTs and LSTs) for the five wells.

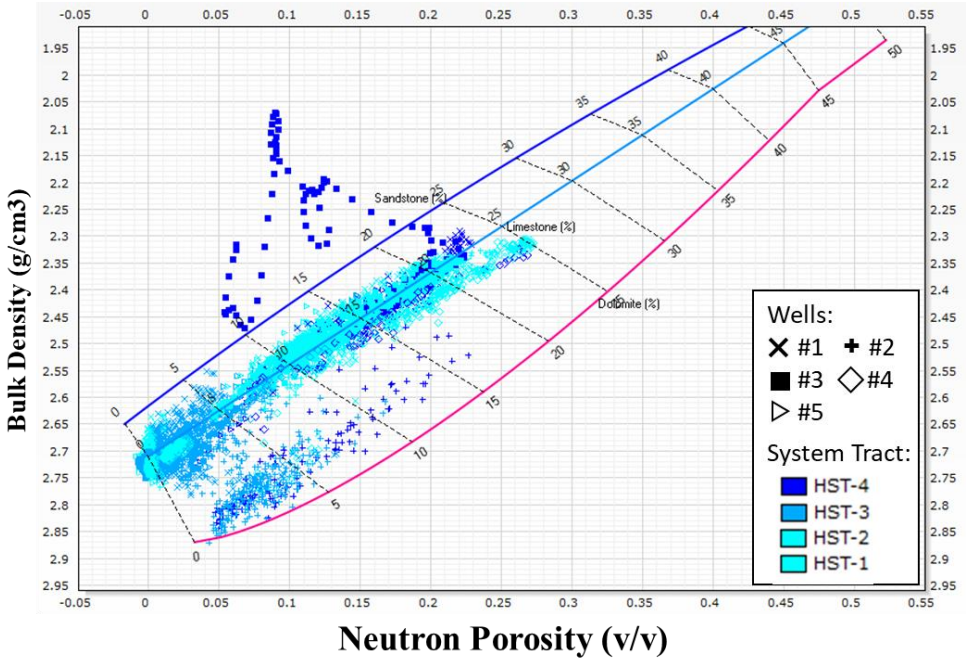

Figure 33: Bulk density versus neutron density cross plot for all HSTs for the five wells. HST-2 and HST-4 show high porosity development with high calcite percentage. HST-1 and HST-3 have lower porosities and show high degrees of associated dolomitization.

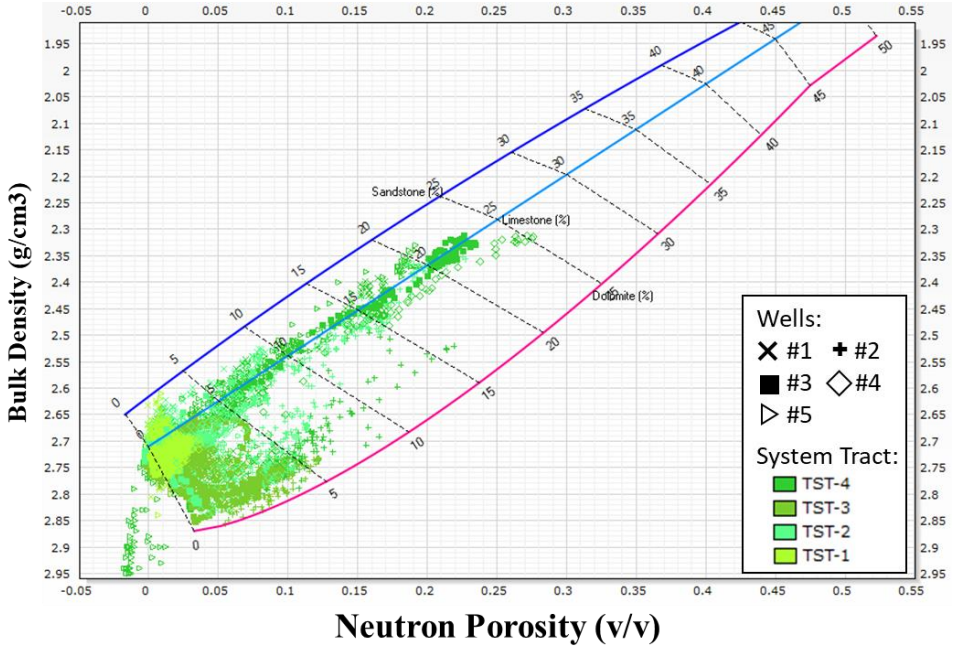

Figure 34: Bulk density versus neutron density cross plot for all TSTs for the five wells. TST-4 has the highest porosity development. Most of the TSTs have porosity values <5%.

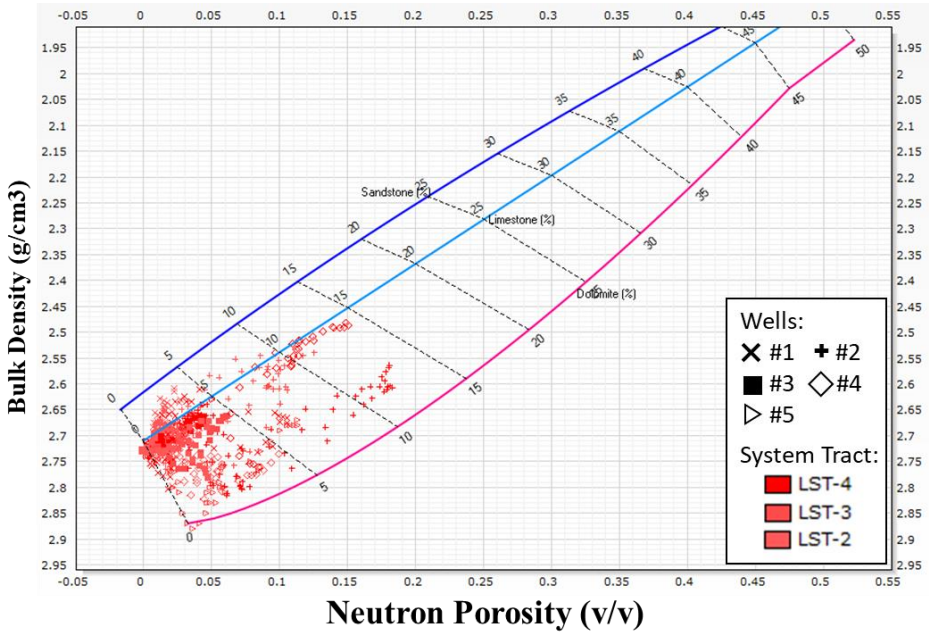

Figure 35: Bulk density versus neutron density cross plot for all LSTs for the five wells. LSTs are dominated by mudstone which explains the very low porosity overall and low dolomitization.

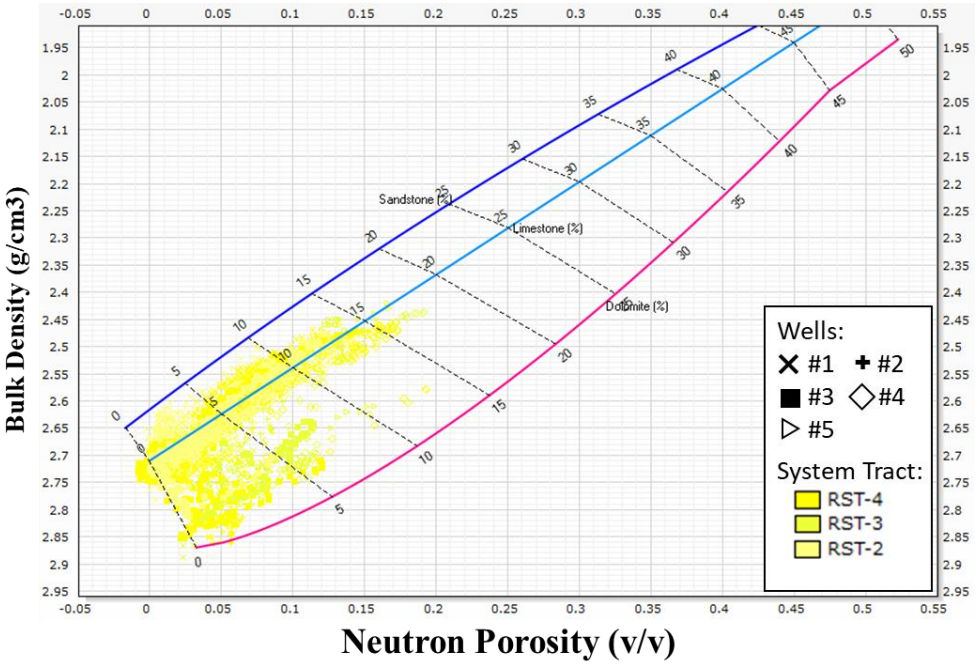

Figure 36: Bulk density versus neutron density cross plot for all RSTs for the five wells. RSTs are very heterogeneous as they are formed by mudstone and reworked sediments which might have high porosity.

It is important to establish a relationship between these hitherto unrelated parameters based on the crossplots. For example, plotting calculated porosity against neutron-density or bulk density will show a false correlation as the calculated porosity is derived from both logs. However, any relation established from plotting the measured porosity from core data with either bulk density or neutron-density will prove scientifically meaningful.

4.2.4 Secondary porosity

Understanding and classifying the porosity types in carbonate facies is important as it allows for insights to diagenetic alteration. Furthermore, presence of primary

porosity is importance for lateral continuity and homogeneity within the reservoir. Primary porosity types in carbonates are interparticle and intercrystalline, while moldic and vuggy porosity represent secondary porosity types. Since sonic porosity is insensitive to moldic, vuggy and fractures, it can be used to calculate primary porosity (Wilson, 1997; Milad and Slatt, 2018). Thus, difference between neutron-density porosity (also known as total porosity) and sonic porosity may be understood to represent the secondary porosity. To determine the effect of the secondary porosity, neutron-density crossplot is used because the intersection shows the total porosity. Then, points are color coded by the secondary porosity. Figures (36 - 37) shows the crossplots for all the cycles and classified based on the wells. Wells #1, #2, and #3 show minimum effects of diagenesis on the porosity, as the porosity is predominately primary in nature. In contrast, Wells #4 and #5 show more signs of diagenesis as they have higher secondary porosity up to 12%. Figure (39) shows the bulk density versus neutron density for all the wells and all the cycles color coded by the total porosity.

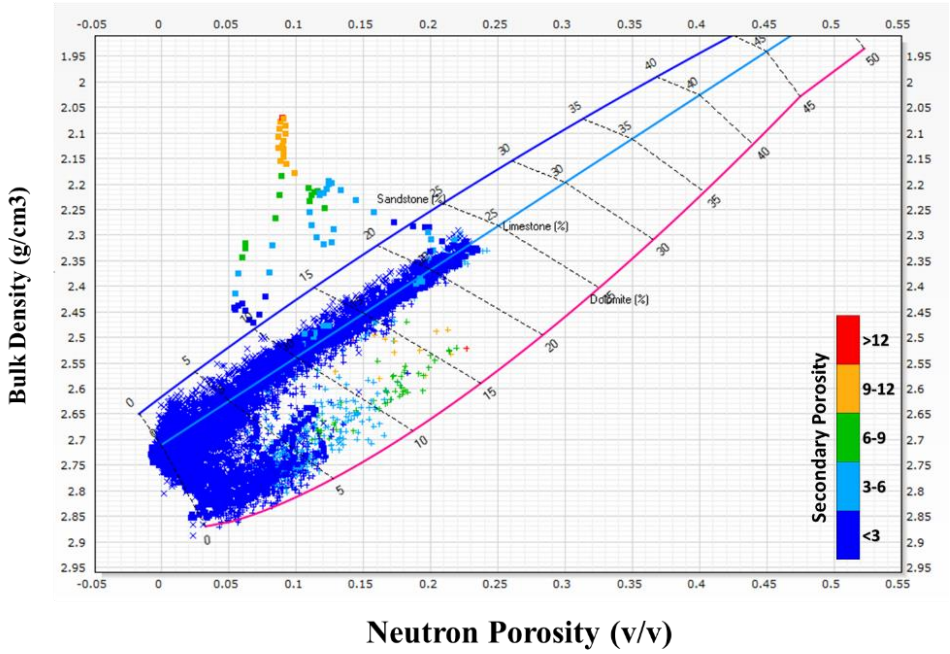

Figure 37: Bulk density versus neutron density cross plot for all cycles for three wells (#1, #2 and #3) and color coded by secondary porosity. Porosity within these three wells is dominated by the primary porosity.

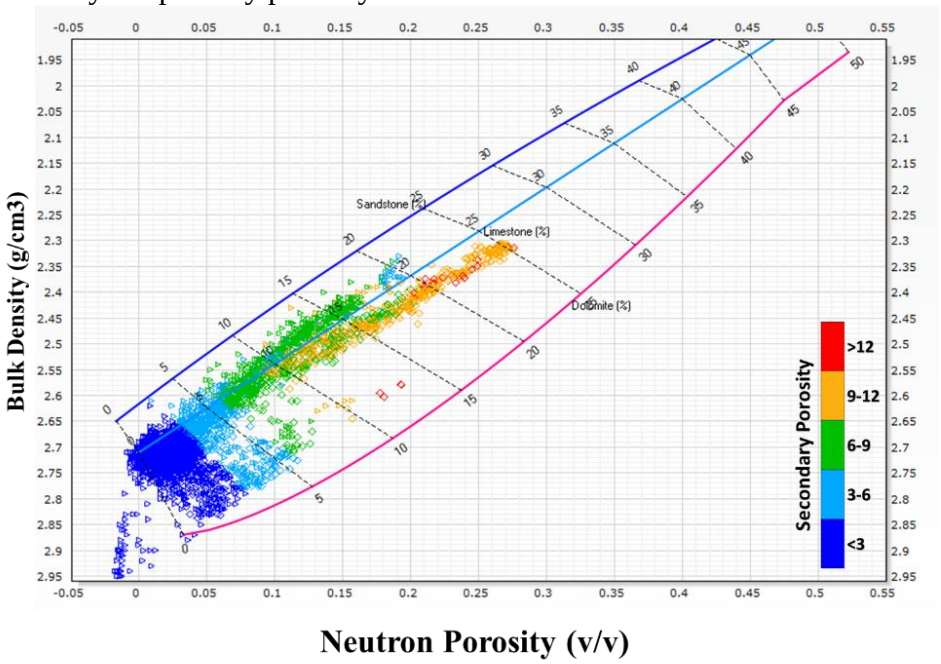

Figure 38: Bulk density versus neutron density cross plot for all cycles for two wells (#4, and #5) and color coded by secondary porosity. These two wells have higher secondary porosity compare to Wells #1, #2 and #3.

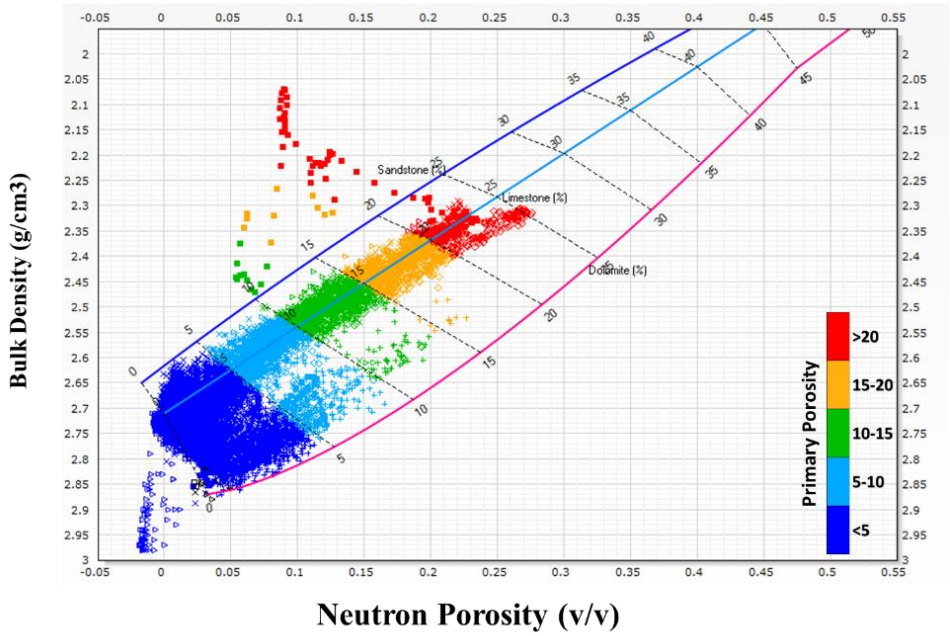

Figure 39: Bulk density versus neutron density cross plot for all cycles for the five wells and color coded by total porosity.

4.3 Seismic Quantitative Interpretation

4.3.1 Post-stack acoustic impedance inversion

Post-stack Acoustic Impedance Inversion (PSAII) is basically converting seismic reflection data to P-impedance ($\rho * \upsilon_p$). This transformation allows one to predict reservoir qualities such as porosity and lithology. Porosity may be predicted using only P-impedance inversion, while lithology detection requires both P and S impedances inversions in combination in order to remove any ambiguities arising from fluid effects (Russell et al., 2006). Due to lack of shear data, S-impedance inversion was not included in this study. Consequently, no lithology study was conducted using the seismic data.

The Russell et al. (2006) post-stack acoustic impedance inversion method is applied to the seismic data to generate the results. This method is also known as model based inversion. Figure (39) shows the inputs to generate the inversion volume.

To generate the PSAII, there are two main inputs used. First, borehole data (sonic and density logs) are used to generate the acoustic impedance log. Second, derivative data from the seismic reflection volume are incorporated , which includes extracted wavelet and interpreted horizons. The target of PSAII is to enhance the frequencies that are extracted from the seismic data, especially the lower frequencies which are lost during processing (Russell et al., 2006). Since seismic data has a restricted frequencies band-width, borehole data are used to provide the missing frequencies through the acoustic impedance logs. An initial inversion model is created using seismic horizons as guidance while content is extracted from the acoustic

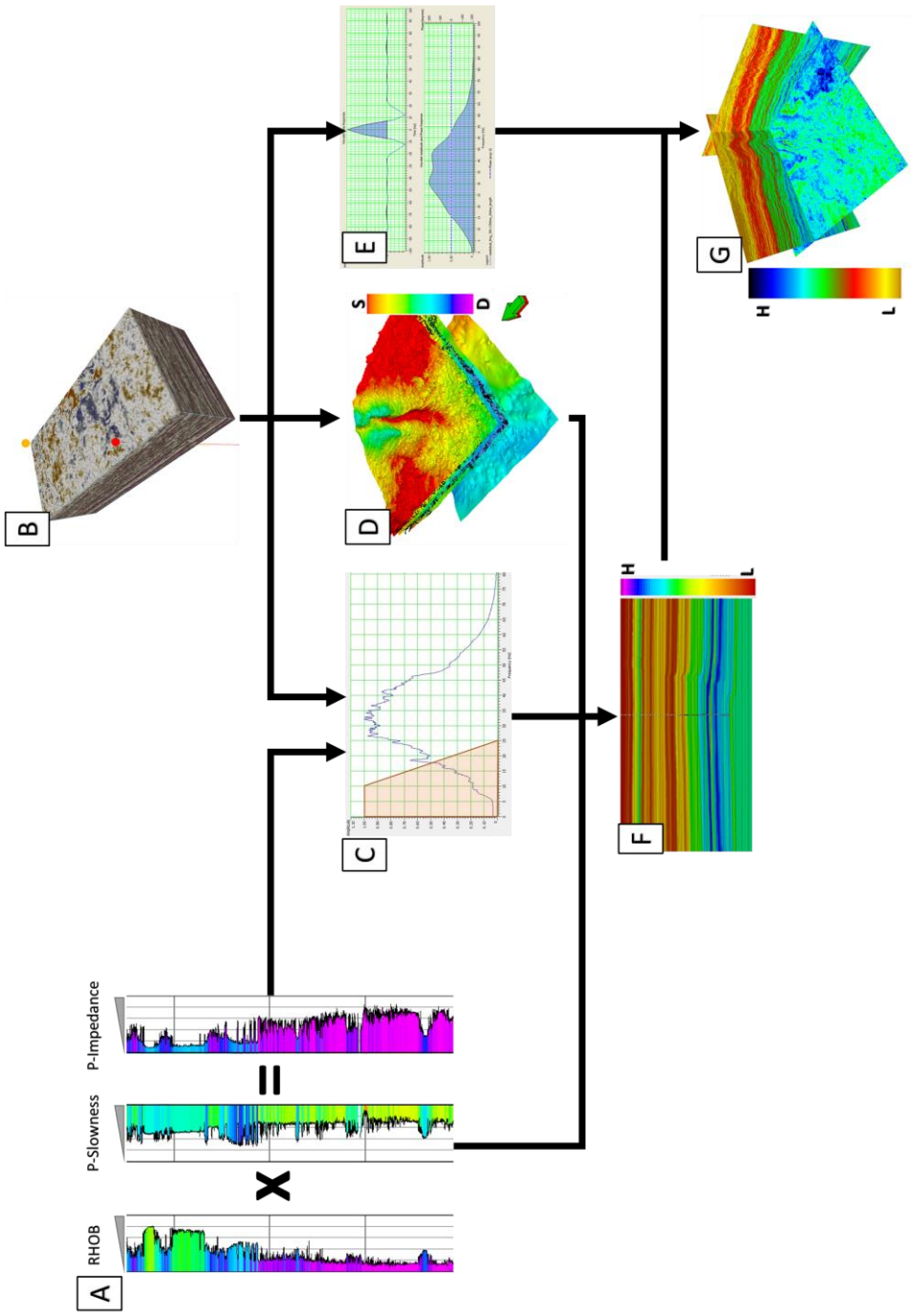

Figure 40: Workflow followed to generate the post stack acoustic impedance, Zp. (A) input wells logs (bulk density and P-slowness (P-sonic)) are used to generate the acoustic impedance log. (B) 3D seismic survey. (C) Curve represents frequency bandwidth extracted from the seismic survey, while the shaded area represents the low cut filter. Low frequencies are extracted from impedance logs. (D) Interpreted horizons. (E) Extracted wavelet. (F) Initial (low frequency) model. (G) The output PSAII volume.

impedance logs using a low-pass filter (10-25 Hz). Different low-pass filter settings were test, but little apparent differences were observed. Four wells are used to generate the initial impedance inversion model which are #1, #2, #3 and #4. Well #5 created artifacts to the model as its well logs are considered to be raw data without any treatments or conditionings. However, eliminating this well out of the initial model will allow its use in blind testing. Eight horizons were used as inputs to guide the initial model. Figure (40) shows an inline of the initial model that goes through Well #3. Figure (22) shows the statistically extracted wavelet from seismic, which is the same wavelet that is used for the seismic-well tie. Seismic traces are inverted using this wavelet to provide the middle frequency broadband of the data while the initial model provides the low frequency content of the PSAII.

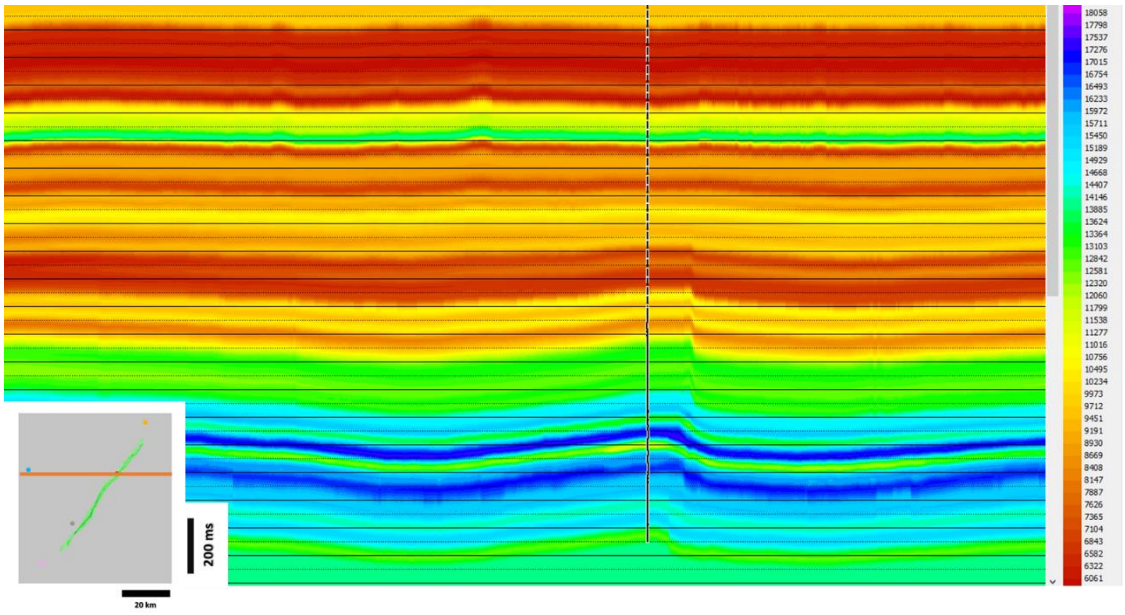

Figure 41: The initial low frequency model based on the impedance logs from four wells (#1, #2, #3, and #4) and guided by the interpreted horizons.

Before applying the initial model and the wavelet on the seismic volume, it is important to analyze and compare the inverted logs versus original logs for all wells (Figure 41). The correlation is good (90.1%) for all the wells while the synthetic trace shows 99.6% correlation with the seismic (Figure 42).

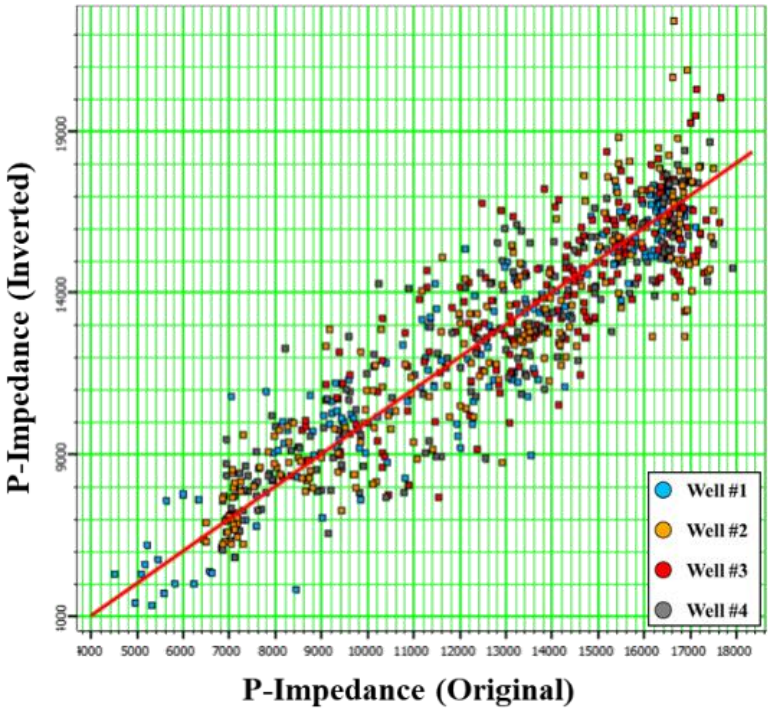

Figure 42: Inverted P-Impedance versus Original P-Impedance analysis for the four wells (#1, #2, #3 and #4).

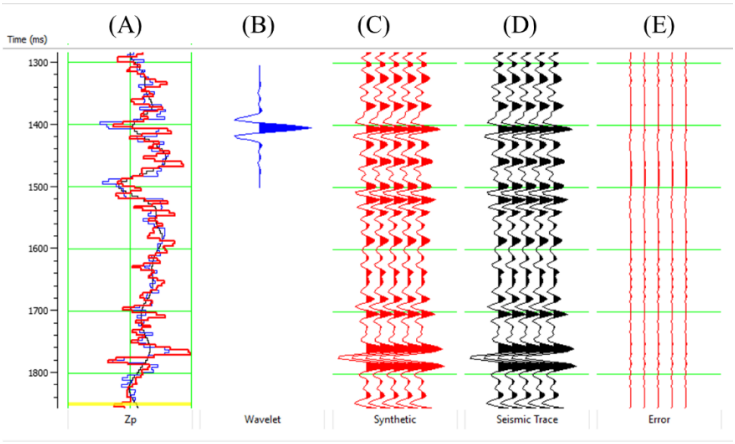

Figure 43: (A) Original P-Impedance log (blue) and Inverted P-Impedance log (red), **(B**) extracted wavelet from the seismic survey, **(C)** synthetic seismic trace, **(D)** extracted trace from the seismic (Inline# 3790 and Xline# 6044), and (**E)** error trace. The correlation between the extracted trace from the seismic survey and the synthetic trace is 90.1%.

Several PSAII volumes were produced using differing numbers of wells to examine the variations within the results. Minimal differences were found between the results using either three or four wells. The main purpose of this experiment is to enhance the confidence of the final result. Refer to Appendix A for a comparison between the inversion results using one, two, three or four wells. Seismic inversions mainly along strike shows minor differences in the zone of interest and significant differences in the carbonate facies above and below.

4.3.2 3D porosity prediction

Figure (30) shows a clear relationship between acoustic impedance and porosity. Therefore, PSAII volume will be used to predict porosity for these Jurassic carbonates.

Acoustic impedance inversion does not contain information regarding porosity though it does provide insights into lithology and fluid content. There are different approaches to drive any relationship that are linear, nonlinear and neural network (Hampson et al., 2001). In this study, all three approaches are tested in order to establish the relationship. A Probabilistic Neural Network (PNN), a type of neural network, has the best correlation for the predicting porosity when compared to the other two methods. Neural networks may consist of numerous layers. As one targets only one output, only one hidden layer will exist which means the neural network consists of three layers (Figure 43).

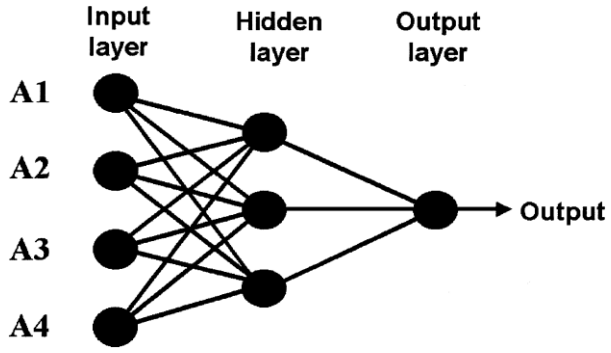

Figure 44: Multilayer feedforward neural network. From Hampson et al.(2001).

Seven attributes are used in the input layer that are PSAII, instantaneous quality, instantaneous frequency, instantaneous amplitude, integrate, derivative and dominant frequency. The efficacy of these attributes to detect seismic facies is well-documented, as they remain sensitive to layer properties such as porosity, and lithology changes (Pigott et al., 2013). While in general increasing the number of attributes can increase the fit of the data to the training. However, adding more attributes can lead to overtraining the data which may result in a decreasing fit (Figure 44). Figure (45) shows

the crossplot of actual porosity versus predicted porosity via PNN with cross correlation of 79%. For more details regarding neural network application please refer to (Hampson et al., 2001). Figures (46-51) shows sections of the conditioned seismic, PSAII and porosity predicted via PNN. The first section is XLine through Well #3 while the second section is InLine through Well #4 which was not included in the porosity prediction via PNN. More of the interpretation on the predicted porosity will follow up in the next chapter.

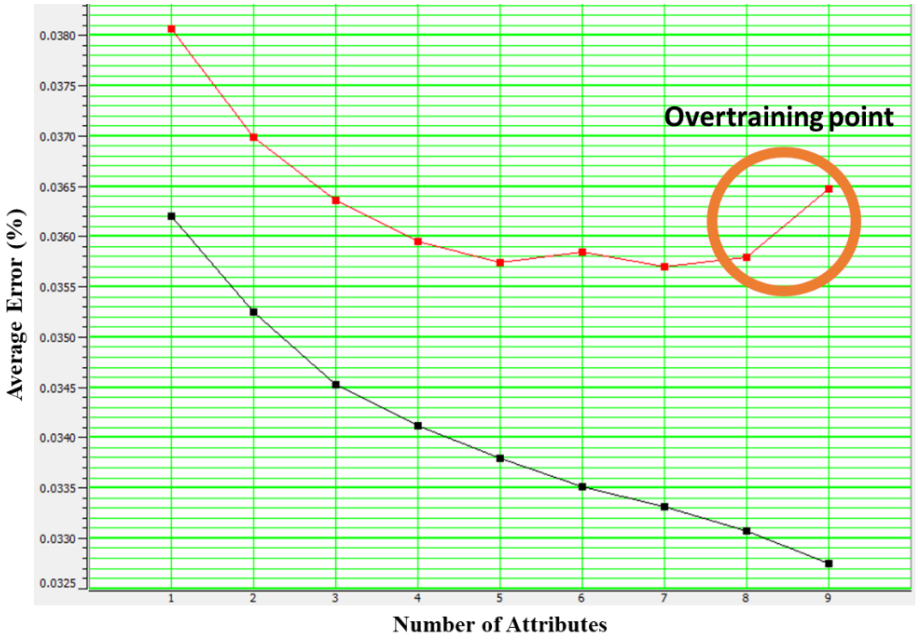

Figure 45: The average error for used four wells (#1, #2, #3 and #4) versus number of attributes. Black line represents all wells error. Red line represents the validation error. The orange circle shows the overtraining effects on the error.

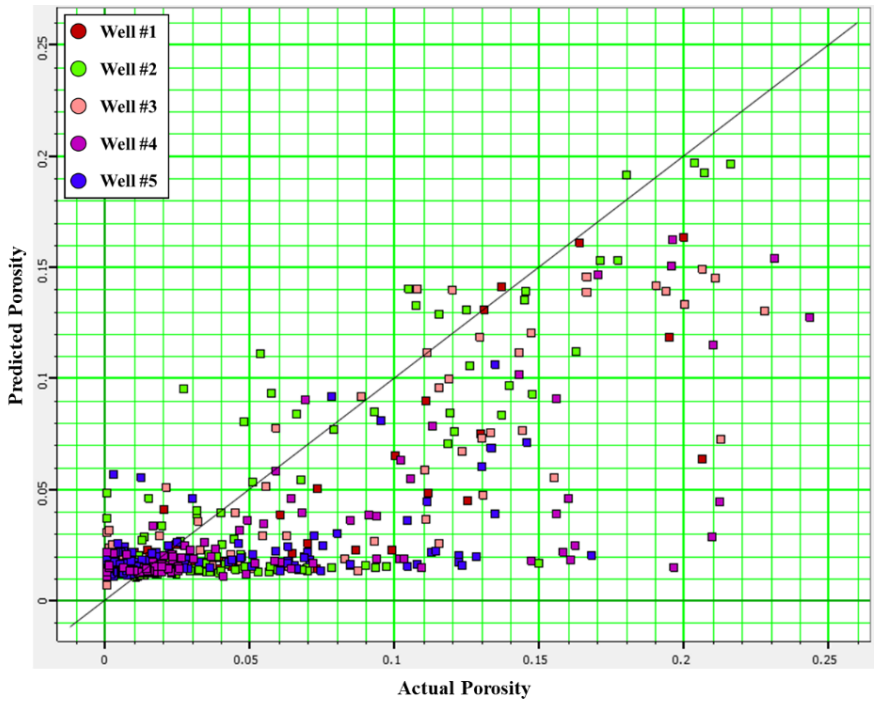

Figure 46: Predicted porosity via neural network versus actual porosity from well logs for the five wells. Cross-correlation is 79.3% with error= 3%. Overall, predicted porosity is lower than the actual porosity. Seven attributes are used in the training phase.

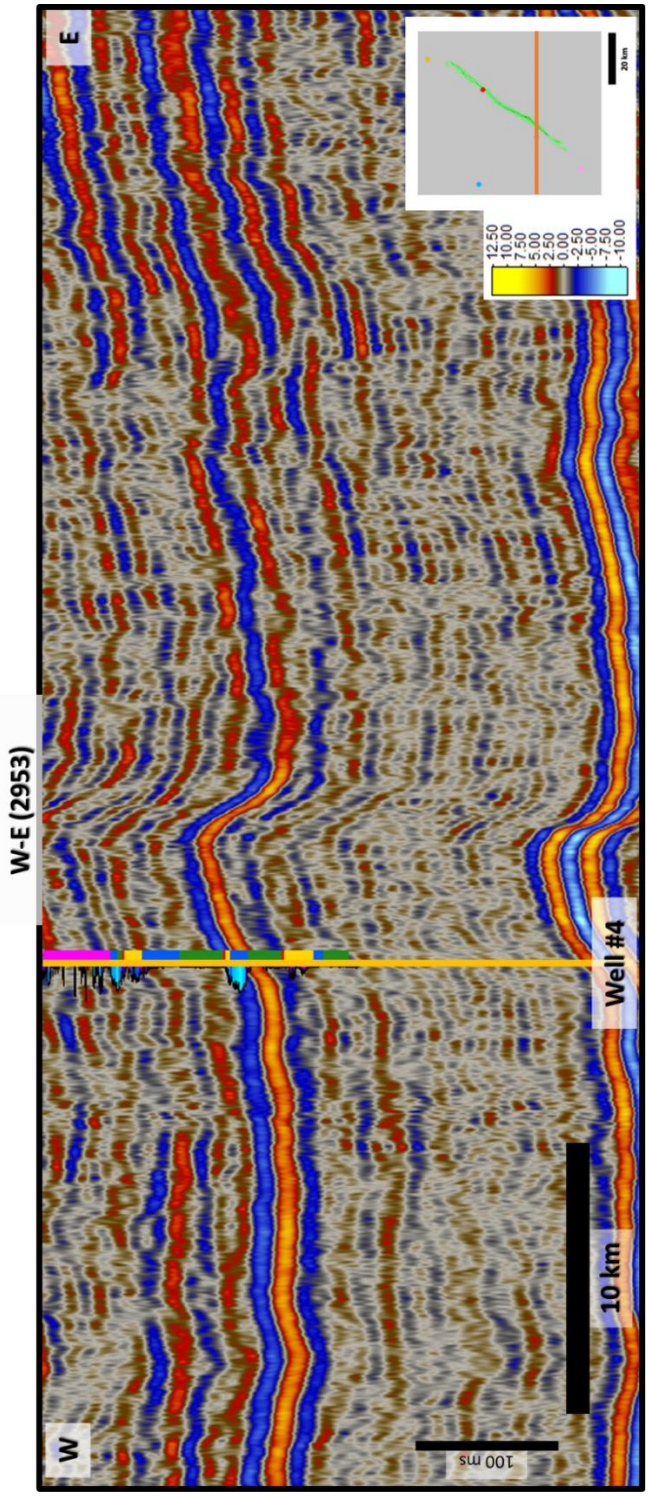

Figure 47: Uninterpreted E-W seismic section Inline #2953 as shown in the index map on the bottom right corner. The orange vertical line indicates the location of Well #4.

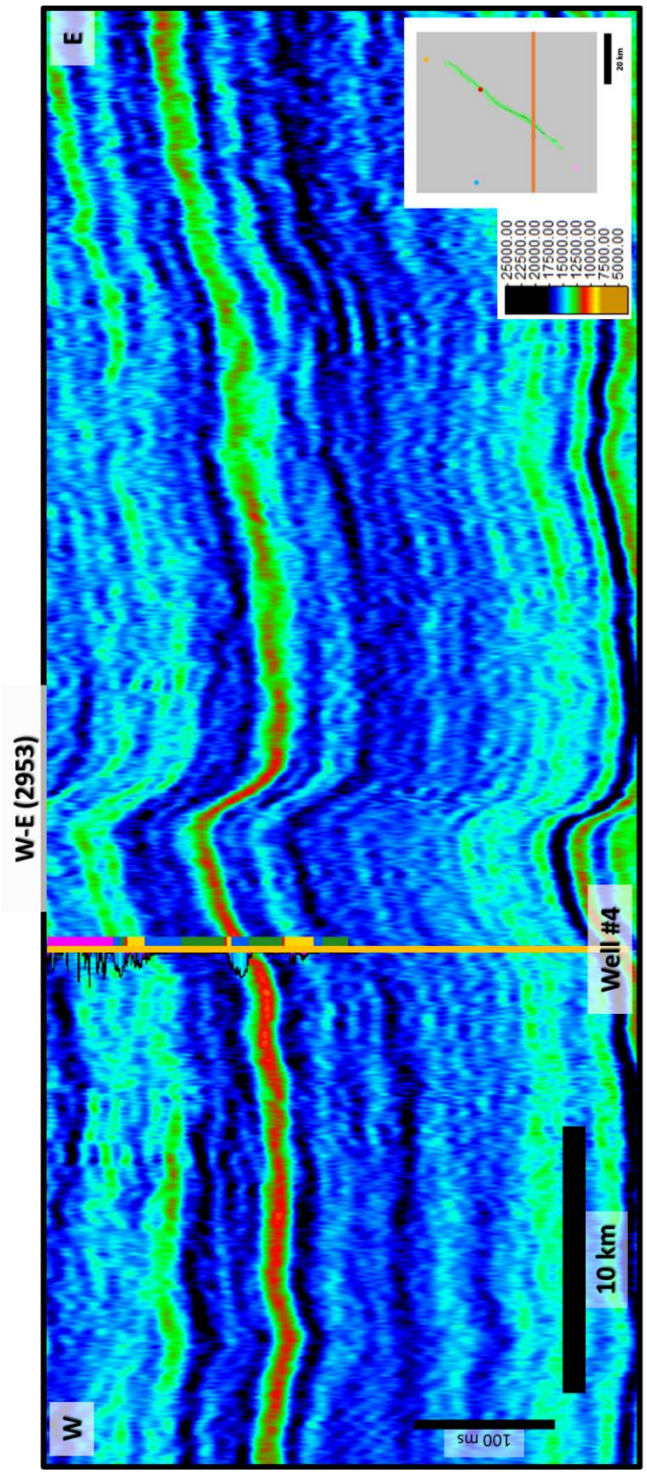

Figure 48: Uninterpreted E-W PSAII for the Inline #2953 as shown in the index map on the bottom right corner. The orange vertical line indicates the location of Well #4.

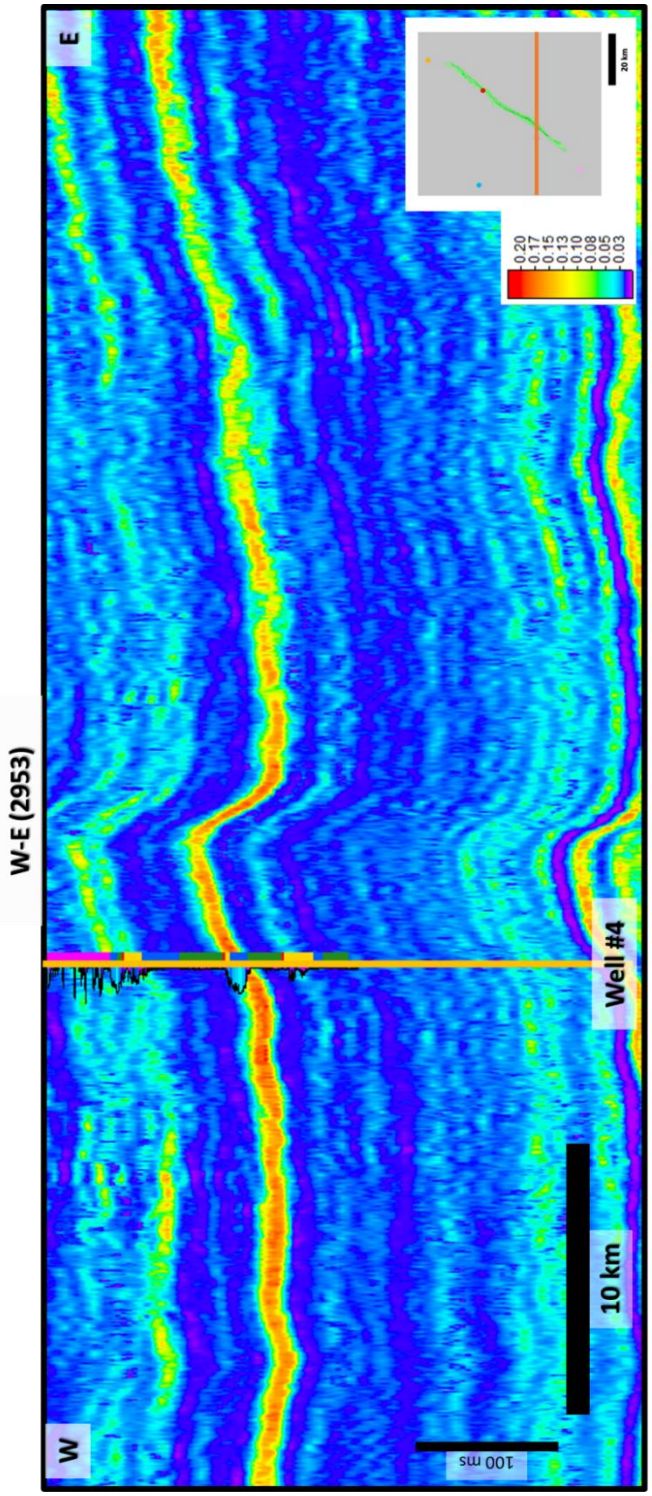

Figure 49: Uninterpreted E-W predicted porosity via PNN for the Inline #2953 as shown in the index map on the bottom right corner. The orange vertical line indicates the location of Well #4.

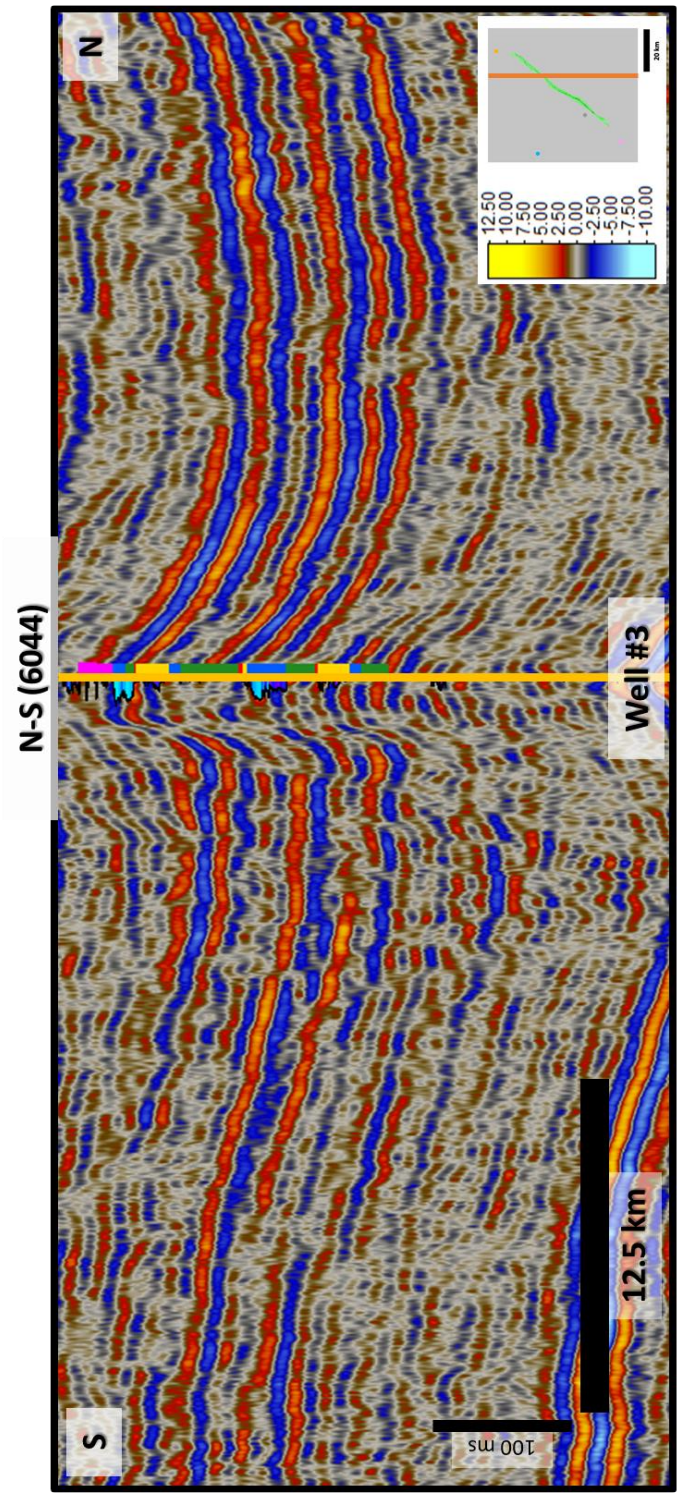

Figure 50: Uninterpreted N-S seismic section Xline #6044 as shown in the index map on the bottom right corner. The orange vertical line indicates the location of Well #3.

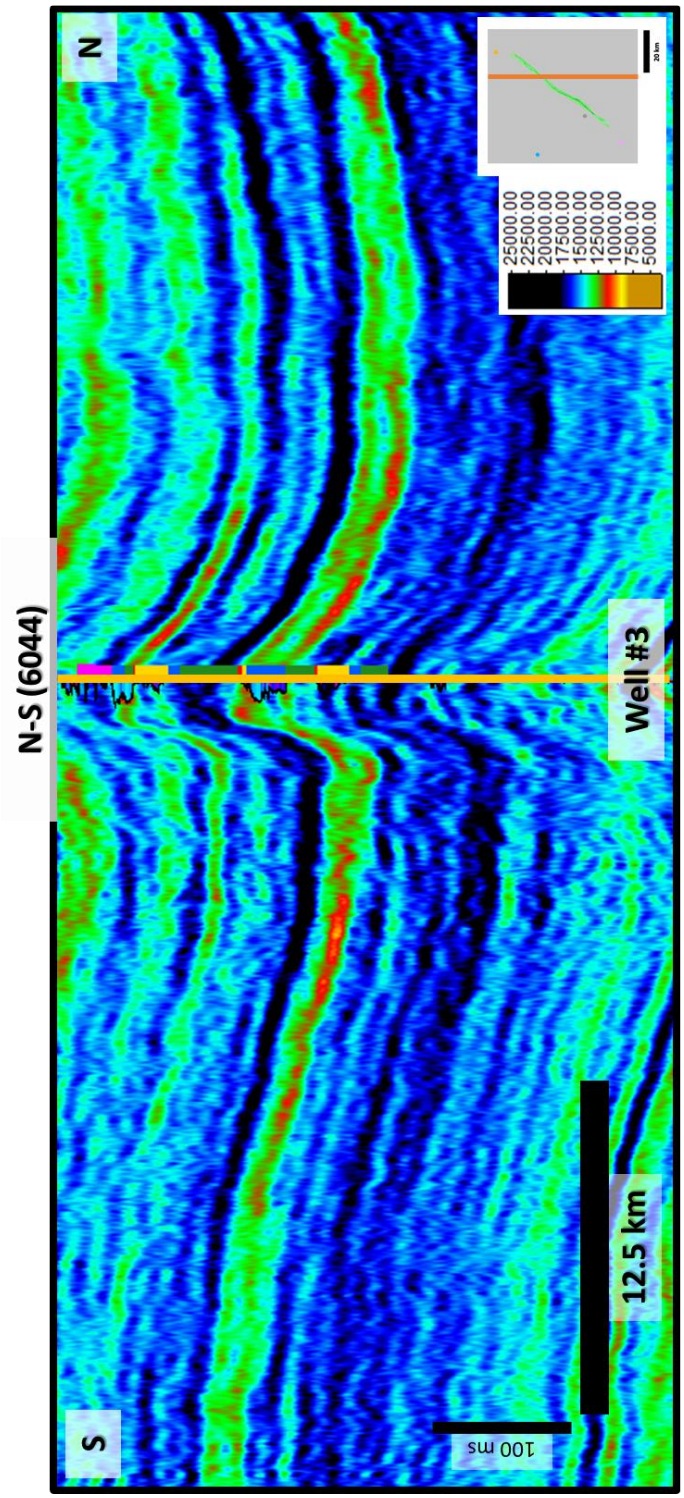

Figure 51: Uninterpreted N-S PSAII for the Xline #6044 as shown in the index map on the bottom right corner. The orange vertical line indicates the location of Well #3.

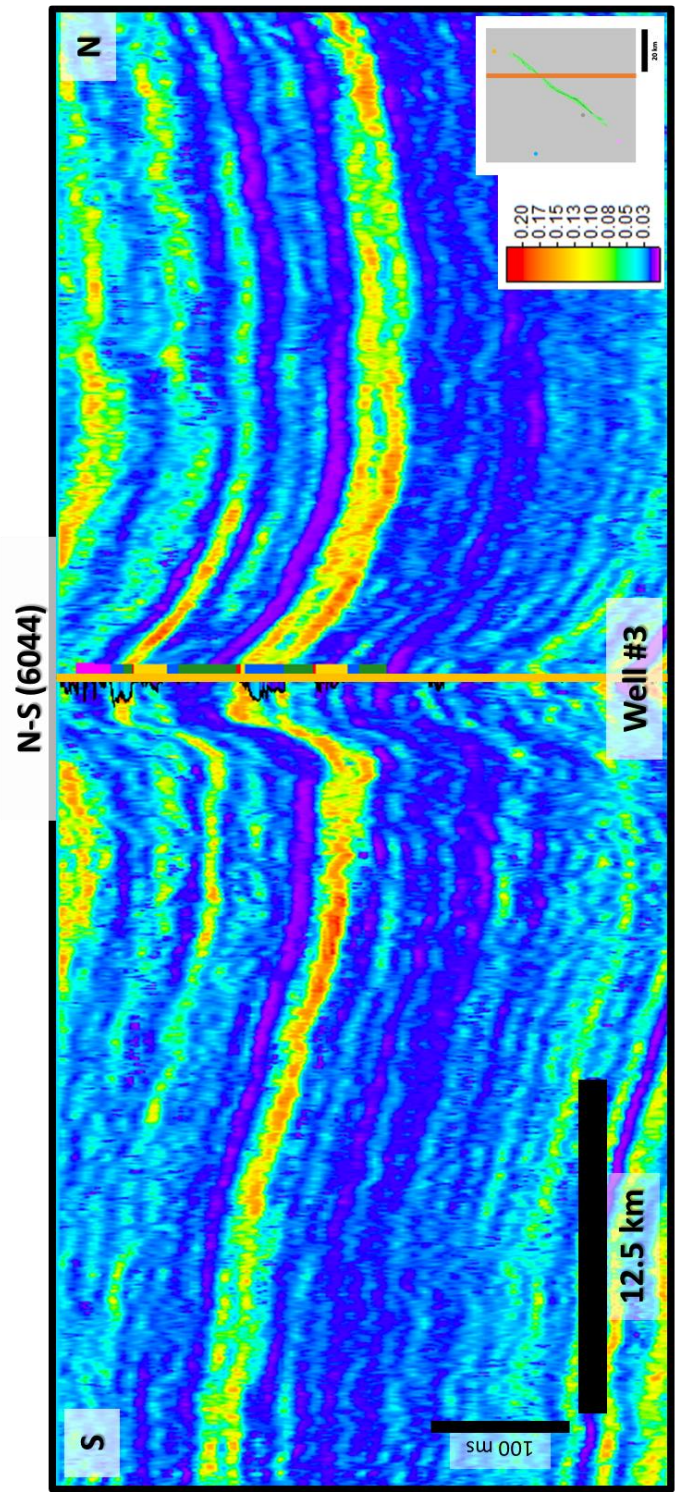

Figure 52: Uninterpreted N-S predicted porosity via PNN for the Xline #6044 as shown in the index map on the bottom right corner. The orange vertical line indicates the location of Well #3.

Chapter 5 Interpretations and Discussions

5.1 Controlling Factors

There are several depositional models to describe the different carbonate depositional environments. The three main depositional environment models most widely recognized are rimmed platform, unrimmed platform, and ramp. Wilson (1975) established idealized facies belts of a rimmed carbonate platform (Figure 52). The zone of interest of this study correlates to facies #6 (winnowed edge sands) in the model, deposited during an overall time of rising sea levels to HST. Grainstone and packstone are the dominant lithologies deposited. In contrast, during an approaching LST, sea level is dropping, the interpreted facies is that of #8 (restricted circulation). Though Ziegler (2001) has presented the occure of several thick subaerial anhydrite packages during the Jurassic in his regional study, these packages have not been found in this area which suggest a slightly deeper depositional environment during the study period.

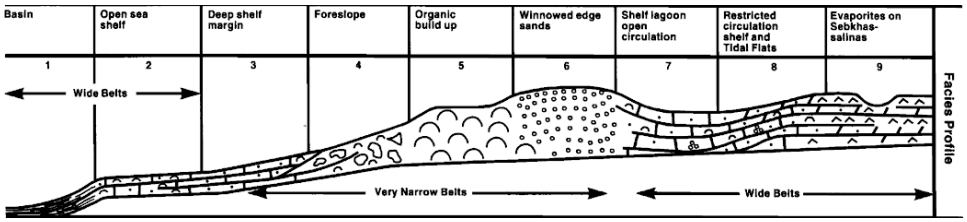

Figure 53: Wilson's (1997) model for rimmed carbonate platform showing idealized facies belt. Area of interest is interpreted to be deposited between facies #6 and #8. HSTs are interpreted as winnowed edge sands (facies #6), while LSTs are interpreted as restricted circulation shelf and tidal flats (facies #8) From Wilson (1997).

The importance of determining the lithologic facies is to understand and predict the reservoir properties across the area of study. A key factor in determining the lithology, aside from sequences interpretation and core data, is paleolatitude and plate direction during the Jurassic era (Figure 53). Moreover, inherited topography can have direct impacts on the reservoir properties due to its control on carbonate production and subsequent exposure during sea level falls. Though proposing differing causes, Mackenzie and Pigott (1981); Sandberg (1983); Stanley and Hardie (1999) theorized that the Jurassic period was dominated by low Mg/Ca generation, resulting in low Mg/Ca ratio's was a time of "greenhouse". Deposited carbonates during this stage of low Mg/Ca make them more resistant to diagenesis compared to high Mg/Ca ratio sediments.

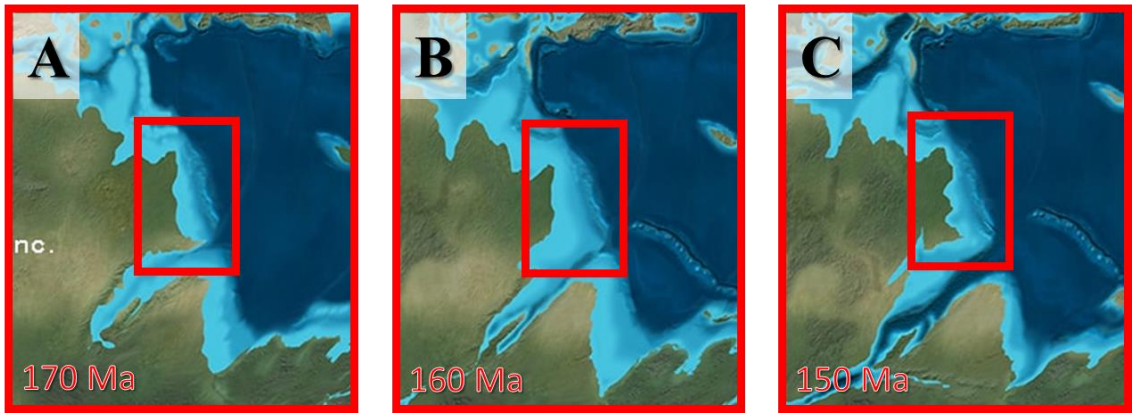

Figure 54: (A) The global paleogeography and tectonics during the Bathonian (≈170 Ma). **(B)** The global paleogeography and tectonics during the Oxfordian (≈160 Ma). **(C)** The global paleogeography and tectonics during the Tithonian (≈150 Ma). The highlighted red box shows the location of the Arabian Plate during these periods. The paleogeography confirms the carbonate settings. From http://deeptimemaps.com.

5.2 Interpreted Parasequence Sets

Using the interpreted parasequence sets, we can predict and link the petroleum elements to the parasequences TST's, HST's, RST's, and LST's. Using a sequence stratigraphic framework, the presence of the three main elements of petroleum systems (i.e. seal, reservoir, source) may be inferred.

5.2.1 Highstand System Tracts (HSTs)

HSTs are deposited during high sea level. The abundance of water circulation enhances the carbonate factory leading to growth of the carbonates. Specifically, in this area of interest, the high process energy leads to the growth of the ooids leading to grainstone/packstone deposition. This has been confirmed by the thin sections extracted from the cores from the Well #1 (Figure 54). Moreover, HST lithology facies make great reservoirs, as they tend to have high interparticle porosity. They also have fairly low diagenetic alteration as indicated by the neutron-density crossplot, making them more lateral connected. However, the HST's are more prone to erosion from the subsequent RST period due to sea level fall.

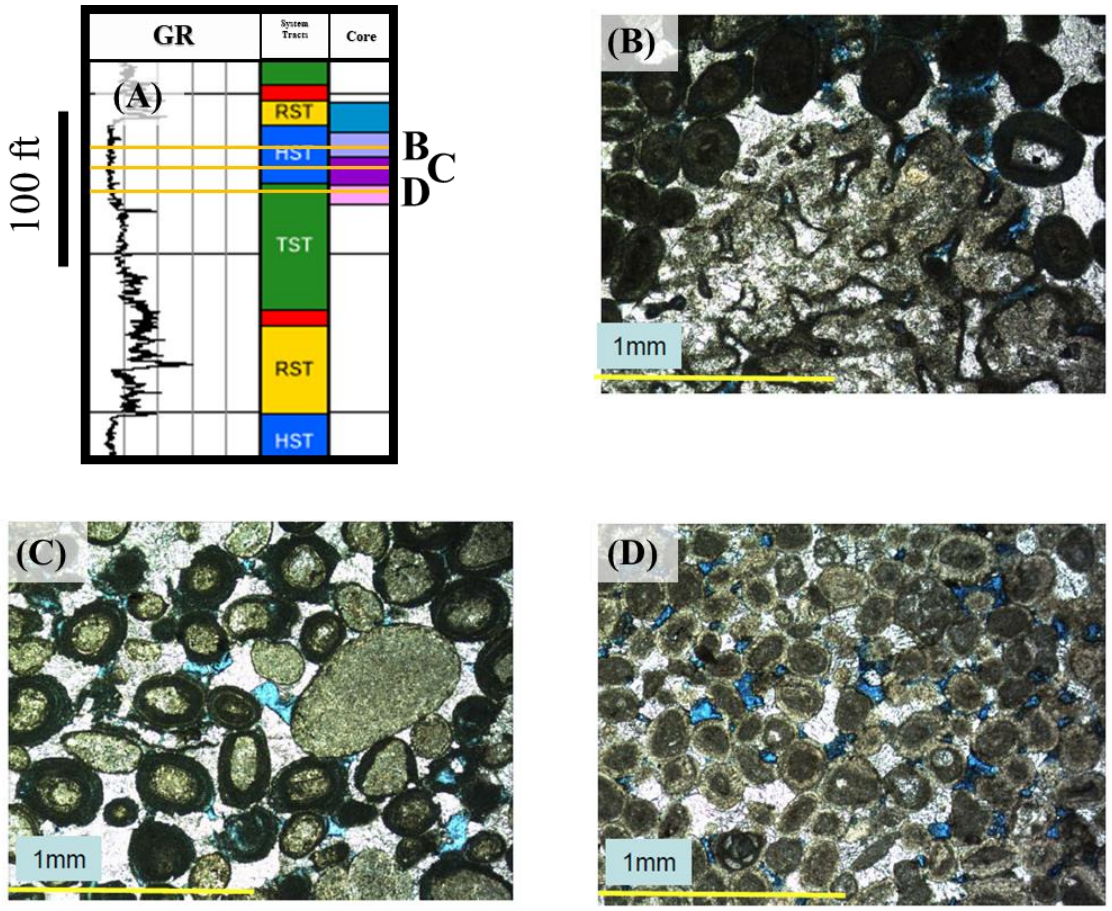

Figure 55: (A) The location of the thin sections on the GR log from well #1 HST-2. **(B)** Ooid grainstone with Cladocoropsis fragment. Porosity is mouldic and interparticle. **(C)** Ooid grainstone with partly calcite cement. Porosity is interparticle, intercrystalline and mouldic. **(D)** Ooid grainstone with partly calcite cement. Porosity is interparticle.

5.2.2 HST-2

Figure (55-A) reveals the extracted maximum porosity between J3 and J4 sequences from the predicted porosity volume. Figure (55-B) shows the extracted geobody with porosity equal or greater than 12% from the same volume. Hence, porosity development remains unrelated to the structure. Moreover, there are no

indications of inherited topography during the depositional period. HST-2 thickness varies from 40ft to 90ft across the area as measured from the borehole data.

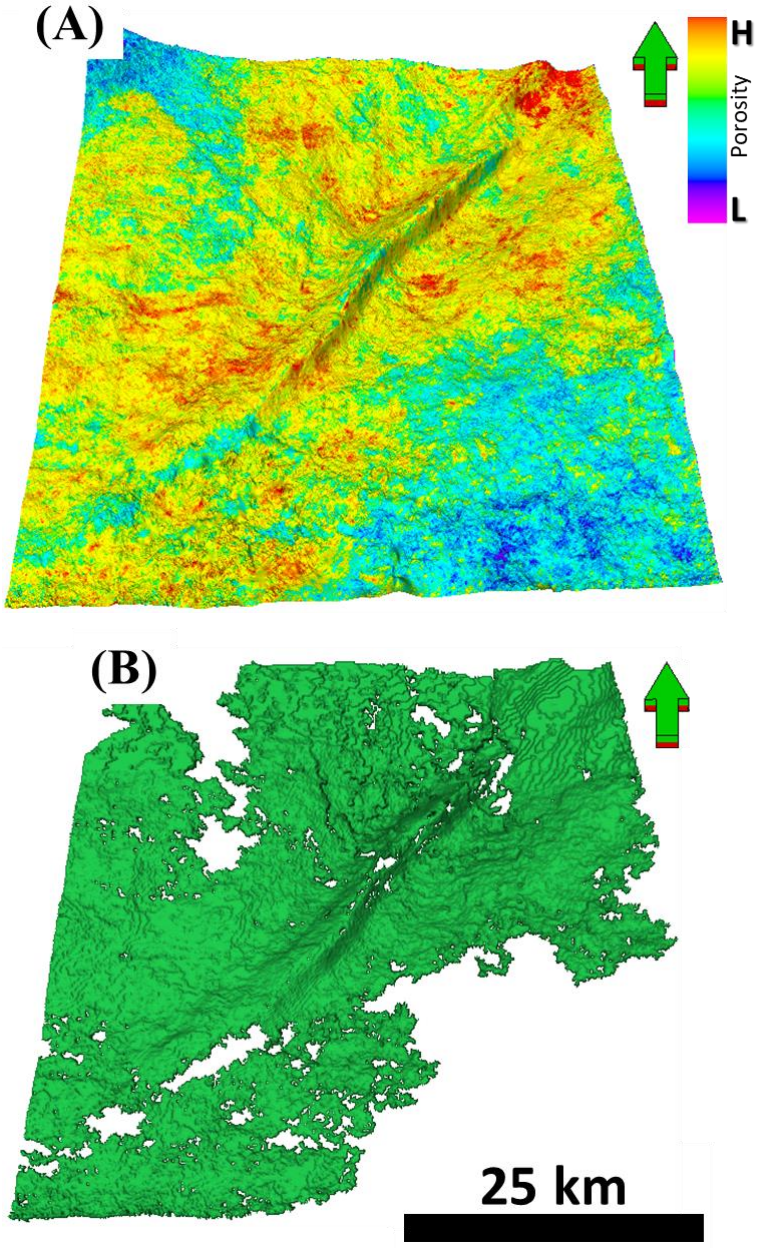

Figure 56: (A) Extracted maximum porosity values from the 3D porosity volume via neural network between the interpreted horizons J2 and J3. **(B)** Extracted geobody from the 3D porosity volume via neural network that shows the porosity connectivity across the area of interest.

5.2.3 HST-4

Similar analysis has been conducted on HST-4 similar to the one conducted on HST-2. However, HST-4 differs from HST-2 as it shows less connectivity within the reservoir, with low overall porosity. A geobody is extracted from the predicted porosity volume with values equal or greater than 8% (Figure 56-A). Extracted maximum porosity between J1 and J2 shows a pattern of northwest-southeast belt (Figure 56-b). This has been confirmed as well by the extracted seismic amplitude over the same zone (Figure 56-C). The seismic acquisition footprint is not the source for this pattern as the footprint has north-south and east-west directions. I have not observed any changes in thickness or buildups from the seismic data (Figure 57). However, core description indicates that low porosity zones also correspond to dolomitized zone as indicated from Wells # 2 and #5. While Well # 3 shows no evidence of dolomitization. This belt can be interpreted as an ooid shoal (bar). Another interpretation includes clinoform progradation in the northeast-southwest direction (Figure 58). The map view shows the possibility of five clinoform packages. Using the interpreted clinoforms from Figure (58), we can assume that clinoforms I, III, and V are dolomitized. Clinoforms II and IV are not affected by diagenesis, which suggests they are dominated by calcite, and have preserved porosity. Moreover, these clinoforms have very gentle angles and are deposited along a wide region, which make them hard to separate in the seismic volume.

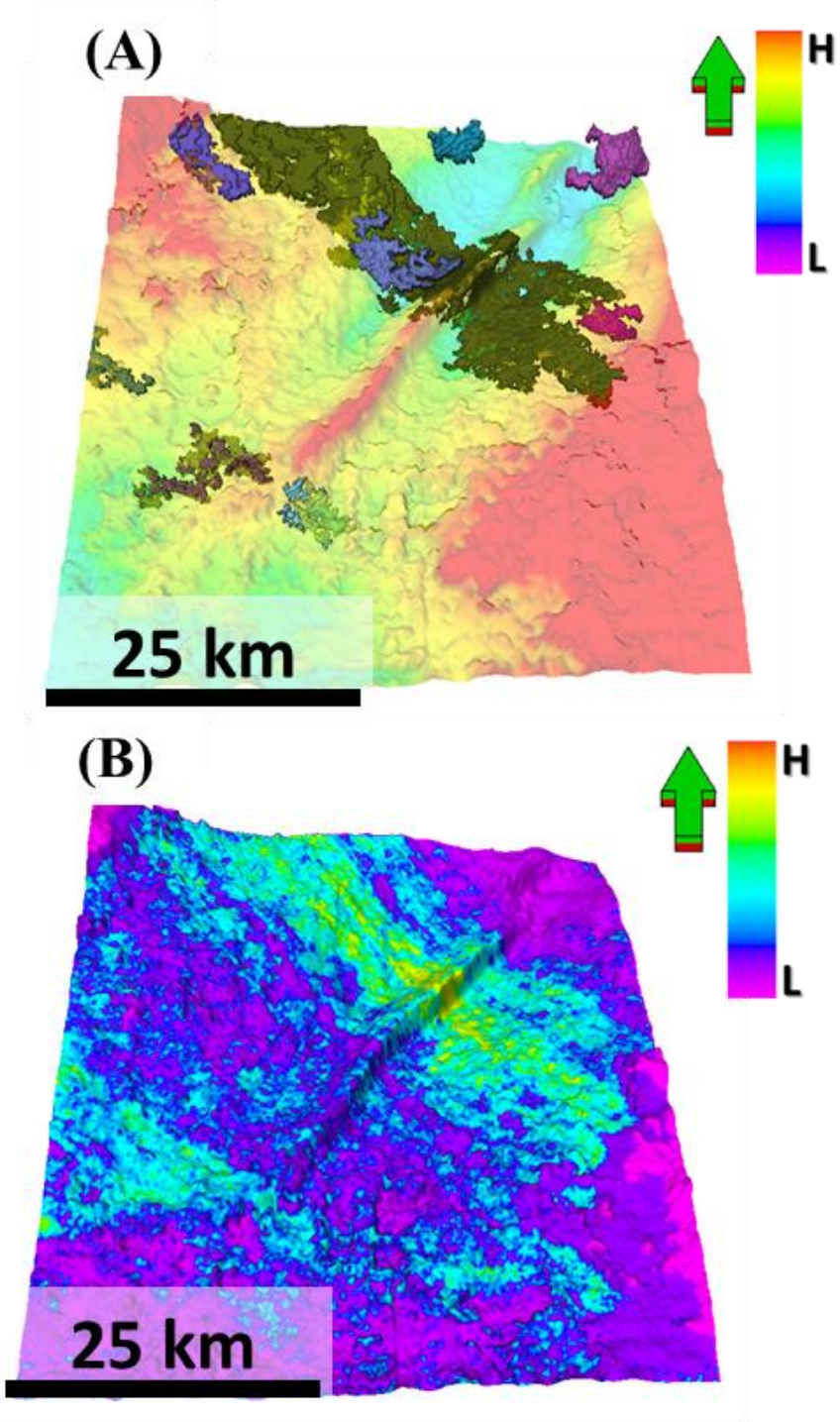

Figure 57: **(A)** Extracted geobody from the 3D porosity volume via neural network that shows the porosity connectivity across the area of interest overlay the structural map of the J5 horizon. **(B)** Extracted maximum porosity values from the 3D porosity volume via neural network between the interpreted horizons J4 and J5.

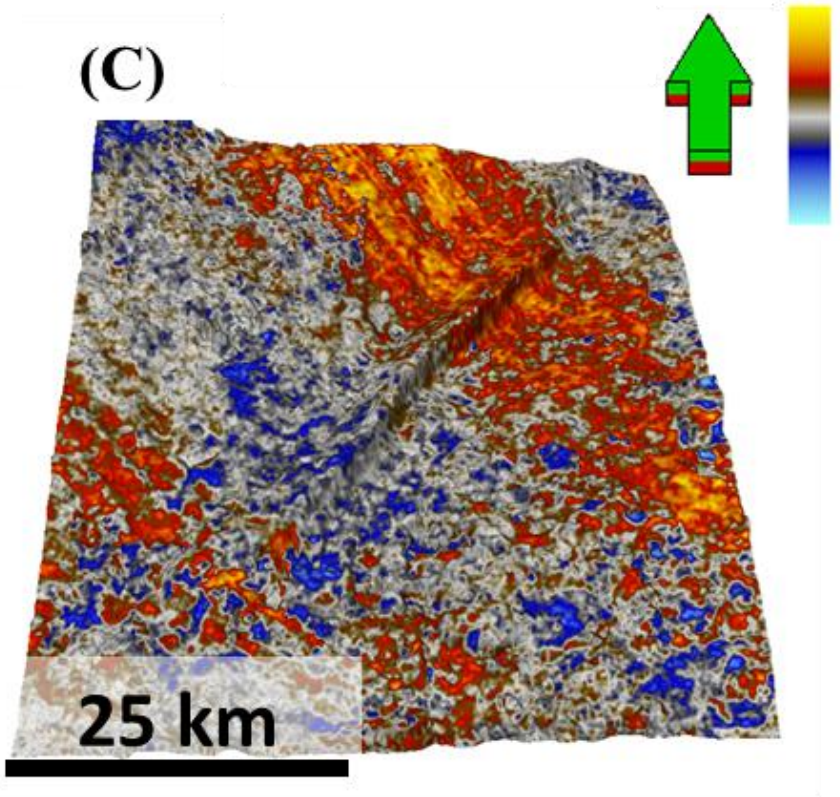

Figure 56: (C) Extracted seismic amplitude from the 3D seismic survey.

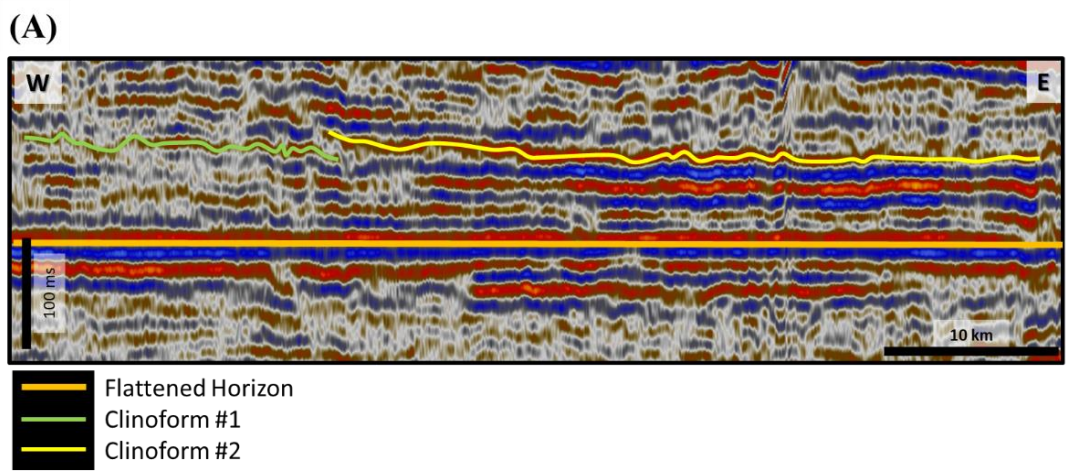

Figure 58: (A) Seismic section shows possible clinoforms in the HST-4 zone. These two clinforms have very gentle dip angle and extend over a long area.

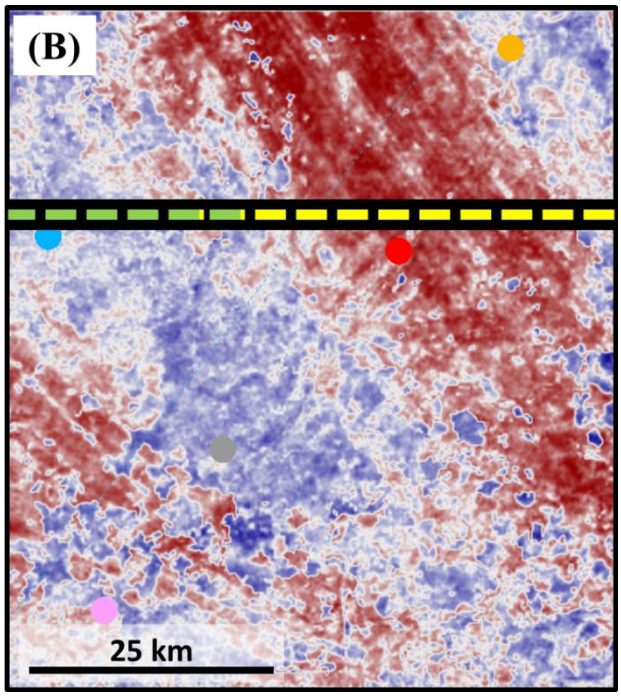

Figure 57: (B) Index map shows the extracted seismic amplitude along J5 horizon with the seismic section location as well as the extent of the two clinoforms.

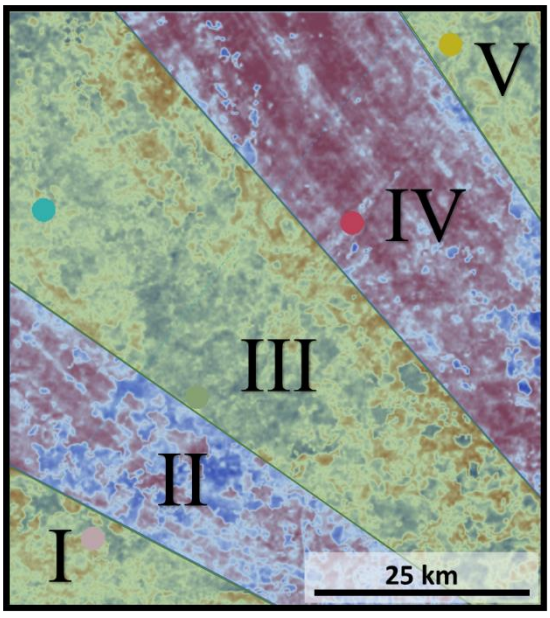

Figure 59: Extracted seismic amplitude along J5 horizon shows variance in the amplitude that can be divided into five clinoforms. Based on well penetration and core data, clinoforms II and IV are expected to have high porosity while clinoforms I, III and V are expected to have low porosity.

5.2.4 HST-1 and HST-3

HST-1 and HST-3 show very low porosity development (lower than 10%) and it is also disconnected (Figure 59). Yet the neutron-density crossplots show minimum dolomite content. Only Wells #1 & #2 have dolomite content (Figure 60). I used the density versus GR plot to reanalyze the system tracts (Figure 61) and highlight the ease of differentiating the HSTs from TSTs. However, HST-1 and HST-3 are located with the TSTs zone which suggests that the classified HST-1 and HST-3 are more likely to be an extension of TST-1 and TST-3 respectively. This implies that these HSTs layers were eroded, sea level was not high enough to allow for the carbonate production and growth, or the high sea level did not last enough.

Moreover, some part of TST-4 is located within the HSTs zone. This implies that the boundary between HST-4 and TST-4 can be set deeper.

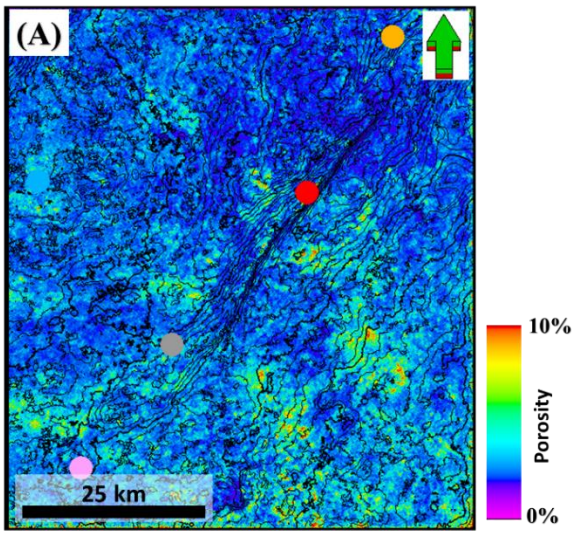

Figure 60: (A) Extracted maximum porosity values from the 3D porosity volume via neural network between the interpreted horizons J1 and J2 that represents HST-1.

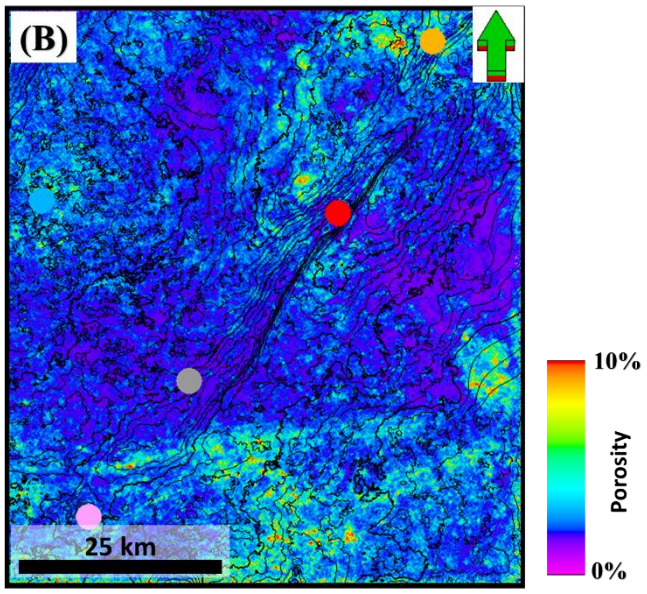

Figure 59: (B) Extracted maximum porosity values from the 3D porosity volume via neural network between the interpreted horizons J3 and J4 that represents **HST-3**. Both maps show very low porosity across the two zones. The color bar on the right is used for both maps.

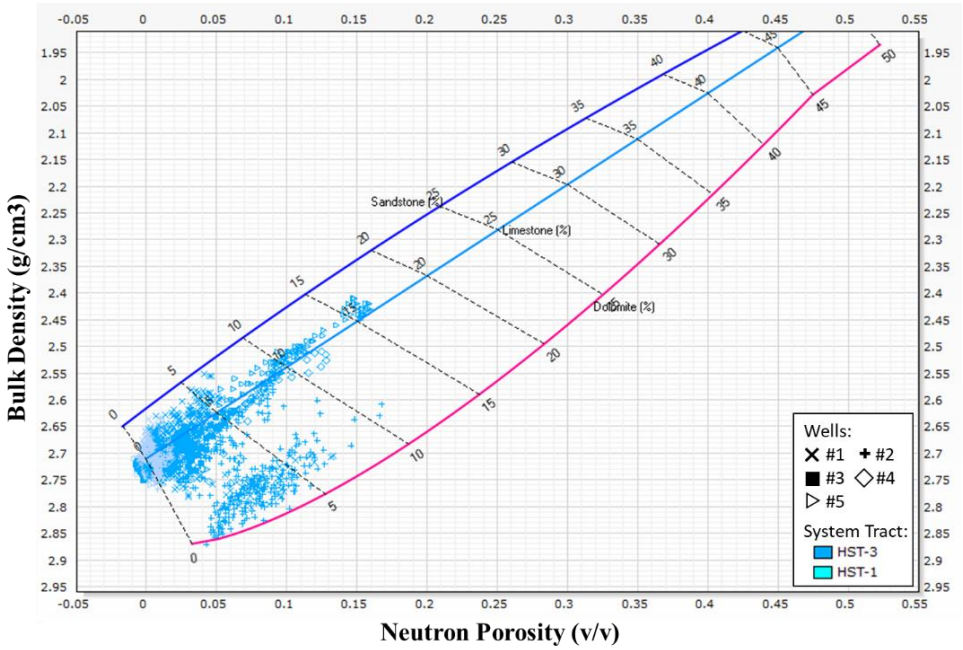

Figure 61: Bulk density versus neutron density cross plot for HST-1 and HST-3 for the five wells. Wells #1 **(X)** and #2 **(+)** have the highest percentage of the dolomitization compare to the other wells.

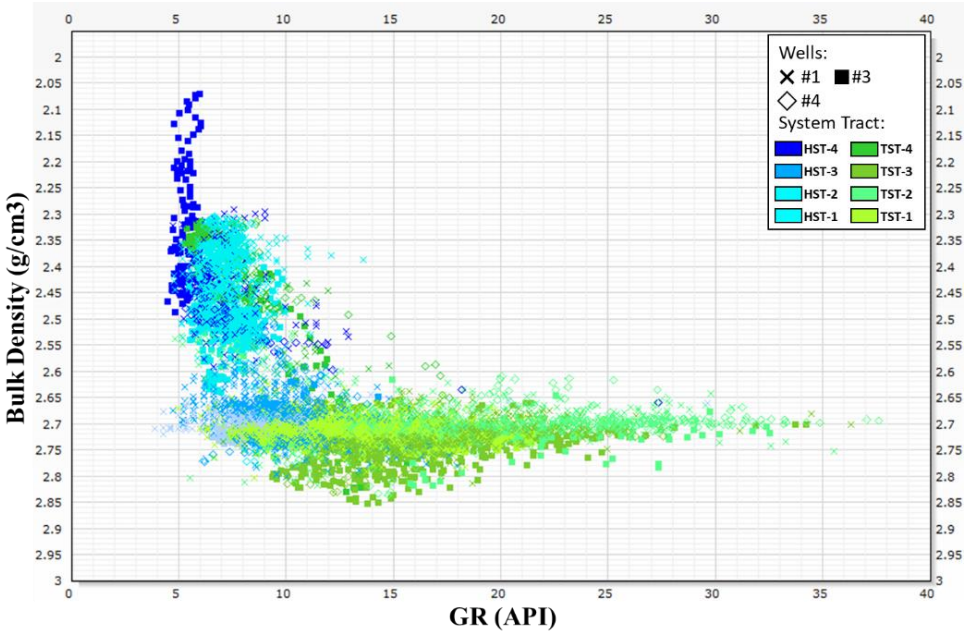

Figure 62: Bulk density versus GR cross plot for All the HSTs and TSTs for the three wells (#1, #3 and #4). HSTs can be separated from TSTs using this cross plot.

5.2.5 Lowstand System Tracts (LSTs)

LSTs are deposited during the lowest sea level. This environment allows for mudstone and shale deposition. As the sea level fall, the intrashelf basin becomes restricted. Thus, process energy drops allowing deposition of the mudstone. This implies that LSTs make good source rock as low circulation implies low O_2 level that in turn may allow for the preservation of organic content. However, there are no core data available across any of the interpreted LSTs. Confirmation of this conclusion would require geochemical analysis.

5.2.6 Regressive System Tracts (RSTs)

During sea level fall, RSTs are developed. These parasequences sets commence by eroding the previous deposition that is likely to be the HSTs. In some cases, reworked sediments are deposited creating good reservoirs with stratigraphic traps. Figure (62) shows a thin section extracted from the cores taken from the RST-1 from Well #4.

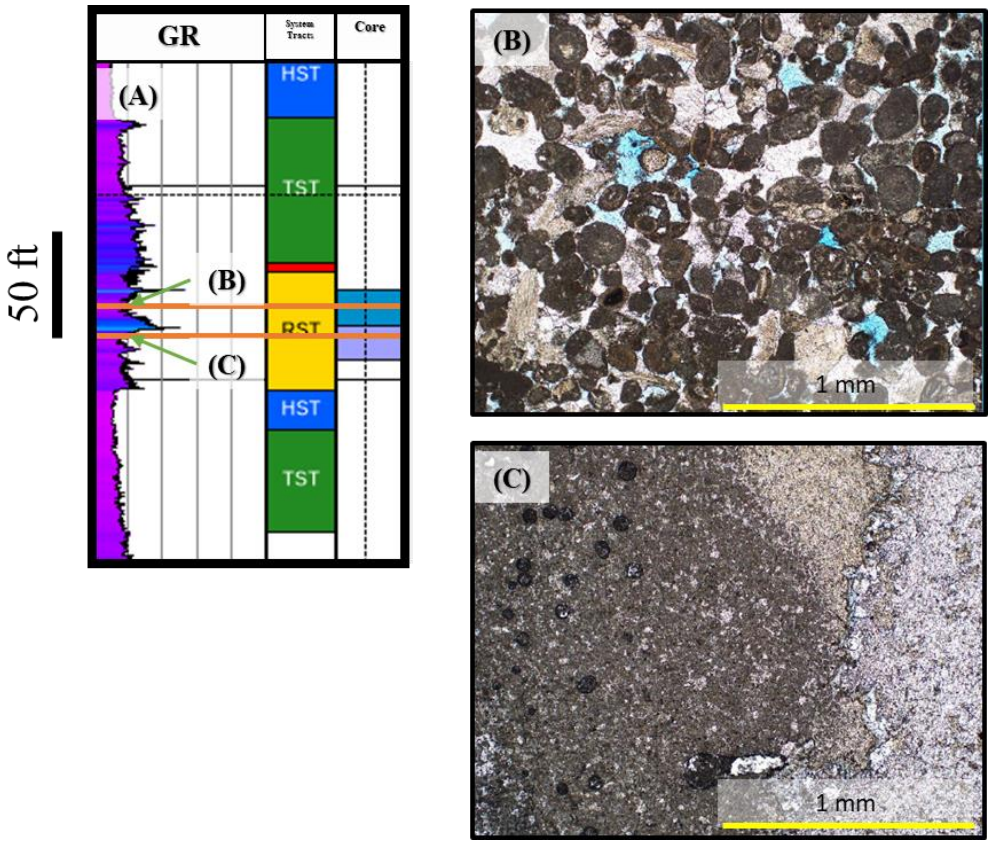

Figure 63: (A) The location of the thin sections on the GR log. **(B)** Thin section extracted from core #1 from Well #4 within RST-1. Ooids grainstone are shown with calcite cement. Blue color indicates porosity. **(C)** Thin section extracted from core #2 from Well #4 within RST-1. This thin section is a mudstone with almost no porosity due to cementation. Both these slides confirm the heterogeneity of the RST zone.

Although borehole data show development of porosity within the RSTs, the predicted porosity failed to detect the porosity zone. Either the reservoir zone falls below the seismic resolution or more control points are required to obtain a more accurate result.

It is important to note that the boundaries between RST-LST, LST-TST are hard to pick as it is difficult to distinguish between these systems using GR alone. Moreover, the RSTs erosion seem to correlate across the five wells indicating that allocyclic rather than autocyclic processes are likely at work. Well #2 has a higher order cycle (4^{th} order) within RST-1 that can be correlated across the other wells. No further analysis has been conducted, however, as it is a higher order.

Chapter 6 Conclusions and Recommendations

6.1 Conclusions

Galloway's principals for the genetic sequence stratigraphic method have been incorporated with Vail's method of seismic sequence stratigraphy in order to study the Jurassic carbonate strata of the Arabian Platform. The methods are applied on the 3D seismic volume and constrained by five wells. Using Vail motifs, thirteen interpreted sequence boundaries are mapped, resulting in one Cenozoic, three Cretaceous, six Jurassic, two Triassic and one Permian sequence boundaries. Using Galloway's principals, four 3rd order cycles are interpreted and correlated along the five wells, and encompass TST, HST, RST and LST parasequence sets. The principal findings of the study are:

1. Petroleum system elements were linked to the parasequences to predict the reservoir properties:
    a. HSTs: if they are preserved, they provide good reservoir, so long as diagenetic alteration has not destroyed primary porosity.
    b. LSTs: allow for environments capable of supporting deposition of organic-rich sediments, and encouraging preservation of organic content.
    c. RSTs: are heterogeneous parasequence sets as they can be a good seal due to unconformities above the HSTs, with abrupt shifts to fine-grained lithologies. Reworked sediments can also be

deposited during this stage to have a good porosity, encouraging the formation of stratigraphic traps.

2. Extracted porosity surfaces and bodies show no effect on the structure or their distribution. Thus, reservoir development occurred prior to the structural deformation. Presence of hydrocarbon means the structural traps were formed prior to the hydrocarbon generation and migration.
3. 3D porosity prediction via neural networks successfully predicted the continuity of HSTs high porosity. However, it failed to detect the RSTs porosity previously confirmed by borehole data.

6.2 Recommendations

To add more value to this study, the following recommendations are made:

1. Construct local sea level curves and compare to the interpreted system tracts.
2. Perform an extensive seismic attributes analysis to detect any possible carbonate features such as reef build ups.
3. Apply the approach utilized on this thesis on other datasets to quantify and approve its scientific approach.
4. Use the unavailable borehole data during the study to confirm the results as a blind test.

5. Retie seismic to wells using Vertical Seismic Profiles (VSP) to establish better relation to enhance the porosity prediction.
6. Obtain core data in the LSTs to perform decisive geochemistry investigation.
7. Re-examine the parasequence sets for their validity and in order to determine the relationship between the proposed relative sea level and the eustatic sea level.

References

Al-Husseini, M., 2011, Middle east geologic time scale 2011: Late ediacaran to early cambrian (infracambrian) jibalah group of Saudi Arabia: Geoarabia, v. 16, no. 3, p. 69–90.

Avseth, P., T. Mukerji, and G. Mavko, 2005, Quantitative Seismic Interpretation: Applying Rock Physics Tools to Reduce Interpretation Risk: Cambridge, Cambridge University Press.

Brown, L. F., and W. L. Fisher, 1977, Seismic-Stratigraphic Interpretation of Depositional Systems: Examples from Brazilian Rift and Pull-Apart Basins, *in* C. E. Payton, ed., Seismic Stratigraphy—Applications to Hydrocarbon Exploration: American Association of Petroleum Geologists Memoir 26: p. 213–248.

Caf, A. B., 2015, Seismic stratigraphic and quantitative interpretation of Leonardian reefal carbonates, Easterm Shelf of the Midland Basin: insight into sea level effects, geomorphology and associated reservoir quality: University of Oklahoma.

Caf, A. B. and J. D. Pigott, 2016, Seismic Stratigraphy and Quantitative Interpretation of the Midland Basin: Insight Into Sea Level Effects, AAPG Annual Convention and Exhibition, Calgary, Alberta, Canada.

Chopra, S., and K. J. Marfurt, 2007, Seismic attributes for prospect identification and reservoir characterization, Geophysical Developments No.11,: Society of Exploration Geophysicists.

Chopra, S., and K. J. Marfurt, 2016, Spectral decomposition and spectral balancing of seismic data: The Leading Edge, v. 35, no. 2, p. 176–179.

Galloway, W. E., 1989, Genetic stratigraphic sequences in basin analysis I: architecture and genesis of flooding-surface bounded depositional units: American Association of Petroleum Geologists Bulletin, v. 73, no. 2, p. 125–142.

Hampson, D. P., J. S. Schuelke, and J. A. Quirein, 2001, Use of multiattribute transforms to predict log properties from seismic data: Geophysics, v. 66, no. 1, p. 220–236.

Haq, B. U., and A. M. Al-Qahtani, 2005, Phanerozoic cycles of sea-level change on the Arabian platform: GeoArabia, v. 10, no. 2, p. 127–160.

Husseini, M. I., and S. I. Husseini, 1990, Origin of the Infracambrian Salt Basins of the Middle East: Geological Society, London, Special Publications, v. 50, no. 1, p. 279–292.

Konert, G., A. M. Afifi, S. A. Al-Hajri, and H. J. Droste, 2001, Paleozoic stratigraphy and hydrocarbon habitat of the Arabian plate: GeoArabia, v. 6, no. 3, p. 407–442.

Mackenzie, F. T., and J. D. Pigott, 1981, Tectonic controls of Phanerozoic sedimentary rock cycling: Jour. geol. Soc. London, v. 138, p. 183–196.

Mann, P., L. Gahagan, and M. B. Gordon, 2000, Tectonic Setting of the World's Giant Oil and Gas Fields, *in* M. T. Halbouty, ed., Giant Oil and Gas Fields of the Decade: 1990-1999, AAPG Memoir 78: p. 471–488.

Marzouk, I. M., and M. A. Sattar, 1993, Implication of Wrench Tectonics on Hydrocarbon Reservoirs, Abu Dhabi, U.A.E.: 3-6 p.

Milad, B., A. Alali, R. Slatt, and K. Marfurt, 2018, Geostatistical Integration of Multiscale Data to Construct the Hunton Group GeocellularModel: Upscaling Logs and Downscaling Seismic Impedance Volumes, in Search and Discovery.

Milad, B., and R. Slatt, 2018, Impact of lithofacies variations and structural changes on natural fracture distributions: Interpretation, v. 6, no. 4, p. T873–T887

Mitchum, R. M., and P. R. Vail, 1977, Seismic Stratigraphy and Global Changes of Sea Level, Part 7: Seismic Stratigraphic Interpretation Procedure, *in* C. E. Payton, ed., Seismic Stratigraphy—Applications to Hydrocarbon Exploration: American Association of Petroleum Geologists Memoir 26: p. 135–143.

Mitchum, R. M., P. R. Vail, and S. Thompson, 1977, Seismic Stratigraphy and Global Changes of Sea Level, Part 2: The Depositional Sequence as a Basic Unit for Stratigraphic Analysis, *in* C. E. Payton, ed., Seismic Stratigraphy—Applications to Hydrocarbon Exploration: American Association of Petroleum Geologists Memoir 26: p. 53–62.

Pigott, J. D., and M. O. Abouelresh, 2016, Basin deconstruction-construction: Seeking thermal-tectonic consistency through the integration of geochemical thermal indicators and seismic fault mechanical stratigraphy - Example from Faras Field, North Western Desert, Egypt: Journal of African Earth Sciences, v. 114, p. 110–124.

Pigott, J. D., and B. W. Bradley, 2014, Application of Production Decline Curve Analysis To Clastic Reservoir Facies Characterization Within A Sequence Stratigraphic Framework: Example --Frio Formation, South Texas: GCAGS, v. 3, p. 111–134.

Pigott, J. D., M. H. Kang, and H. C. Han, 2013, First order seismic attributes for clastic seismic facies interpretation: Examples from the East China Sea: Journal of Asian Earth Sciences, v. 66, p. 34–54.

Pigott, J., and D. Radivojevic, 2010, Seismic stratigraphy based chronostratigraphy (SSBC) of the Serbian Banat region of the Pannonian Basin: Central European Journal of Geosciences, v. 2, no. 4, p. 481–500.

Pigott, J. D., R. Zhai, K. L. Pigott, and T. Tonianse, 2012, Searching for the missing

link: The regressive system tract - seismic stratigraphic evidence from the southern gulf of Thailand: Society of Petroleum Engineers - International Petroleum Technology Conference 2012, IPTC 2012, v. 3, p. 2704–2724.

Russell, B., D. Hampson, and B. Bankhead, 2006, An inversion primer: CSEG recorder, v. 31, p. 97–104.

Sandberg, P. A., 1983, An oscillating trend in Phanerozoic non-skeletal carbonate mineralogy: Nature, v. 305, p. 19–22.

Schlumberger, 2017, Techlog, 2017.2.

Stanley, S. M., and L. A. Hardie, 1999, Hypercalcification: Paleontology links plate tectonics and geochemistry to sedimentology: GSA Today, v. 9, no. 2, p. 1–6.

Stern, R. J., and P. Johnson, 2010, Continental lithosphere of the Arabian Plate: A geologic, petrologic, and geophysical synthesis: Earth-Science Reviews, v. 101, no. 1–2, p. 29–67.

Stewart, S. A., 2016, Structural geology of the Rub' Al-Khali Basin, Saudi Arabia: Tectonics, v. 35, no. 10, p. 2417–2438.

Vail, P. R., and R. M. Mitchum, 1977, Seismic Stratigraphy and Global Changes of Sea Level, Part 1: Overview, *in* C. E. Payton, ed., Seismic Stratigraphy—Applications to Hydrocarbon Exploration: American Association of Petroleum Geologists Memoir 26: p. 51–52.

Vail, P. R., R. G. Todd, and J. B. Sangree, 1977, Seismic Stratigraphy and Global Changes of Sea Level, Part 5: Chronostratigraphic Significance of Seismic Reflections, *in* C. E. Payton, ed., Seismic Stratigraphy—Applications to Hydrocarbon Exploration: American Association of Petroleum Geologists Memoir 26: p. 99–116.

Wilson, J. L., 1997, Carbonate depositional environments and diagenesis, *in* I. Palaz, and K. J. Marfurt, eds., Carbonate Seismology: p. 9–28.

Ziegler, M. A., 2001, Late Permian to Holocene paleofacies evolution of the Arabian Plate and its hydrocarbon occurrences: GeoArabia, v. 6, no. 3, p. 445–504.

Appendix A

The PSAII was run on several initial models based according to the number wells utilized. Table below illustrates which wells were used in which model.

Model No.	Wells
#1	Well # 3
#2	Well #3 and Well #1
#3	Well #3 , Well #1 and Well #2
#4	Well #3 , Well #1, Well #2 and Well #4

The figures below show first the results of each inversion for Xline #5604 and second the results for Inline #3539.

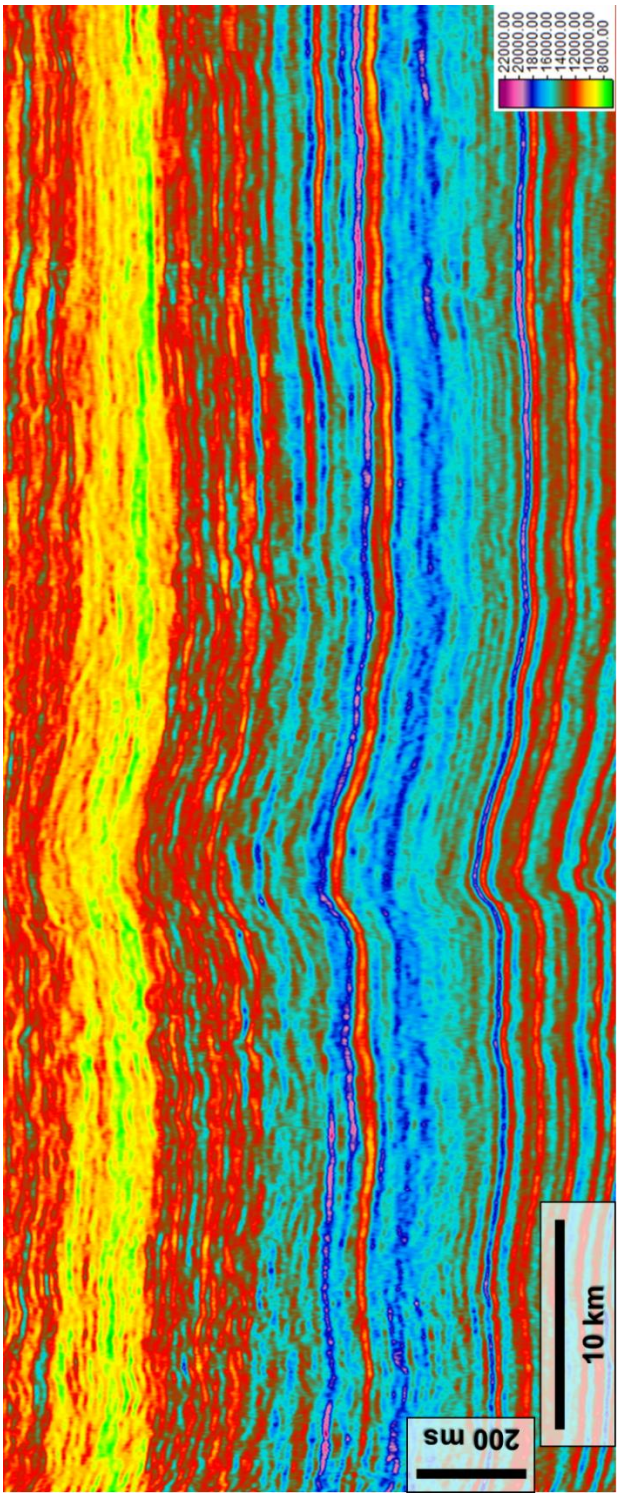

Figure 64: The PSAII Xline #5604 using one well (Well #3) in the initial model.

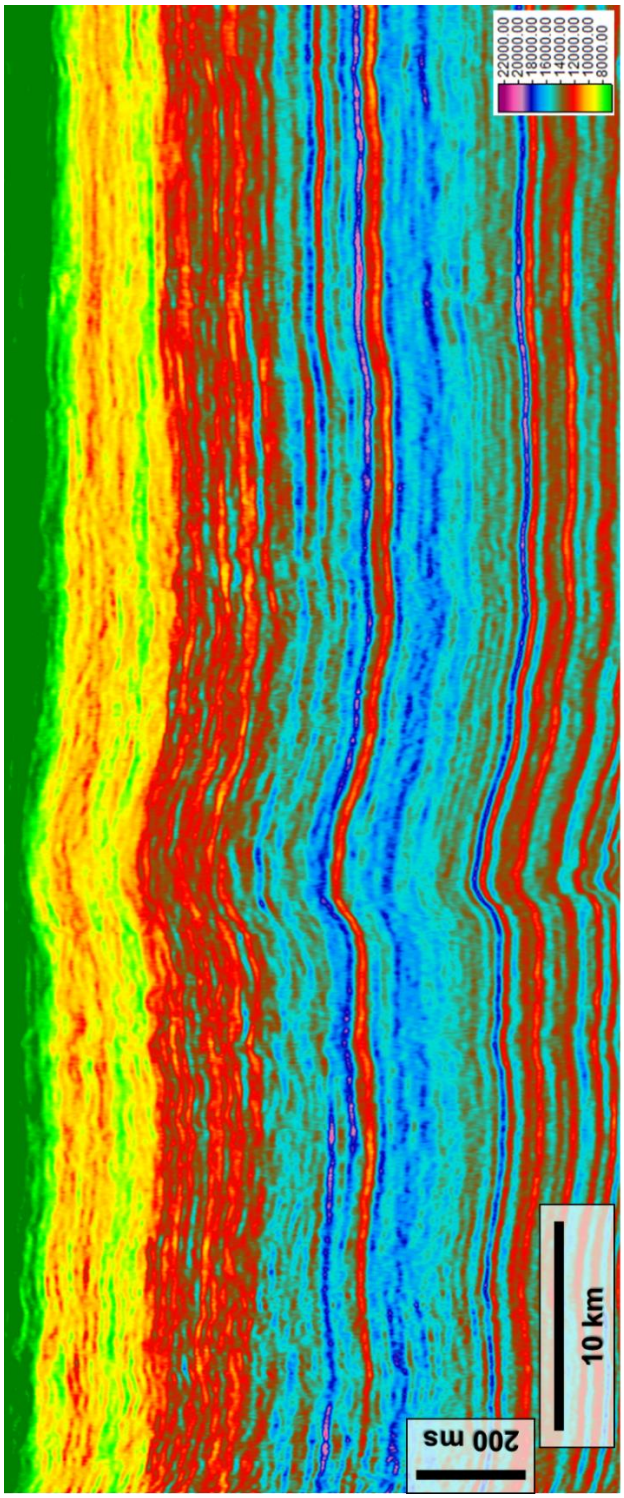

Figure 65: The PSAII Xline #5604 using two wells (Well #3 and #1) in the initial model.

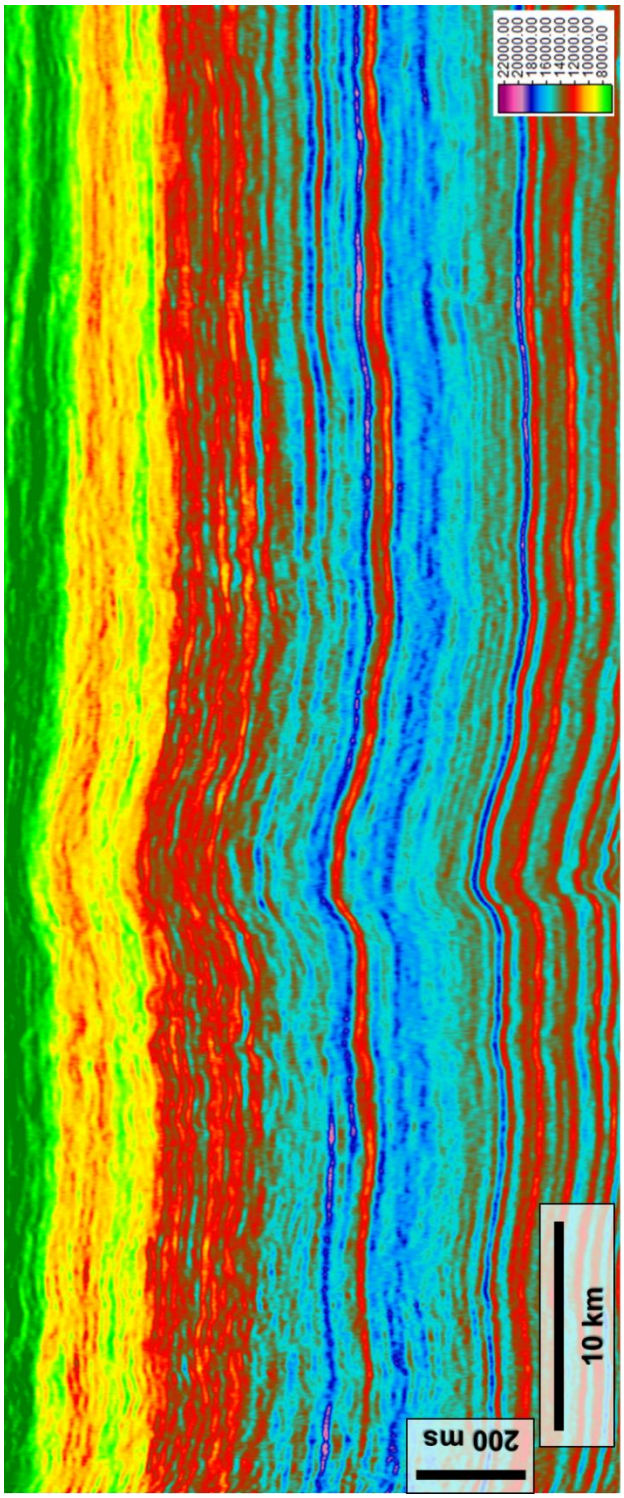

Figure 66: The PSAII Xline #5604 using three wells (Well #3, #1 and #2) in the initial model.

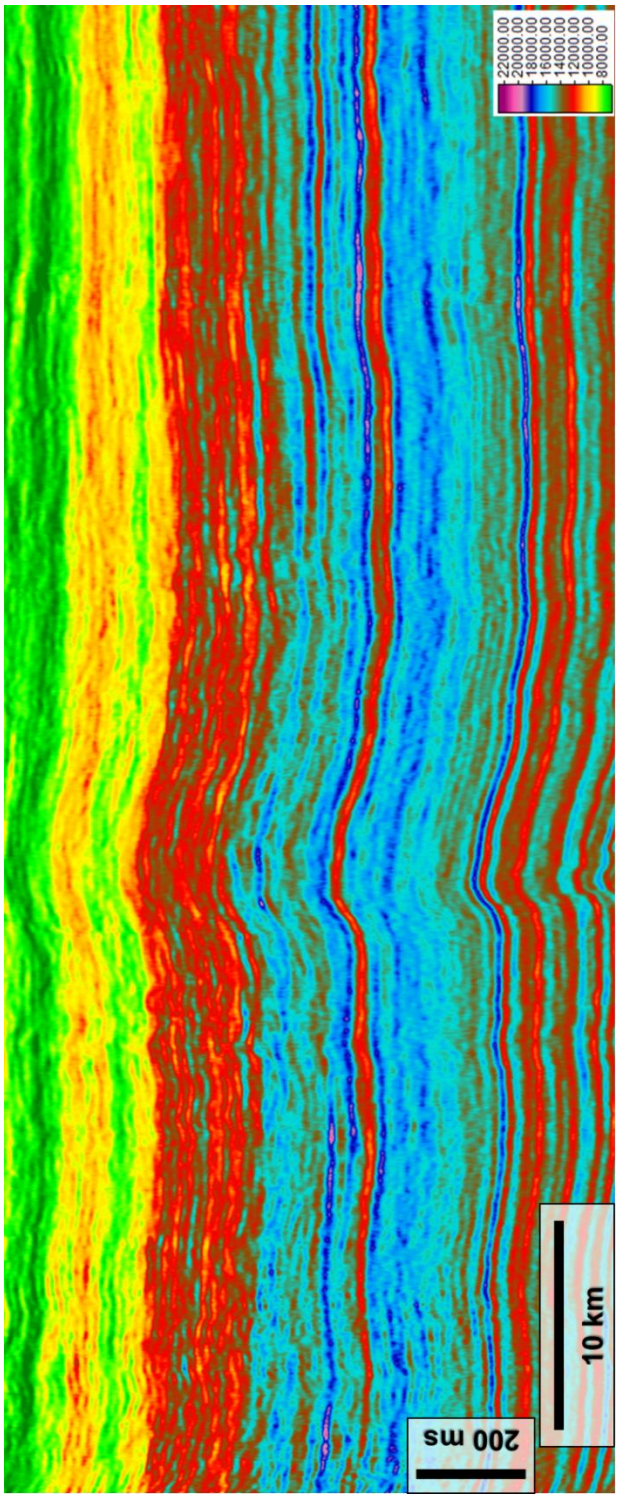

Figure 67: The PSAII Xline #5604 using four wells (Well #3, #1, #2 and #4) in the initial model.

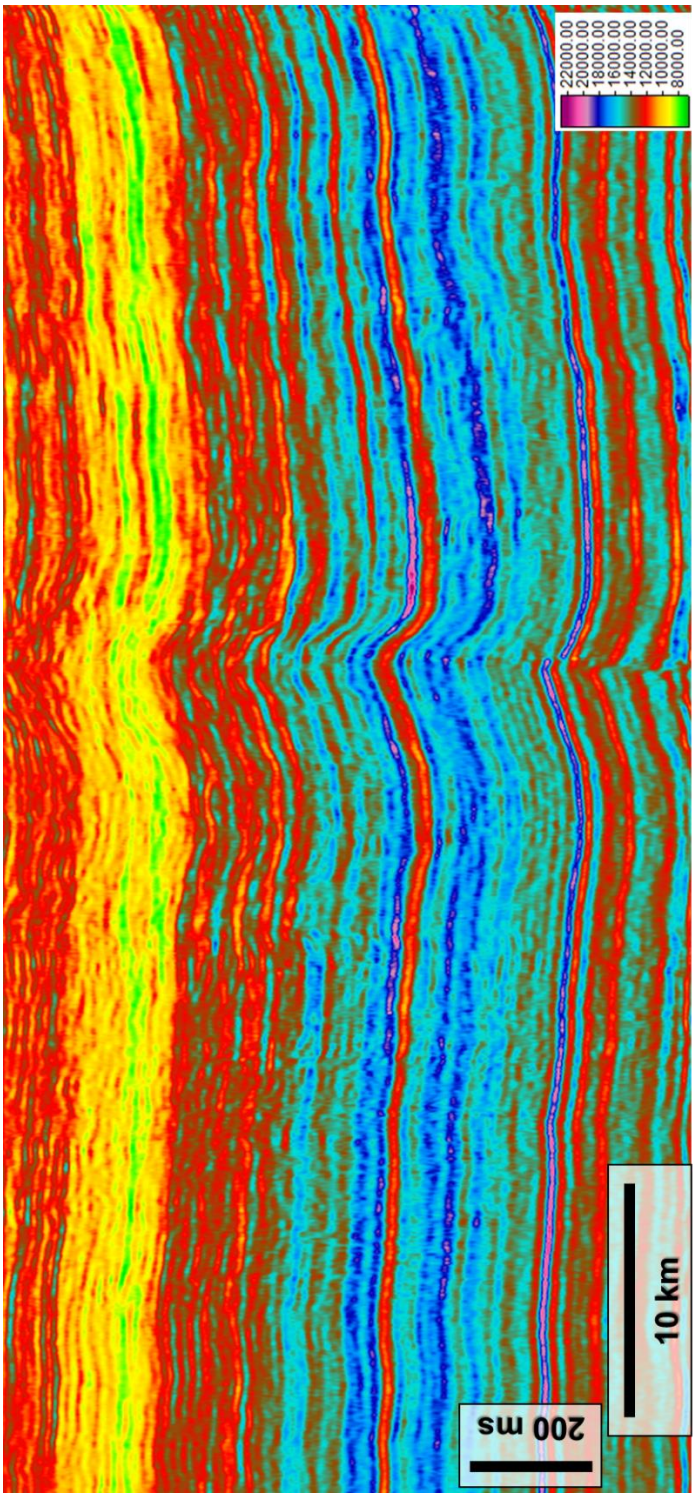

Figure 68: The PSAII Inline #5604 using one well (Well #3) in the initial model.

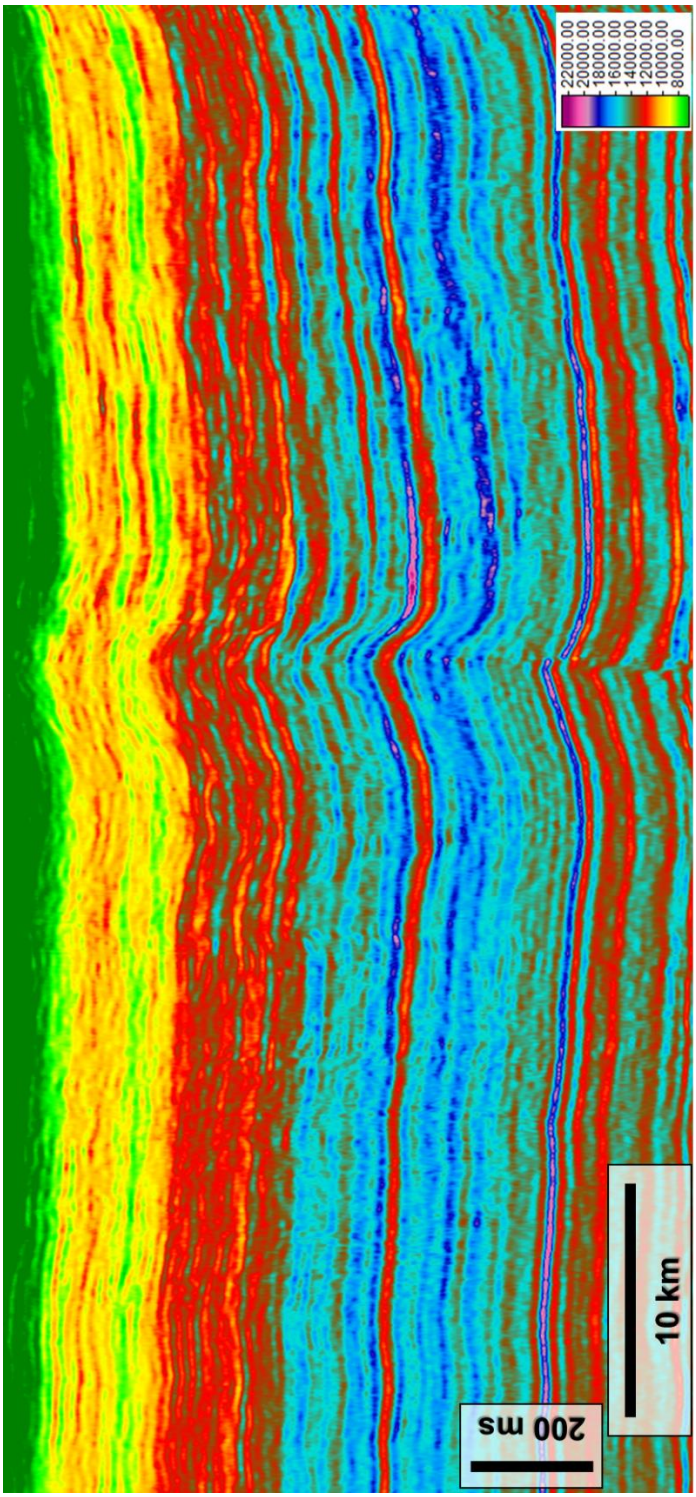

Figure 69: The PSAII Inline #5604 using two wells (Well #3 and #1) in the initial model.

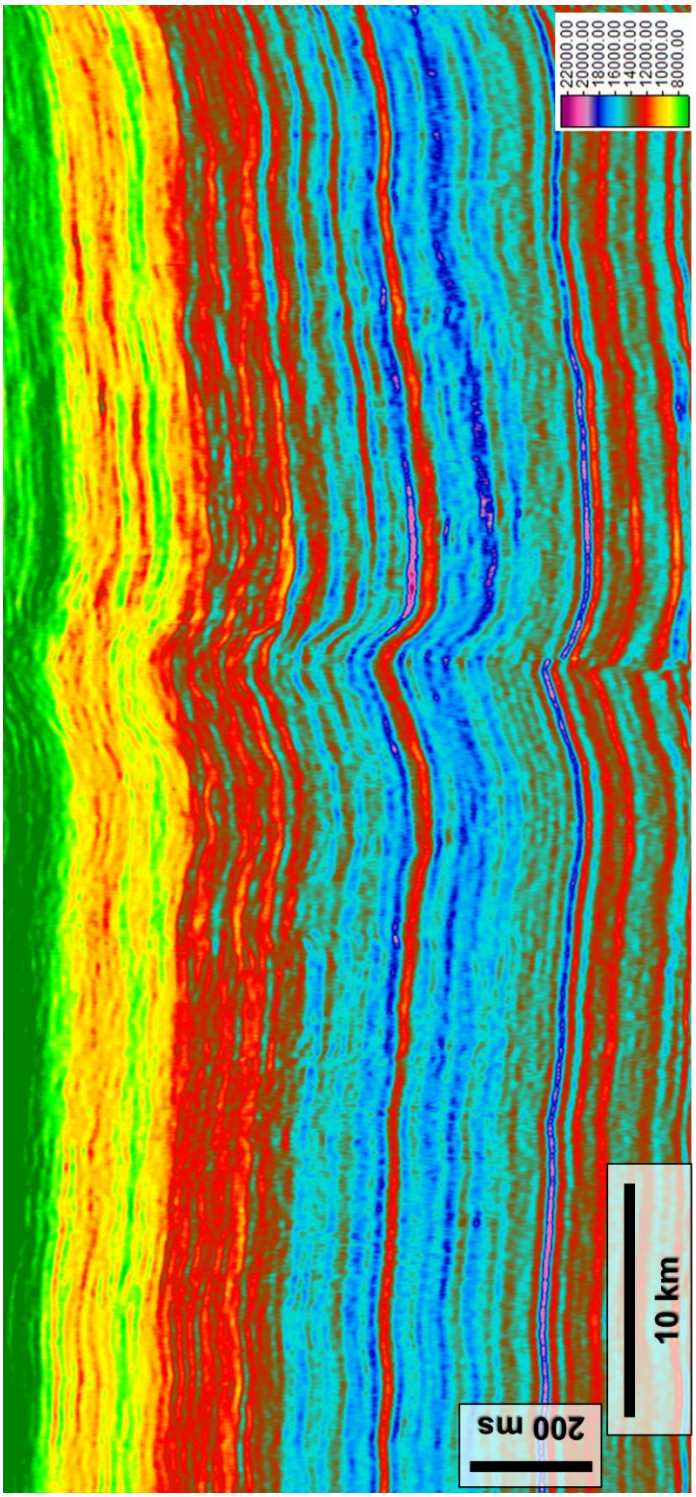

Figure 70: The PSAII Inline #5604 using three wells (Well #3, #1 and #2) in the initial model.

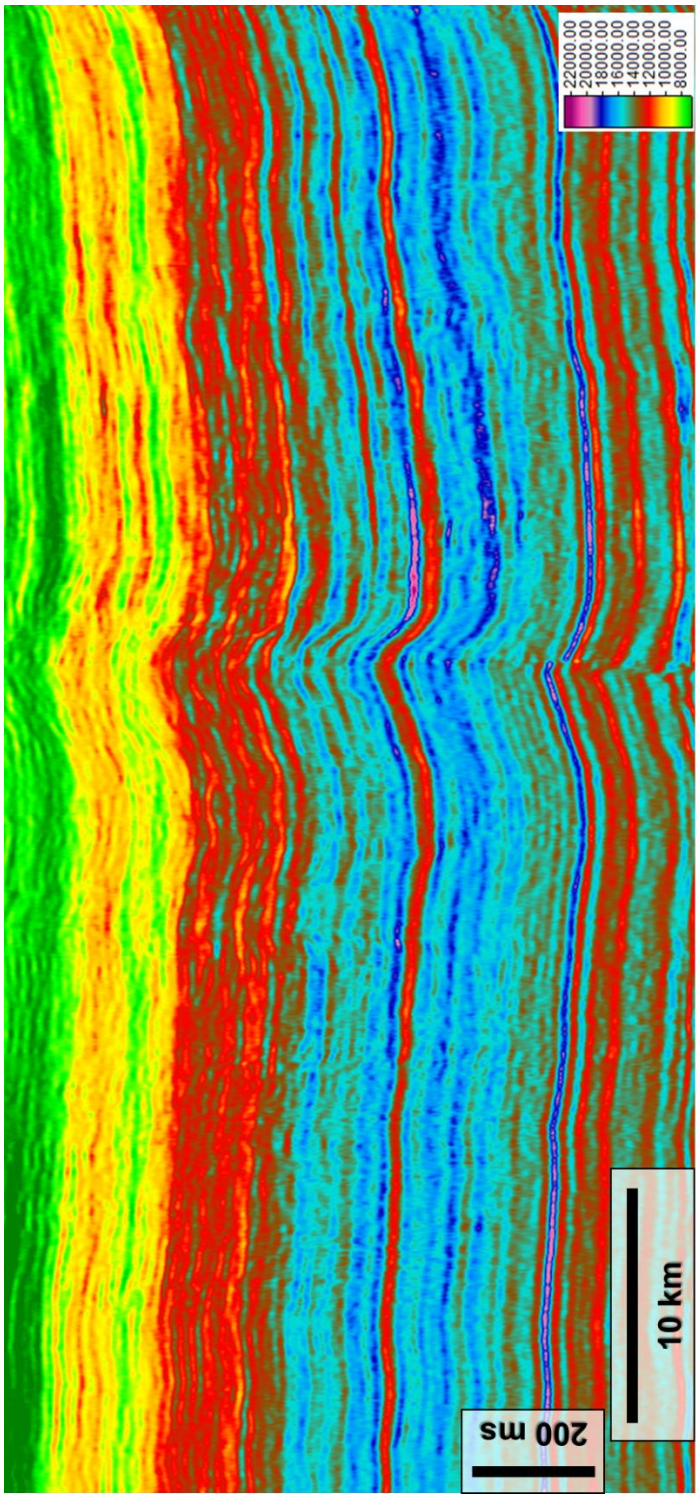

Figure 71: The PSAII Inline #5604 using four wells (Well #3, #1, #2 and #4) in the initial model.

Appendix B

Digitized core description is included in the Appendix. The lithology composition is shown in the left track, which has limestone (blue), dolomite (green), and anhydrite (pink). The right track shows the associated Dunham Classification. Each core description includes the well number, parasequence sets, and core number in the header.

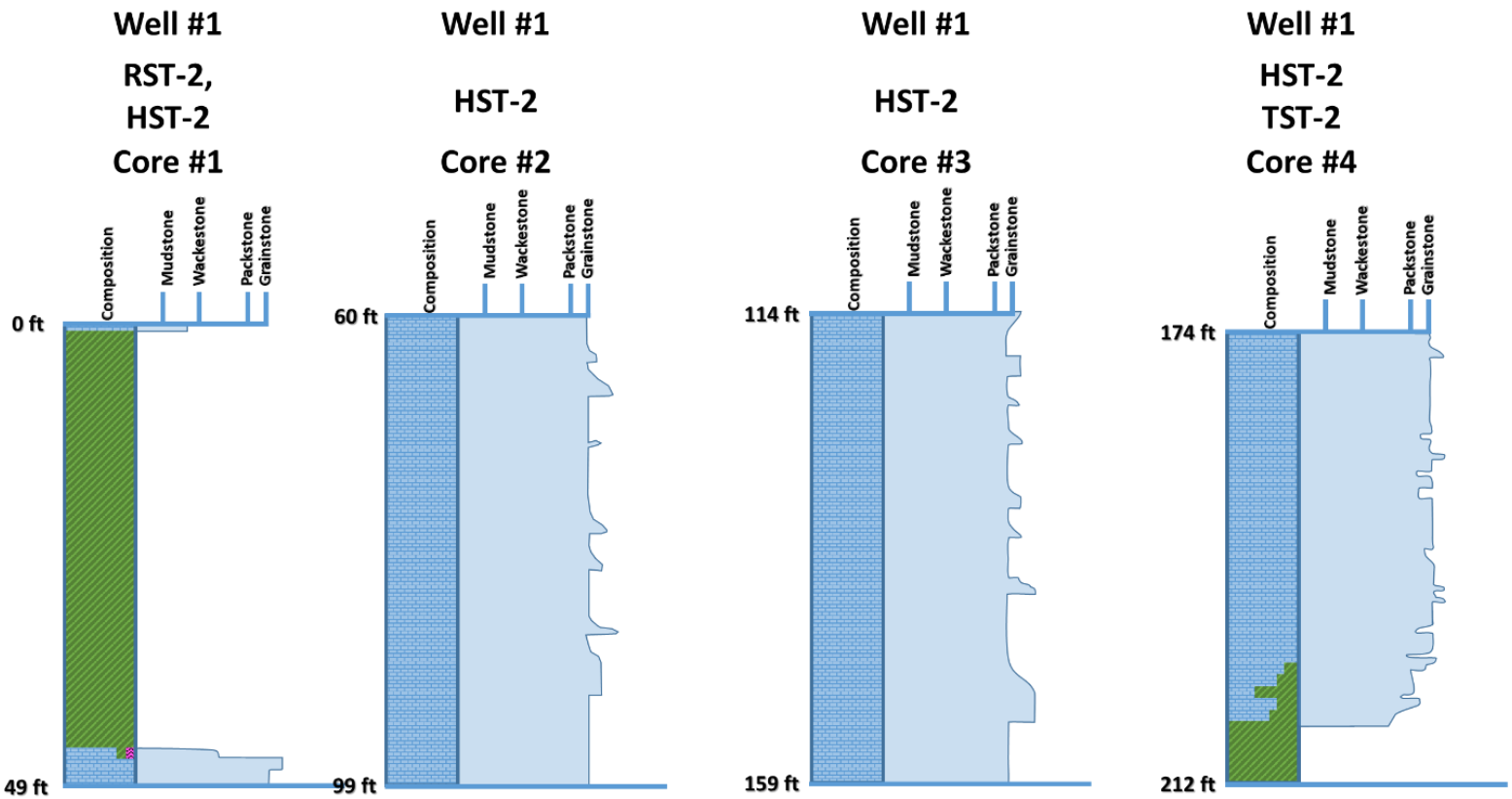

* There are some missing sections which explain the inconsistency between the end of one core and the start of another one.

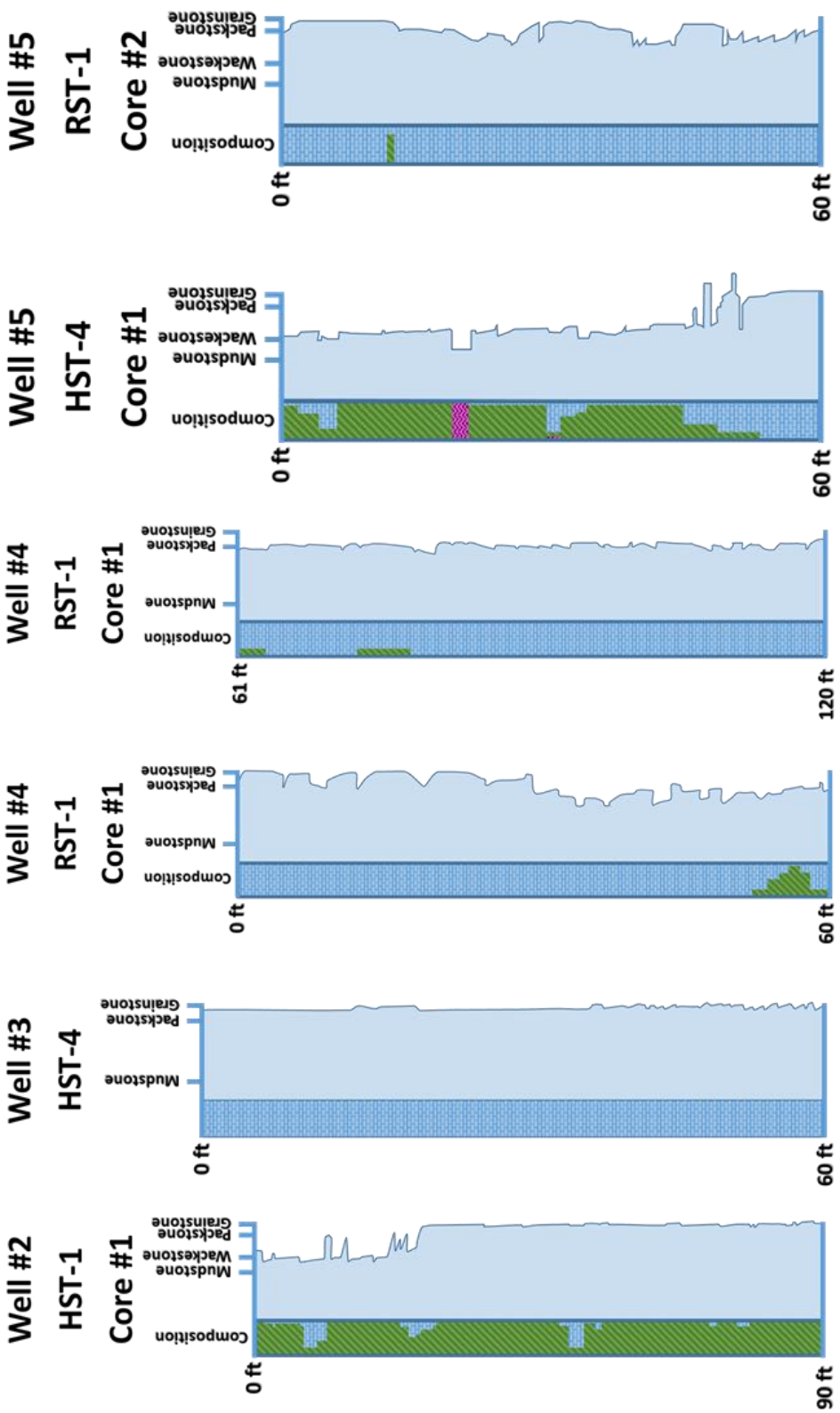
Well #5
RST-1
Core #2
Composition
Mudstone
Wackestone
Packstone
Grainstone
0 ft
60 ft
Well #5
HST-4
Core #1
Composition
Mudstone
Wackestone
Packstone
Grainstone
0 ft
60 ft
Well #4
RST-1
Core #1
Composition
Mudstone
Packstone
Grainstone
61 ft
120 ft
Well #4
RST-1
Core #1
Composition
Mudstone
Packstone
Grainstone
0 ft
60 ft
Well #3
HST-4
Mudstone
Packstone
Grainstone
0 ft
60 ft
Well #2
HST-1
Core #1
Composition
Mudstone
Wackestone
Packstone
Grainstone
0 ft
90 ft